

Out-of-Plane Compression Behaviour of Honeycomb Structures with Mass Gradient Produced by Additive Manufacturing Technologies

Tiago Ventura Rua

Thesis to obtain the Master of Science Degree in

Mechanical Engineering

Supervisors: Prof. Maria de Fátima Reis Vaz
Prof. Augusto Manuel Moura Moita de Deus

Examination Committee

Chairperson: Prof. Luís Filipe Galvão dos Reis
Supervisor: Prof. Augusto Manuel Moura Moita de Deus
Member of the Committee: Prof. Marco Alexandre de Oliveira Leite

September 2021

Agradecimentos

Em primeiro lugar, gostaria de agradecer aos meus orientadores, Professor Augusto e Professora Fátima, por toda a ajuda, dedicação e tempo despendido para que este trabalho fosse possível de ser realizado. A vossa simpatia e boa disposição proporcionaram sempre um ótimo ambiente de trabalho que sempre me incentivou a fazer mais e melhor.

Gostaria de agradecer ao Professor Manuel Sardinha do Laboratório para Desenvolvimento de Produto do Instituto Superior Técnico, imprescindível para a realização deste trabalho, não só pela transmissão dos conhecimentos nesta tão inovadora área de Fabrico Aditivo, mas também por todos os conselhos, disponibilidade e incentivo que foram um enorme contributo neste trabalho.

Obrigado ao João Ajuda do Laboratório para Desenvolvimento de Produto do Instituto Superior Técnico por todo o auxílio prestado na impressão dos provetes para este trabalho.

Queria também agradecer ao Professor Étienne Copin da École Nationale Supérieure des Mines d'Albi-Carmaux da Universidade de Toulouse pela sua amabilidade em produzir os provetes de alumínio para este trabalho.

Queria deixar uma palavra de profundo agradecimento aos meus pais por todo o apoio ao longo do meu percurso escolar, e em especial, nesta última fase tão complicada e cansativa como foi. A vossa sede pelo conhecimento e o afinco no trabalho foi fulcral para que eu aceitasse todos os desafios e ultrapassasse todas as barreiras sempre de cabeça erguida.

Em último, mas não menos importante, ao Diogo, ao Francisco, à Iva, ao João Afonso e ao João Francisco: uma palavra de ternura e eterno agradecimento. Falham-me as palavras neste momento. Será impossível alguma vez pôr por palavras tudo aquilo que foram seis anos vividos convosco: as gargalhadas, os desabafos, as viagens; as longas e complicadas horas de estudo no Espaço 24, os almoços no “Social”, as pausas no bar de Civil. Memórias eternizadas, sempre lembradas com muita alegria e que deixam vontade de criar novas. Vocês foram uma grande parte da força para realizar este trabalho e dão sentido àquilo que foi o meu percurso no Técnico. Em jeito de brincadeira, refiro-me a vós como “os meus irmãos”, mas o que é na verdade o CSDN, senão uma família? Que nunca seja adeus, mas sempre até já.

Resumo

Este trabalho tem como principal objetivo avaliar o comportamento de materiais celulares com gradiente de massa (nomeadamente, estruturas favo-de-mel) sob condições de compressão normais (fora do plano). O estudo foi conduzido experimentalmente e computacionalmente, no último caso recorrendo ao software *ABAQUS 2017*. Os provetes para ensaios experimentais foram impressos com os materiais ácido poliláctico (PLA) e alumínio, recorrendo a técnicas de Fabrico Aditivo como Fused Filament Fabrication (FFF) e Selective Laser Melting (SLM), apropriadas para o desenvolvimento de estruturas celulares. As geometrias estudadas foram modeladas com espessura de parede uniforme (estruturas regulares) e com variação da espessura de parede e comprimento da parede das células através de diferentes padrões de variação geométrica.

Neste trabalho, as características das estruturas favo-de-mel estudadas foram a rigidez, a capacidade de absorção de energia e a resistência mecânica. Durante os estudos, foi verificado que os parâmetros geométricos da estrutura têm uma grande influência na forma como a estrutura reage a esforços efetuados para fora do plano. Conclui-se que a área de projeção dos provetes e o rácio espessura-comprimento das paredes das células (este último fisicamente expresso pela densidade relativa) são os principais fatores que influenciam o desempenho das estruturas favo-de-mel, sejam elas regulares ou com gradiente. No que toca à distribuição de tensões, verificou-se que quanto maior é a densidade relativa, menores são as tensões sentidas pelas estruturas.

Relativamente às estruturas com gradiente geométrico, foi possível verificar que, embora a área projetada das estruturas e a densidade relativa continuem a ter a maior influência sobre as mesmas, a distribuição de massa no plano da estrutura também influencia o comportamento destas: amostras com maior concentração de massa junto ao centro da geometria, tendem não só a absorver mais energia, mas também a possuírem maior rigidez.

A introdução de gradientes geométricos no plano das estruturas pode melhorar a sua capacidade de absorção de energia e aumentar a sua rigidez, bem como reduzir as tensões sentidas por estas, quando são solicitadas por carregamentos para fora do plano. As estruturas de gradiente de massa com densidades relativas mais elevadas constituem uma boa alternativa às geometrias tradicionais.

Palavras-chave: Materiais Celulares com Gradiente de Massa, Estruturas Favo-de-Mel, Fabrico Aditivo, Análise por Elementos Finitos, Carregamentos para fora do plano, Absorção de Energia.

Abstract

The present work has as its main objective to evaluate the out-of-plane behaviour on functionally graded cellular materials with mass gradients, namely honeycomb structures under compressive conditions. The study is conducted both experimentally and numerically; in the latter case, using the software *ABAQUS 2017*. The experimental specimens were produced out of polylactic acid (PLA) and aluminium using Additive Manufacturing techniques, Fused Filament Fabrication (FFF) and Selective Laser Melting (SLM), respectively, referenced as adequate when it comes to the development of cellular structures. The studied geometries were modelled with uniform wall thickness (regular structures) and with varying wall thickness and cell length size through different geometrical variations (graded structures).

In this study, stiffness, energy absorption capacity and strength were the chosen characteristics to evaluate the performance of the honeycomb structures. During the study, it was verified that in-plane geometrical parameters influence how the structure handled out-of-plane loadings. It was concluded that the specimen overall size and the thickness-to-length ratio (physically expressed by the relative density) were the main factors to influence the performance of honeycomb structures, whether regular or graded structures. Regarding the structures strength, it was possible to verify that the higher the relative density is, the lower the stress (at a given displacement) is.

Regarding specifically to the graded structures, numerical analysis showed that, although specimen size and relative density continue to influence the most, the in-plane mass distribution also has a contribution to the structures behaviour: those that have more mass concentration near the centre of the geometry tend to perform better in energy absorption and have higher stiffness.

The introduction of in-plane geometrical gradients may enhance the energy absorption capacity and improve the stiffness and the strength of the honeycomb structures when loaded in their out-of-plane direction. Functionally graded materials with higher relative densities constitute a good alternative to the traditional honeycomb geometries.

Keywords: Functionally Graded Mass Materials, Honeycomb Structures, Additive Manufacturing, Finite Element Analysis, Out-of-Plane Loading, Energy Absorption.

List of Contents

Agradecimientos	i
Resumo	iii
Abstract	iv
List of Contents	v
List of Figures	viii
List of Tables	xi
List of Abbreviations, Acronyms, Symbols and Variables	xii
Chapter 1: Introduction	1
1.1 Motivation and Objectives	1
1.2 Thesis Outline	2
Chapter 2: Literature Review	3
2.1 Composite Materials	3
2.2 Cellular Materials	4
2.2.1 Overview	4
2.2.2 Production Methods of Honeycomb Structures	6
2.3 Additive Manufacturing	7
2.3.1 Selective Laser Melting (SLM)	8
2.3.2 Fused Filament Fabrication (FFF)	9
2.4 Functionally Graded Materials	11
2.4.1 Previous works	11
2.4.2 Relative density	16
2.4.3 Out-of-Plane Mechanical Properties	17
Chapter 3: Materials and Methods	19
3.1 Materials properties	19
3.1.1 PLA	19
3.1.2 Aluminium	20
3.2 Modelling of CAD-3D Geometries	20
3.2.1 Regular Structures	21

3.2.2	Graded Structures	21
3.3	Numerical Methodology	26
3.3.1	Computational model	26
3.3.2	Mesh Refinement	36
3.4	Specimens 3D-printing	37
3.4.1	PLA samples	37
3.4.2	Aluminium samples	38
3.5	Experimental Test	39
Chapter 4:	Results and Discussion	41
4.1	Preliminary Notes	41
4.2	Force vs. Displacement Curves	41
4.2.1	PLA	41
4.2.2	Aluminium	52
4.3	Discussion	58
4.3.1	PLA samples	58
4.3.2	Aluminium samples	73
4.3.3	Comparison With Analytical Expressions	75
4.3.4	Comparison Between Regular structures and Graded structures	78
Chapter 5:	Conclusions	79
5.1	Future Work	80
References		81
Appendix A:	Numerical Methodology	A1
A.1	Use of Symmetry	A1
Appendix B:	Materials Properties and Composition	B1
B.1	Aluminium's Chemical Composition	B1
B.2	PLA specimen's Mechanical Properties	B1
Appendix C:	Parametric Studies on the Geometrical Parameters Influence and Results Processing	C1
C.1	PLA regular structures – Elasto-plastic regime simulation	C1
C.2	PLA Stress-strain curves	C2

C.3 Aluminium regular structures – Numerical analysis	C4
C.4 Aluminium regular structures – Experimental test	C5
C.5 Error Statistics for Aluminium Experimental Testing Results	C7
C.6 Aluminium Stress-strain curves	C7
C.7 Determination of Euler's Critical Load and Comparison with Maximum Load	C7
Appendix D: Produced Specimens	D1
D.1 PLA Specimens	D1
D.2 Aluminium Specimens	D2

List of Figures

Figure 2.1 - Properties comparison between composite materials, steel and aluminium [3].	3
Figure 2.2 - (a) Tetrahedral truss core; Bi-directionally corrugated core (b); Honeycomb core (c) [4].	3
Figure 2.3 - Sandwich structure with honeycomb core [11].	4
Figure 2.4 - Possible applications of cellular materials [13].	4
Figure 2.5 - Cellular materials classification according to their topology [15].	5
Figure 2.6 - Diagram for the expansion method – honeycomb manufacturing process [1].	6
Figure 2.7 - Diagram for the corrugation method – honeycomb manufacturing process [1].	7
Figure 2.8 - AM processes divided into categories according to the pre-processed material's state [21].	8
Figure 2.9 - Schematics of the powder-bed fusion process [21].	9
Figure 2.10 - Schematics of FFF process [22].	9
Figure 2.11 - Representation of FFF process parameters: (a) build orientations,	10
Figure 2.12 - Example of an insert at a sandwich core structure [36].	14
Figure 2.13 - Reference area on a unit cell.	16
Figure 2.14 - Schematics of the unit cell and geometric variables.	17
Figure 2.15 - Out-of-plane properties for honeycomb structures [10].	17
Figure 3.1 - Filkemp PLA filament.	19
Figure 3.2 - Symmetry lines for the considered honeycomb graded structures.	22
Figure 3.3 - Belts for (a) main and (b) secondary symmetry lines.	22
Figure 3.4 - Considered distance variables for R1 calculations.	24
Figure 3.5 - R1 function for honeycomb graded structures.	24
Figure 3.6 - R2 function for honeycomb graded structures.	25
Figure 3.7 - Importing/creating a new part – “Part” module.	27
Figure 3.8 - Material properties of PLA for the elastic regime – “Property” module.	28
Figure 3.9 - Material properties for the compression plates – “Property” module.	28
Figure 3.10 - Material properties of PLA for the elasto-plastic regime – “Property” module.	29
Figure 3.11 - Sections' creation window – “Property” module.	29
Figure 3.12 - Sections' assignment window – “Property” module.	29
Figure 3.13 - “Create instance” window – “Assembly” module.	30
Figure 3.14 - Assembly for the compression test simulation – “Assembly module”	30
Figure 3.15 - “Create step” window – “Step” module.	30
Figure 3.16 - Window for step's settings – “Step” module.	31
Figure 3.17 - Interaction creation and properties windows – “Interaction” module.	32
Figure 3.18 - Boundary conditions definition – “Load” module.	33
Figure 3.19 - Element types/seed control windows and mesh applied to the structure – “Mesh” module.	34
Figure 3.20 - Viewport for von Mises stress over the structure – “Visualization” module.	35
Figure 3.21 - “U2” field output procedure – “Visualization” mode.	35

Figure 3.22 - "RF2" field output procedure – "Visualization" module 36

Figure 3.23 - Convergence analysis for the full model at various nodes. 37

Figure 3.24 - (a) Ultimaker 3 printer; (b) Ultimaker Cura software interface. 38

Figure 3.25 - (a) Instron 3369; (b) load cell installed on the test equipment. 39

Figure 3.26 - View of Instron Bluehill software for data acquisition. 39

Figure 4.1 - Force vs. Displacement curves for aluminium regular structures with different specimen size: (a) (b) (c) L4; (d) (e) (f) L6; (g) (h) (i) L8; (j) (k) (l) L10. 47

Figure 4.2 - Force vs. Displacement for PLA graded structures (first design method). 48

Figure 4.3 - Force vs. Displacement for PLA graded structures (second design method): (a) Decreasing density; (b) Increasing density..... 49

Figure 4.4 - Force vs. Displacement for PLA graded structures (second design method): increasing and decreasing densities on first option. 50

Figure 4.5 - Force vs. Displacement for PLA graded structures (third design method): (a) $R_1 = +0,31$; (b) $R_1 = -0,31$ 51

Figure 4.6 - Force vs. Displacement for PLA graded structures (third design method): $R_1 = +0.22$, $R_1 = -0.22$, $R_1 = -0.37$ 51

Figure 4.7 - Force vs. Displacement curves for Aluminium regular structures – Numerical and experimental results: (a) (b) L4; (c) (d) (e) L6; (f) (g) (h) L8; (i) (j) (k) L10. 57

Figure 4.8 - Specific stiffness vs. specimen size for PLA regular structures – Numerical analysis. 60

Figure 4.9 - Specific energy absorbed vs. specimen size for PLA regular structures – Numerical analysis. 61

Figure 4.10 - Specific stress vs. relative density for PLA regular structures – Numerical analysis. 62

Figure 4.11 - Specific stiffness vs. relative density at PLA regular structures – Experimental test. 65

Figure 4.12 - Specific energy absorbed vs. relative density at PLA regular structures – Experimental test. 65

Figure 4.13 - Specific stress vs. relative density at PLA regular structures – Experimental test. 66

Figure 4.14 - Specific stiffness vs. specimen size at PLA graded structures – Numerical analysis. 69

Figure 4.15 - Specific energy absorbed vs. specimen size at PLA graded structures – Numerical analysis. 69

Figure 4.16 - Specific stress vs. relative density at PLA graded structures – Numerical analysis..... 70

Figure 4.17 - Specific stiffness vs. relative density at PLA graded structures - Experimental test. 71

Figure 4.18 - Specific energy absorbed vs. relative density at PLA graded structures - Experimental test. 72

Figure 4.19 - Specific stress vs. relative density at PLA graded structures - Experimental test. 72

Figure 4.20 - Relative Density vs. Thickness-to-Length Ratio on Regular Structures. 76

Figure 4.21 - Specific Stiffness vs. Thickness-to-Length Ratio on Regular Structures. 76

Figure 4.22 - Specific Energy Absorbed vs. Thickness-to-Length Ratio on Regular Structures. 77

Figure 4.23 - Specific Stress vs. Thickness-to-Length Ratio on Regular Structures. 77

Figure A. 1 - Symmetry plans over the honeycomb structure.....	A1
Figure A. 2 - Cut of the honeycomb structure's original model into a quarter.....	A1
Figure A. 3 - Convergence analysis for the full model at various nodes.....	A2
Figure B. 1 - Stress-strain curves for L4 PLA specimens – Experimental testing.....	B2
Figure B. 2 - Stress-strain curves for L6 PLA specimens – Experimental testing.....	B2
Figure B. 3 - Stress-strain curves for L8 PLA specimens – Experimental testing.....	B3
Figure B. 4 - Stress-strain curves for L10 PLA specimens – Experimental testing.....	B3
Figure C. 1 - Specific values of (a) stiffness, (b) energy absorbed and (c) stress vs. specimen size and relative density at PLA regular structures – elasto-plastic numerical analysis.....	C2
Figure C. 2 - Stress-strain curves for L4 at PLA regular structures – Numerical analysis and experimental test.....	C3
Figure C. 3 - Stress-strain curves for $R_1 = +0.31$ at PLA graded structures – Numerical analysis and experimental test.....	C3
Figure C. 4 - Specific values of (a) stiffness, (b) energy absorbed and (c) stress vs. specimen size and relative density at aluminium regular structures – numerical analysis.....	C5
Figure C. 5 - Specific values of (a) stiffness, (b) energy absorbed and (c) stress vs. specimen size and relative density at aluminium regular structures – experimental test.....	C6
Figure C. 6 - Stress-strain curves for L6 at aluminium regular structures – Numerical analysis and experimental test.....	C7
Figure C. 7 - Load vs. Inverse of Squared Core Height for L4 – 66.99 x 64 structure – PLA numerical analysis.....	C8
Figure C. 8 - Load vs. Inverse of Squared Core Height for L6 – 91.15 x 88 structure – PLA numerical analysis.....	C8
Figure C. 9 - Load vs. Inverse of Squared Core Height for L8 – 83.15 x 84 structure – PLA numerical analysis.....	C9
Figure C. 10 - Load vs. Inverse of Squared Core Height for L10 – 100.46 x 102 structure – PLA numerical analysis.....	C9
Figure D. 1 - PLA Specimens of geometries (a) L4, (b) L6, (c) L8, (d) L10.....	D1
Figure D. 2 - PLA specimens of graded structures: (a) "T6-8-10"; (b) "S0.5+_2O"; (c) "S0.5-_2O"; (d) "R1 = +0.31"; (e) "R1 = -0.31".....	D1
Figure D. 3 - Aluminium Specimens of geometries (a) L6, (b) L8, (c) L10.....	D2

List of Tables

Table 3.1 - PLA properties used in the study.	20
Table 3.2 - Considered aluminium properties for the study.	20
Table 3.3 - Characteristics of the hexagonal regular structures.....	21
Table 3.4 - Characteristics of the graded structures (first design method).	23
Table 3.5 - Characteristics of the graded structures (second design method).	23
Table 3.6 - Characteristic of the graded structures (third design method).	26
Table 3.7 - Parameters and simulation time for various meshes (full model).	37
Table 3.8 - List of geometries tested experimentally.....	40
Table 4.1 - Specific energy absorbed, specific stiffness and specific stress for PLA regular structures – Numerical and experimental results.	59
Table 4.2 - Values of specific energy absorbed, specific stiffness and specific stress for only-elastic and elasto-plastic analysis – PLA regular structures.....	63
Table 4.3 - Numerical and experimental values of specific energy absorbed, specific stiffness and specific stress – PLA graded structures (first design method).	66
Table 4.4 - Numerical and experimental values of specific energy absorbed, specific stiffness and specific stress – PLA graded structures (second design method).	67
Table 4.5 - Numerical and experimental values of specific energy absorbed, specific stiffness and specific stress – PLA graded structures (third design method).	67
Table 4.6 - Specific energy absorbed, specific stiffness and specific stress for Aluminium regular structures – Numerical and experimental results.	74
Table A. 1 - Parameters and simulation time for various meshes (quarter model).....	A2
Table A. 2 - Computation of error between both models on various nodes.....	A3
Table B. 1 - Chemical composition of aluminium alloy AlSi7Mg0,6.....	B1
Table B. 2 - Computed values for the Young's Modulus values of PLA specimens.....	B4
Table C. 1 - Error statistics for "h10" aluminium samples.....	C7
Table C. 2 – Slope values of maximum load and critical load linear regressions vs. inverse of squared core height.....	C10

List of Abbreviations, Acronyms, Symbols and Variables

List of Abbreviations and Acronyms

2D	Bidimensional
3D	Tridimensional
ABS	Acrylonitrile Butadiene Styrene
AM	Additive Manufacturing
ASTM	American Society for Testing and Materials
CAD	Computer Aided Design
CFRP	Carbon Fibre Reinforced Polymers
DIN	Deutsches Institut für Normung (German Institute for Standardization)
FDM	Fused Deposition Modeling
FFF	Fused Filament Fabrication
FEA	Finite Element Analysis
FEM	Finite Element Method
FGCM	Functionally Graded Cellular Materials
FGM	Functionally Graded Materials
HOBE	“HOneycomb Before Extrusion”
PC	Polycarbonate
PLA	Polylactic Acid
PP	Polypropylene
PBF	Powder-Bed Fusion
SLM	Selective Laser Melting
SLS	Selective Laser Sintering

List of Symbols

“h”	Structure’s height
“L”	Cell wall length

List of Variables

A_{ref}	Reference area for a unit cell
A_s	Solid material's area
E_s	Young's Modulus of the solid material
E_3^*	Young's Modulus of the cellular material in the out-of-plane direction
$\frac{E_a}{\bar{\rho}}$	Specific energy absorbed
h	Structure's height
I	Moment of inertia
$\frac{K}{\bar{\rho}}$	Specific Stiffness
l	Cell wall length
m_s	Solid material's mass
n	Correction factor for the critical load expression
P_{cr}	Critical load on Euler conditions
R_1	Primary measure of the geometrical gradient
R_2	Secondary measure of the geometrical gradient
t	Cell wall thickness
V_{ref}	Reference volume for a unit cell
V_s	Solid material's volume
ε_N	Nominal (engineering) strain
$\varepsilon_{pl,R}$	True strain's plastic component
ε_R	True strain
$\varepsilon_{tot,R}$	Total strain
ε_y	Strain at yield point
η	Cellular material's porosity
ρ_s	Density of the solid material
$\bar{\rho}$	Relative density
ρ^*	Density of a cellular material
$\frac{\sigma}{\bar{\rho}}$	Specific Stress

$\sigma_{max,N}$	Maximum stress
σ_N	Nominal (engineering) stress
σ_R	True stress
σ_y	Yield strength
$\overline{\sigma_{VM}}$	Average von Mises stress

Chapter 1: Introduction

1.1 Motivation and Objectives

The use of composite materials allows new possibilities in many engineering fields. The search for light-weight materials that have good mechanical properties, especially the ones with high strength and stiffness, encourages the development of new structures, such as sandwich structures and functionally graded materials, with a great variety of applications. In some engineering fields, these have a great importance given the fact that it allows to produce parts with considerable strength and low weight, essential in aerospace, marine and automotive industries. More recently, these materials have gained relevance in medical fields, with the development of manufacturing techniques and materials design. The production of medical imaging equipment and implants made of bio-compatible materials through Additive Manufacturing (AM) is now a promising breakthrough, not only because of fast prototyping (which allows a better product design), but also due to the possibility to manufacturer complex geometries, with a significant decrease in production costs and low waste of material.

The honeycomb structures formed by regular hexagonal cells are the most common cores for sandwich structures due to their light weight. The aviation industry was pioneer in this matter, introducing the first sandwich panel on seaplane pontoons with a core made out of wood [1]. In 1945, the first all-aluminium sandwich panel was made with aluminium facing sheets, possible due to the development of adhesive solutions [1]. Since then, new materials have been chosen to produce these structures, such as stainless steel, titanium and other non-metallic materials (Kraft paper, Nomex and glass fibre) [2]. The honeycomb structures are not only attractive by their mechanical properties, but also by their thermal and acoustic insulation capabilities explored in more recent years [2].

In this work, the out-of-plane mechanical behaviour of functionally graded materials is studied, namely honeycomb structures. The study is conducted both through numerical analysis (using the Finite Element Method) and experimental testing, under conditions of uniaxial compression in the out-of-plane direction. In general, research is more frequent in in-plane directions, although the out-of-plane case also presents some challenges. For this study, honeycombs with regular hexagonal and functionally graded structures were designed varying different parameters in order to study the effects of geometrical gradients on the out-of-plane properties. The specimens for experimental testing were produced in PLA and aluminium, by means of AM processes.

The following objectives were defined for this work:

- Study the effect of geometrical parameters in mechanical properties of regular and functionally graded structures;
- Investigate the possibility of enhancement of mechanical properties in functionally graded structures over the regular ones;
- Evaluate the potential of Additive Manufacturing in honeycomb structures using both traditional materials (aluminium) and new polymeric alternatives (PLA);

- Establish a comparison between Finite Element analysis and experimental testing results.

1.2 Thesis Outline

In this section, the structure of this work is presented along with a brief summary of the chapters and the main topics addressed in each one:

- In the first chapter, an introduction of the work is made, with the motivation for the study of honeycomb structures, some background of the honeycomb structures' applications and the objectives of this work;
- In the second chapter, a bibliographic review on the state-of-the-art and previous works related with cellular materials and functionally graded materials is made, as well as an overview over Additive Manufacturing processes and their importance in functionally graded structures production;
- In the third chapter, the materials used to obtain the specimens are described as well as the design methods for the structures, the computational model for the Finite Element analysis and the experimental test procedure;
- In the fourth chapter, the results obtained in the numerical analyses and the experimental tests are presented, followed by discussion;
- In the fifth chapter, the conclusions from the study are presented, covering the objectives stated on the first chapter. Some suggestions for future work are also presented.

Chapter 2: Literature Review

2.1 Composite Materials

Composite materials are defined as a mixture of two (or more) different types of materials, combined into one. The principal benefit from this combination is the achievement of better mechanical properties, providing new materials with high strength-to-weight ratio. It also allows having materials with specific mechanical, physical, thermal and electrical properties that are much more suitable for a specific application (figure 2.1).

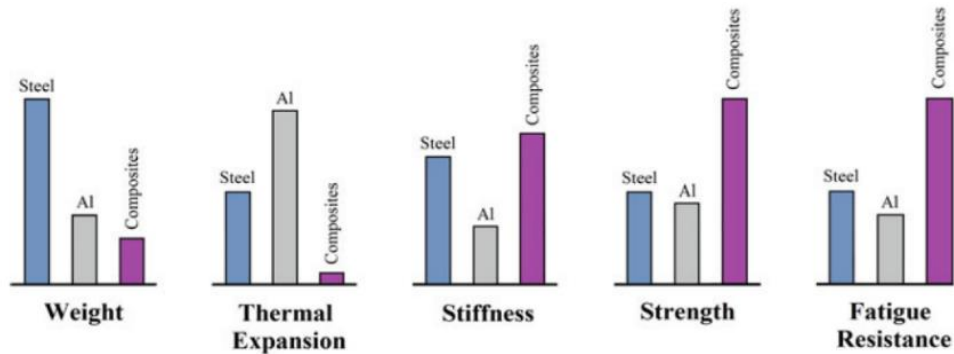


Figure 2.1 - Properties comparison between composite materials, steel and aluminium [3].

The composite materials are constituted by a matrix, which is usually the main material, and a reinforcement phase in forms of particles, fibres or sheets [3]. A very well-known composite structure is the sandwich panel, which is composed by a core embedded between two exterior sheets. The core can have several designs, such as foam, honeycomb, tetrahedral truss or lattice structures (figure 2.2), among others [4-8]. Many core structures are also inspired by biological geometries [4]. The focus of this study will be on honeycomb hexagonal structures.

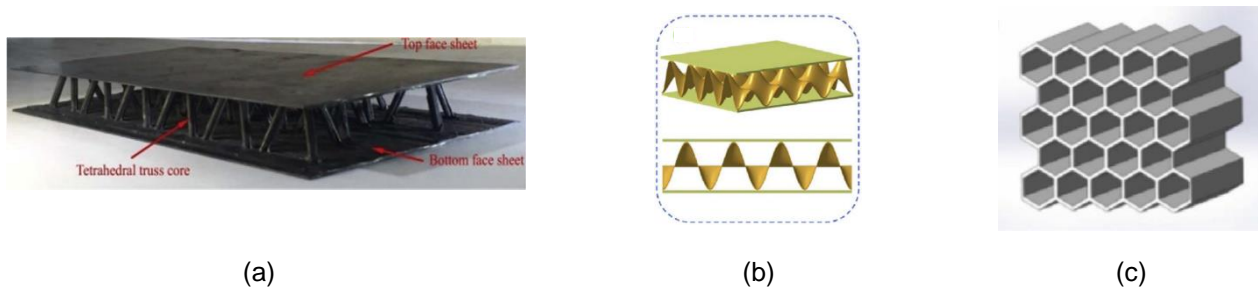


Figure 2.2 - (a) Tetrahedral truss core; Bi-directionally corrugated core (b); Honeycomb core (c) [4].

Honeycomb structures (as mentioned before) are a core solution for sandwich structures (figure 2.3). This type of structures is well known for their capability to absorb high quantities of energy and their high strength-to-weight ratio [9, 10]. This type of structures has also good properties when it comes to thermal and acoustic insulation, and radio frequency shielding [1]. All these properties enable them to be applied in industries such as aerospace, transportation sector [1], civil construction and marine [4].

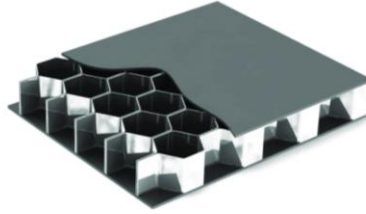


Figure 2.3 - Sandwich structure with honeycomb core [11].

Although in the earlier years the used material for the core was aluminium [1], nowadays the polymeric materials are much more used [9], precisely due to the improvements on materials for composite structures, aiming always for materials with better mechanical properties and less weight.

As a proof of the variety of functions that these structures have, Goodman [12] presents honeycomb structures as a solution for tissue engineering and regenerative medicine, in particular for designing scaphoids, making possible tissue regeneration. The biocompatibility, biodegradability and processability of cyto-compatible hydrogels capable of 3D cell encapsulation are attractive characteristics for tissue regeneration purposes. Goodman [12] also refers applications other than bio-engineering, such as high-performance energy capacitors, water treatment, and solar energy conversion.

2.2 Cellular Materials

2.2.1 Overview

As explained by Gibson and Ashby, cellular materials are formed by small compartments denoted as cells [10]. Bathe et al. [13] define cellular materials as “patterns that may be best defined in contrast to their homogeneous counterparts”; i.e., their heterogeneity in shape confers other properties that may be a benefit rather than if the same materials would be geometrically homogeneous. Figure 2.4 shows the possible applications of cellular materials.

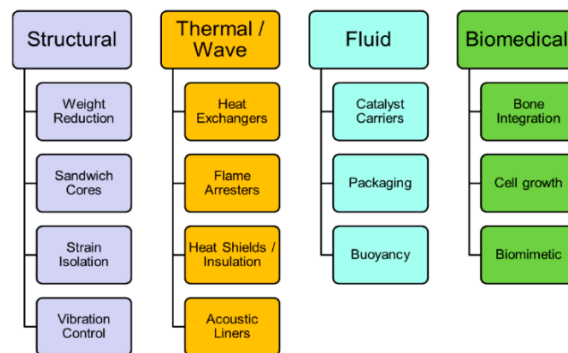


Figure 2.4 - Possible applications of cellular materials [13].

Some examples of cellular materials are cork, wood, marine sponge – as well as corals, bone and honeycombs [14]. Jordi et al. [7] studied nature-inspired structures like bamboo and enamel, proposing them as an alternative to the traditional honeycomb ones.

A cellular material is constituted by a unit cell (a combination of solid and empty space) and the repetition of that unit cell with a certain pattern that may be either regular or variable [10].

There are several classifications of cellular materials. Gibson and Ashby propose to distinguish among two-dimensional (honeycombs) and three-dimensional (foams and lattices).

According to their cells' geometry and microstructure, cellular materials can be grouped (figure 2.5) into the following categories [15]:

- stochastic – cells with random microstructures. These materials are usually called “foams”;
- periodic – cells with patterned microstructures. These materials can be called either “honeycombs” or “prismatic materials”, where lattice structures are included.

Regarding stochastic cells, they can be divided into two types: open or closed cells. These differ in having (or not) solid material along the pores' surface (i.e., the walls of the cells) [10]. Regarding periodic cells, they can be grouped into 2D structures (either honeycombs or prismatic) or 3D (lattice) structures, which may be either truss or textile structures. The difference between honeycombs and prismatic structures are their 2D pattern orientation, having their cross section propagated on the vertical axis or on the horizontal axis, respectively.

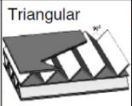
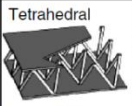
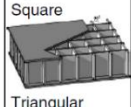
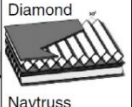
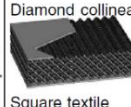
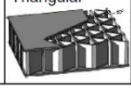
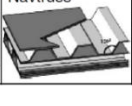
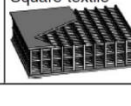
Cellular materials					
Stochastic		Periodic			
Open cell	Closed cell	2D		3D (lattice)	
		Honeycombs	Prismatic	Truss	Textile
					
					
					

Figure 2.5 - Cellular materials classification according to their topology [15].

The lattice structures are characterized by unit cells that are interconnected in three dimensions [16]. Besides the common advantages of composite materials in general (acoustic and vibration damping, high strength-to-weight ratios and good thermal management [16]), Helou and Kara [16] point out the energy absorption capabilities of these structures through the use of hollow trusses. Hollow trusses have a higher load carrying capacity due to a higher second moment of inertia, when comparing to solid trusses.

AM technologies have made more feasible the production of new geometries in cellular materials [5-8, 13]. However, there are some challenges that limit the implementation of AM these materials, such as a lack of methodology regarding structures design and optimization, with view to a specific application [13].

2.2.2 Production Methods of Honeycomb Structures

Since hexagonal honeycomb structures are the subject of study at the present work, only this type of structures will have its manufacturing detailed.

There are five main ways to produce honeycomb structures: thermal fusion, diffusion bonding, brazing, resistance welding and adhesive bonding, apart from AM techniques. Since the most common process is the adhesive bonding [1], only this will be detailed in the next section.

Adhesive bonding consists of using adhesives to gather permanently two different materials. In the case of the honeycomb structures, the core needs to have attached two reinforcements, one of each side. The connecting interfaces between the sheets and the core is called “node”. Inside adhesive bonding, there are two methods to manufacturer the honeycombs: expansion and corrugation.

2.2.2.1 Expansion method

When manufacturing a metallic honeycomb, a resisting coat is applied to the foil sheets that come from the metal, applying also parallel adhesive lines over the sheets. The sheets are then cut and stacked on top of each other. The adhesion of the sheets is accomplished by curing the adhesive under pressure at elevated temperature. This forms the HOBE block (“Honeycomb Before Expansion”), that is cut into “slices” afterwards to confer the intended core height. The sliced HOBEs suffer an expansion by mechanical processes that, with the adhesive conferring adhesion between the sheets, the honeycomb gains its final geometry, being the process terminated (figure 2.6).

For non-metallic materials, the process is the same as above, but it may take some extra steps, as the expansion process might not be able to confer the intended geometry. In this case, the structure is placed on an oven in order to heat small amounts of resin previous placed on the block material. The heat-up will make the structure achieve the final form. In non-metallic honeycombs of larger dimensions, the structures are dipped in liquid resin (usually, phenolic or polyimide) and then cured [1].

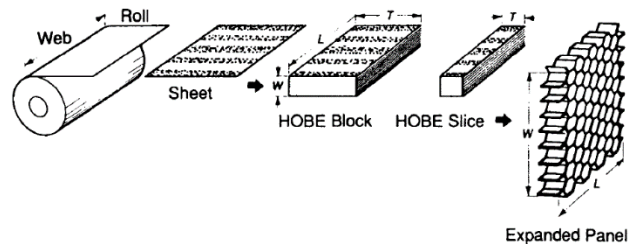


Figure 2.6 - Diagram for the expansion method – honeycomb manufacturing process [1].

2.2.2.2 Corrugation method

In this method, there is a pre-processing of the geometry before introducing the adhesive and assembling the foils. The raw material passes through corrugating rolls, acquiring partially the honeycomb geometry.

Next, the adhesive is applied to the already cut corrugated sheets, and the sheets are stacked, originating a corrugated block with the final geometry. The block is then taken to the oven to cure the adhesive. After the cure, the process is terminated (figure 2.7). Some non-metallic honeycombs might be dipped in resin to achieve more density, as well as more resistance [1].

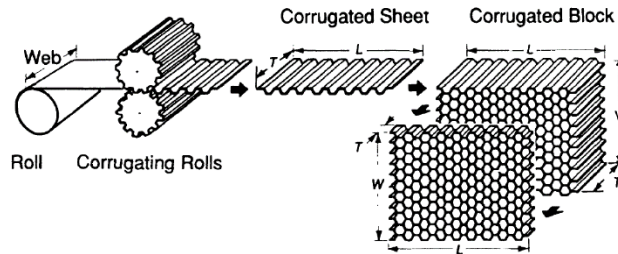


Figure 2.7 - Diagram for the corrugation method – honeycomb manufacturing process [1].

2.3 Additive Manufacturing

Additive manufacturing, frequently referred as “3D printing”, is defined as a type of manufacturing that builds 3D objects joining materials layer by layer, based on computer-aided design 3D models [17]. AM is important for rapid prototyping, thus being commonly used on scientific research facilities and companies which intend to use 3D printing to rapidly create a representation or test a part or system before the final product [18, 19]. Rapid tooling is also very appreciated in the industry context and it is frequent to resort to AM in order to produce manufacturing and assembling tools [18].

AM was introduced in industry in 1980’s decade with the stereolithography machines [18] that make use of photochemical processes to manufacturer the parts. In the latest years, with the development of new technologies and constant decrease of 3D printing costs [19], new types of AM have been emerging and its use has been each time more frequent in industry.

The AM produced parts have a very useful implementation in various sectors, but there is special interest in the industries of [18-20]:

- Automotive: parts prototyping, tools’ production for assembly lines, test components to rehearse assembly processes, parts for sport racing vehicles;
- Aerospace: parts prototyping (possibility to build complex geometries), interior cabin’s components (e.g., overhead compartments), engine components (due to high temperature resistance on AM manufactured materials). It is important to refer the high strength-to-weight ratio, something very important on design, especially at aerospace industry, and common in all applications here referred;
- Medical and healthcare: surgical and diagnostics equipment (imaging devices), prosthetics and implants (with great importance to both orthodoxy and orthopaedical), tissue engineering and medical training models.

AM processes open new possibilities when it comes to design complex geometries, even though the resin injection or machining processes may be more suitable for production purposes of regular honeycomb structures. Comparing to the traditional honeycomb manufacturing processes, AM represents a much more suitable solution to produce graded cellular materials due to its manufacturing easiness on parts with varying geometry and less need of post-processing. Several parts' geometries can be done in one single operation through AM, contrary to many cases using traditional manufacturing processes.

An ASTM committee has categorized AM processes into seven distinct families [20]: Vat photopolymerization, Powder-Bed Fusion (PBF), Binder Jetting, Material Jetting, Sheet Lamination, Material Extrusion and Directed Energy Deposition. Making use of Kruth's classification [20, 22], AM processes can be divided into three groups according to the material's state before the processing: powder, liquid and solid (figure 2.8). For this work, only the used processes to produce the specimens will be detailed, namely Selective Laser Melting (SLM) and Fused Filament Fabrication (FFF).

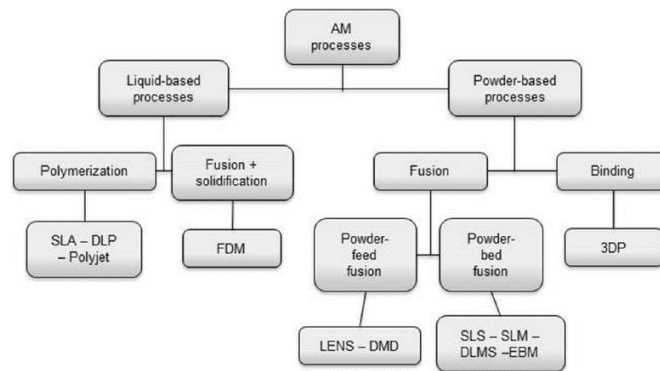


Figure 2.8 - AM processes divided into categories according to the pre-processed material's state [21].

2.3.1 Selective Laser Melting (SLM)

Selective Laser Melting is a Powder-Bed Fusion process, where metallic particles in a powder-bed are melted using a high intensity laser beam, welding these particles to form a specimen with a defined geometry. A powder-based process consists of discrete particles at a container, where a roll transports the powder into the build platform, making the so called “powder bed” (figure 2.9). This method is “selective” in a way that the laser beam points towards powder zones that are within the geometry limits, therefore pointing it to the powder bed particles so they define the geometry contours.

As all AM processes, it is done layer by layer, where the build platform descends as a layer is finished and a new one is produced on top of that one.

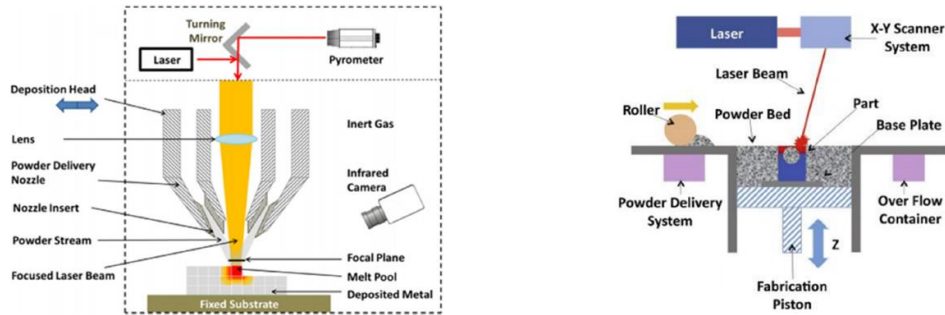


Figure 2.9 - Schematics of the powder-bed fusion process [21].

On SLM manufacturing, the layer thickness varies from 20 μm and 100 μm . During the manufacturing process, an inert gas (usually, argon or nitrogen) flows over the build area in order to prevent oxidation of the powder.

SLM shares the same laser beam method with SLS (Selective Laser Sintering), but in the last one, the laser beam only sinters the powder particles and does not melt them, creating final parts that are more porous. Nevertheless, there is an advantage in using SLS over SLM: it gives the possibility to mix different types of materials, making benefit of final materials with higher strength-to-weight ratio.

SLM manufacturing is mainly applied to metallic materials. Given the fact that the material is powdered, it is possible to mix different metallic materials, resulting in final materials with better mechanical properties, but not necessarily with lighter weight.

2.3.2 Fused Filament Fabrication (FFF)

Fused Filament Fabrication (FFF), adapted from a patented technology called Fused Deposition Modeling (FDM), is a Material Extrusion process where the material is pre-heated to its melting temperature, leaving the extruder nozzle, which has a free 2D movement to draw the geometry layer by layer into an also heated build plate. As a layer is being cooled to the material's solidification point, a new one is being constructed on top of that. The fact that the lower layer is not totally cooled down to the material's solidification point permits adhesion between both layers and enough support to the new one [21].

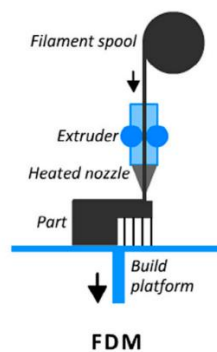


Figure 2.10 - Schematics of FFF process [22].

FFF is currently the most known and most used 3D printing process [18]. The end of exclusive patent rights resulted in a high offer of FFF equipment, which drastically dropped this technology's price [18, 19], making it a very successful AM process.

The most used materials for FFF are the polymers acrylonitrile butadiene styrene (ABS), polylactic acid (PLA) and (polycarbonate) PC [18, 21, 22], even though there are many polymers that may also be applied to this process.

There are a few process parameters (figure 2.11) that will influence the mechanical properties and the part quality [14, 23, 24]:

- the build orientation: the part's orientation relatively to the build platform;
- the layer thickness: often with a value set to 0.2 mm on bi-dimensional structures;
- the air gap between two raster's paths on the same layer;
- the raster angle: the angle between the raster pattern and a defined axis (usually the x - axis) at the bottom layer. It varies between 0 to 90 degrees;
- the raster width;
- the infill density: the measure of "porosity" upon printing;
- the printing speed;
- the extrusion temperature;
- the build platform temperature.

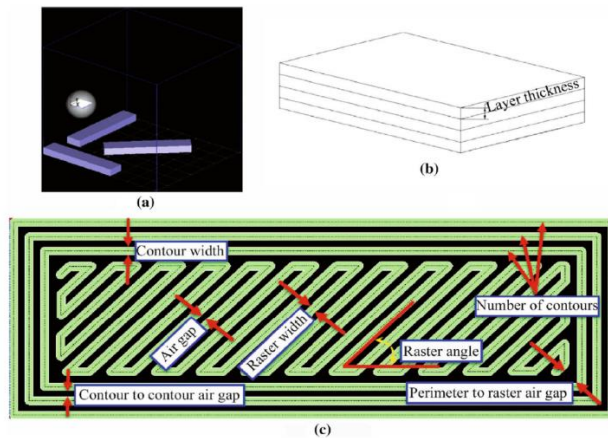


Figure 2.11 - Representation of FFF process parameters: (a) build orientations, layer thickness (b) and (c) FFF tool path parameters.

In Carneiro et al. [25], test samples were printed resorting to FFF, where the used material was polypropylene (PP). The studies concluded that the specimen printed with a raster angle of 0 degrees was the one that performed better, expressed by the highest values of Young's Modulus and ultimate tensile strength. The specimen with a 45-degree raster angle was the one that performed worst, with the lowest ultimate tensile strength. Regarding the layer thickness, between two specimens with 0.20 mm and 0.35 mm, the studies concluded that the second sample performed better than the first one, explaining that it

might be attributed to a lower number of layers, resulting in less interfaces, and therefore more cohesion in the part. The Young's Modulus was the same in both specimens. Lastly, the effect of the infill was evaluated between three different infill densities (20%, 60% and 100%). It was concluded that the effect of the infill density over the mechanical properties was linear: the higher the infill is, the higher the Young's Modulus and ultimate tensile strength are.

2.4 Functionally Graded Materials

2.4.1 Previous works

Functionally graded materials – or simply, FGM – might be defined as heterogeneous materials that are designed to have gradually their properties changing according to the change of the composition or microstructure “over the volume” [26]. A functionally graded cellular material (FGCM) is a combination of a FGM with a cellular material, which benefits from cellular materials plus the possibility to arrange them according to the desired application.

Past studies have shown that the use of FGCM to design honeycomb structures varying geometrical properties had great impact in energy absorption. For example, Taylor et al. [27] have shown that in-plane Modulus could be improved up to 75% with FGCM structures. In another study, Ali et al. [28] studied the effect of a graded wall thickness over a honeycomb structure, showing clearly that graded structures have a much higher energy absorption at impact than regular structures, absorbing especially the plastic energy on an impact.

Some types of functionally graded structures have proven to be an excellent alternative to the traditional regular structures. Fang et al. [29] have studied hierarchical honeycombs under out-of-plane crushing conditions. Hierarchical honeycombs are structures where the side of a hexagon is replaced by smaller hexagons, creating a hierarchy with different levels of increasing density called “order”. In this study, it was concluded that these structures had a significantly higher plateau stress when compared to regular honeycomb structures and even a larger difference when compared with aluminium foams. Also, Fang et al. concluded that the higher the structure's order is, the higher the plateau stress is, proving to be more promising in energy absorption applications. Regarding to thickness-to-cell length ratio, the study concluded that the higher this ratio is, the more the energy absorption is enhanced.

Yet regarding to hierarchical honeycomb structures, Zhang et al. [30] studied “fractal-appearing” structures under out-of-plane crushing conditions, with organisational levels up to second order. The study also comprised parametric studies on geometry changes (in the same structures), such as cell length, wall thickness and specimen's overall dimension. One of the main conclusions was that first order hierarchical structures have an improvement of energy absorption of 38.8% relatively to regular structures, and that second order structures have an improvement of 37.6% relatively to the first order. In what concerns to load response, it was concluded that higher hierarchical orders lead to more stable load responses, implying a smoother transition from elastic region to plastic region. Regarding the parametric studies on the specimens' geometry, it was possible to verify that, with cell lengths changing in second order hierarchical structures,

the energy absorption and the densification strain are greatly affected, being the highest energy absorbed value 47.3% higher than the lowest one. Further into detail, densification strains have multiple value peaks on different cell length combinations. This is due to the structural porosity distribution that changes according to that combination. Relatively to the effect of cell thickness, results showed that the specific energy absorbed and peak crushing force increase with the cell wall thickness, with an intensification trend following the increment of hierarchical order. Lastly, specimen overall dimensions are evaluated, with a change on the cell numbers. Zhang et al. concluded that load response “increase sharply” with the specimen dimension, as well as the energy absorbed. However, reaching a specimen dimension of 9 x 9 (number of cells), the crushing force efficiency and mean plateau stress tend to stabilise, suggesting there is a specimen dimension limit where the mechanical properties of hierarchical structures optimize.

In a study performed by Choy et al. [31], the energy absorption in functionally graded materials is evaluated with in-plane compression of a lattice structure, produced with Selective Laser Melting (SLM). The aim of the study is to evaluate how much can an additive-manufactured FGM structure absorb energy, highlighting the importance of AM that provides the possibility to reduce the production time, while manufacturing the intended geometry with a varying composition of the materials, which are two primary characteristics of FGM structures. Concerning energy absorption and compressive strength, FGM structures showed significantly higher values, relatively to regular structures, for the energy absorbed and the plateau stress, with increases varying from 10% to 72% and from 19% to 67%, respectively. This study had its results in accordance with a similar study [32] that also resorted to SLM to manufacture a graded lattice structure, where it was also concluded that FGM structures performed better in energy absorption than regular structures, although it is less visible here than in Choy et al. study. Regarding the AM technique, the study concluded that SLM process can produce lattice struts with near full density, which indicates that this technique is a viable option for metallic FGM structures manufacturing.

FGM structures may also be accomplished by the introduction of wall thickness gradients with consecutive cell length variation, which implies change in the relative density of structures. Silva [23] studied (numerically and experimentally) the effect of in-plane gradient applied to honeycomb, plateau and lotus structures, also differing in in-plane orientation of the unit cells (0 and 90 degrees). The study was conducted under bending conditions. The specimens were produced in PLA and aluminium materials, both 3D-printed (FFF and SLM, respectively). It was introduced a variable that measures the gradient of the cell wall thickness called “G parameter”. Structures with different cores and multiple G parameters were produced. Silva concluded that FGM structures performed overall better than non-graded structures in terms of strength, stiffness and energy absorbed. Although in some results the tendency was not exhibited, the study concludes that, the greater the gradient is, the better the structures perform. Regarding the morphology of the unit cell, without taking the in-plane orientation into account, the results indicate that the lotus structure is the one with better stiffness and energy absorption, followed by plateau and honeycomb. Taking into account the 90-degree orientation, results showed that the structures that performed better in stiffness and energy absorption were

the honeycomb and plateau, respectively. This study validates, once again, the potential of FGM as a replacement of the traditional honeycomb structures.

Functionally graded materials designs have also great importance in the bio-medical field. Limmahakhun et al. [33] studied cobalt chromium (CoCr) graded materials regarding their stiffness and strength for stress-shielding reduction. The use of these materials for orthopaedic implants has a great potential, since they have similar mechanical properties to natural bone. Besides its bio-compatibility, CoCr graded structures allow not only a higher energy absorption than bones, but also a maximised proximal stress transfer to bones, which prevents implant loosening, therefore avoiding punctual interventions for implant correction. The study also compared graded structures with regular ones, with the first ones showing improvements on energy absorption and compressive strength handling.

Further into detail on previous works, Yu et al. [34] studied the effect of matrix shear strength on CFRP (carbon fibre reinforced polymers) under conditions of out-of-plane compression, configured as cross-ply (fibres aligned alternately at 0/90 degrees by layers). The study shows that compressive strength increases as the specimen size increases. This is explained by the presence of shear lag zones at the periphery of the specimen, evidenced by the pressure build up from the periphery towards the centre. Moreover, the magnitude of the size effect decreases with the increasing “state of cure”, being proved by the study that, for fully cured laminates, “the compressive strength was insensitive to specimen size”.

In a different work, Yu et al. [35] studied the effect of graded square honeycombs as sandwich core under out-of-plane uniform pressure loading. The authors propose the introduction of gradient using a non-uniform mass distribution, with the structure’s total mass constrained. This may be achieved by two approaches: wall thickness variation and cell length variation. The study concluded that, using both the approaches, the structures’ performance in stiffness, strength and plastic energy dissipation was better with positive gradients, rather than negative or null gradients; i.e., placing a higher mass concentration next to the symmetry planes. The mentioned higher mass concentration can be done either by increasing the thickness of the ribs that are close to the symmetry planes or moving the ribs towards the symmetry planes. This is evidenced by the marked sensitivity in thickness change of the ribs that are closer to the symmetry planes.

AM is considered to be very important in the conception of sandwich structures due to its ability to manufacturer complex geometries, allowing optimized structures in terms of energy absorption and stiffness. Schwenke and Krause [36] have developed optimised direct load-paths in the core of sandwich structures for load introduction points (figure 2.12). The introduction of already optimised inserts on the core allows the reduction of stiffness discontinuity at the interface. The insert adheres to the core structures through adhesive use.

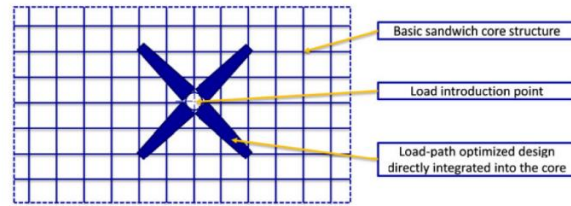


Figure 2.12 - Example of an insert at a sandwich core structure [36].

The results from the study concluded that, on an out-of-plane tensile test, the stiffness is improved by over 50% and the maximum “pull-out force” (force exerted in the out-of-plane direction) is increased by 120%. The authors highlight the great importance of AM given the complexity of the insert’s geometry, proving once again that AM is a great asset to achieve “made-to-measure” structures that satisfy several engineering requirements.

The morphology of the unit cells has also a considerable influence on how the honeycomb structures behave regarding energy absorption and mechanical properties. All the following referred works have their samples 3D-printed with PLA material.

Several works have studied the effect of the core topology on the mechanical properties of sandwich panels. Araújo et al. [5] studied different morphologies for the unit cells (regular hexagonal, lotus and plateau), with different orientations relatively to the load, to assess in-plane properties under compression conditions. The study comprised both Finite Element Method (FEM) simulation and experimental testing on FFF-printed specimens. It was possible to conclude that the lotus arrangement has the highest values of strength and stiffness, followed by the plateau arrangement and then the regular hexagonal one. In terms of elastic energy absorption, generally the regular hexagonal arrangement has the highest value, followed by the plateau and then the lotus one. There is an exception in this trend, where with the orientation of 90 degrees, the order from the highest to the lowest value is lotus, regular hexagonal and plateau. The study presents bending phenomena of the cell walls in the direction of the load as a possible cause to low values of in-plane strength and stiffness.

Bru et al. [7] proposed other unit cell morphologies inspired in natural structures. At this study, the authors propose two novel cores with enamel and bamboo structures, subjected to in-plane compression and three-point bending tests, using both a numerical (FEM) and experimental approach. To conduct the study, honeycomb, enamel and bamboo cores were produced, with different cell thickness in each structure type. Regarding bamboo structures, they are graded due to the distribution of the fibres, with distinction whether the gradient is defined in the longitudinal direction (“Bamboo_L”) or in the transverse direction (“Bamboo_T”). It was possible to conclude that, regarding the compression tests, the honeycomb and enamel structures decrease their maximum stress value and increase their stiffness and energy absorbed values as the relative density increases. In “Bamboo_L” structures, the case was different: with the increase of relative density, maximum stress increased but both stiffness and energy absorbed decreased. “Bamboo_T” structures also have a different behaviour: with the increase of relative density, maximum

stress decreased but both stiffness and energy absorbed increased. Overall, under compression conditions, the highest stiffness and lowest stress values were registered on bamboo structures, with, generally, the highest energy absorbed for “Bamboo_T”. On the three-point bending tests, the behaviour on the structures didn’t follow a trend as in the compression tests. Nevertheless, in bending conditions, bamboo structures performed better in stiffness and energy absorption, although the lowest stress levels had been registered for enamel structures. To conclude, the authors state the potential of enamel and bamboo structures as an alternative to the traditional honeycomb structures. It was also concluded that there is a good results’ agreement between FEM analysis and experimental testing.

Miranda et al. [6] made a detailed study of polymeric and metallic (additively manufactured by FFF, SLM and machined) honeycomb structures, with different unit cell morphologies and orientations, resorting to three-point bending testing. Honeycomb, lotus and plateau configurations with 0, 45 and 90 degrees (in-plane orientation) were tested. Both FEM analysis and experimental tests showed that 0-degree oriented structures are the ones with highest stiffness and energy absorbed, being the 45-degree oriented with the lowest values of stiffness and energy absorption. Keeping the in-plane orientation constant, lotus configuration showed higher stiffness as well as higher energy absorbed. It is then concluded that lotus and plateau arrangements have great potential to replace traditional honeycombs as core structures when it comes to in-plane properties.

Geramizadeh et al. [37] studied the effect of morphology changes of unit cells in out-of-plane energy absorption of sandwich structures. The study was conducted both numerically (in *ABAQUS* software) and experimentally, using test conditions of uni-axial compression and three-point bending (3PB). Two prototypes were elaborated to FFF. In the first one (Beta VI), splines were used to replace the four diagonal walls of unit cells, leaving the two vertical walls without any change. In the second one (Alpha VI), the first prototype had its angles on the vertical walls filleted, creating all-round unit cells. The study concluded that, in the 3PB test, Beta VI and Alpha VI performed better than regular honeycomb structure, with improvements in energy absorption of 23.7% and 53.9%, respectively. Furthermore, in the uniaxial compression test, squared structures with variable number of cells had different performances. The authors concluded that the number of unit cells has a significant impact on energy absorption and ultimate strength until a certain dimension. In this study, the results showed that the stress-strain curves for the specimens 6 x 6 and 8 x 8 (number of unit cells) are the same in the elastic region, meaning that there is no influence (in this case) on structures properties for specimens larger than 6 x 6-unit cells. It was also concluded that the finite elements method’s results and experimental results have good accordance, being FEM a good alternative to evaluate sandwich structures’ behaviour.

Tao et al. [38] studied the effect of in-plane gradients in the out-of-plane crushing strength and energy absorption of honeycomb structures. The gradients were introduced by changing the thickness of the cells walls along their side length, originating three structures with positive or negative gradients and null gradient (regular honeycomb). The results showed that positive gradients (more mass concentration towards the centre) enhance greatly the energy absorption, with an increase of 68.5% over the regular structure in

energy absorption. The study also concludes that crushing strength increases linearly with the increment of the gradient.

In general, the out-of-plane properties of sandwich panels are not so extensively studied as the in-plane behaviour. For example, Kumar et al. [39] found that the ultimate compressive strength of a sandwich panel decreases with increasing core height, independently of the cell lengths studied. For other structures proposed by Townsend et al. [40], there may be the possibility to tailor the amount of energy absorbed under out-of-plane compression, designing several cell lengths and wall thickness of honeycomb structures.

2.4.2 Relative density

One of the key properties regarding cellular materials is the relative density, $\bar{\rho}$. As different core structures may have different densities due to their geometry and material or physical properties, this property plays a very important role when comparing performances between cellular structures. Relative density is defined by the fraction between the density of the cellular material (ρ^*) and the density of the solid material that constitutes the material (ρ_s) [10]. There are different designations for cellular materials depending on their “level of porosity”. A material with $\bar{\rho} < 0.3$ is considered to be a cellular solid, whereas a material with $\bar{\rho} \geq 0.8$ is considered to be a solid with isolated pores [10]. For purposes of scaling, relative densities of some materials are given: polymeric foams – from 0.05 to 0.2; cork – 0.14; most softwoods – from 0.15 to 0.40.

There are alternative ways to define relative density, based on the structure’s geometrical entities. For instance, it can be defined by a fraction between the volume of solid material (V_s) contained on a reference volume (V_{ref}) and the reference volume. This reference volume may be set around a vertex common to various unit cells. Given the core structure is a two-dimensional entity, this fraction may even be simplified to the area of solid material (A_s) over the reference area (A_{ref}). This deduction is detailed on equation 2.1, where m_s stands for the mass of solid [10].

$$\bar{\rho} = \frac{\rho^*}{\rho_s} = \frac{m_s}{V_{ref}} * \frac{V_s}{m_s} = \frac{V_s}{V_{ref}} \Leftrightarrow \bar{\rho} = \frac{A_s}{A_{ref}} \quad 2.1$$

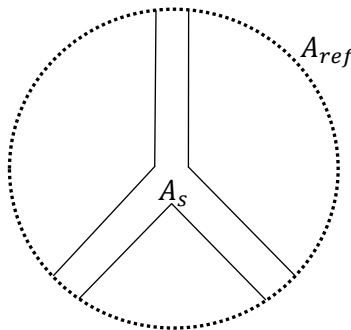


Figure 2.13 - Reference area on a unit cell.

The relative density can also be expressed in terms of the material's porosity, η [10]:

$$\bar{\rho} + \eta = 1 \quad 2.2$$

According to Gibson and Ashby, the relative density for regular hexagonal honeycombs may be expressed in function of the ratio wall thickness-to-cell length size, corrected of a factor (C) near unity that is computed in accordance with the cell shape [10]:

$$\frac{\rho^*}{\rho_s} = C * \frac{t}{l} \quad 2.3$$

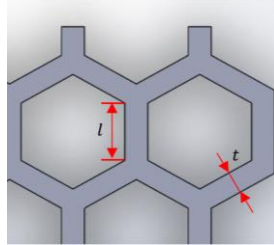


Figure 2.14 - Schematics of the unit cell and geometric variables.

Although there is a correction coefficient to calculate the relative density for this type of structure, when the thickness-to-length ratio is large, the expression above may introduce deviation from the actual value; hence, it is necessary to reformulate the derivation. Gibson and Ashby propose the following expression [10]:

$$\frac{\rho^*}{\rho_s} = \frac{2}{\sqrt{3}} \frac{t}{l} * \left(1 - \frac{1}{2\sqrt{3}} \frac{t}{l}\right) \quad 2.4$$

2.4.3 Out-of-Plane Mechanical Properties

Honeycomb structures have great mechanical properties in situations of out-of-plane loading. They are usually stiffer and stronger (i.e., with better strength performance) when loaded on their out-of-plane direction [10]. The following properties are assumed for low densities ($t \ll l$).

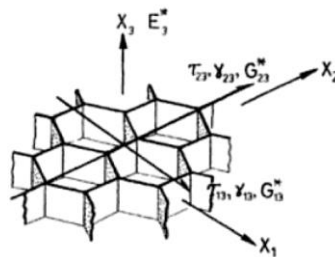


Figure 2.15 - Out-of-plane properties for honeycomb structures [10].

According to the reference, the solid Young's Modulus can be related with the X3-direction Young's Modulus, making use of the thickness-to-length ratio:

$$\frac{E_3^*}{E_s} = \frac{t}{l} \quad 2.5$$

Recalling equation 2.3 and considering C is a value near 1, it is possible to establish a connection between both Young's Modulus and the relative density:

$$\frac{E_3^*}{E_s} = \frac{\rho^*}{\rho_s} = \bar{\rho} \quad 2.6$$

It is necessary to mention that, due to the constant factor, the error between both expressions (2.3 and 2.6) may increase as its value decreases.

Among the assumptions that will be used for cellular materials when applying an out-of-plane loading, one has to take into account that, particularly in the case of open cells, foams may be taken as columns where a vertical load is applied. In this case, it is possible to have to have instabilities (Euler conditions), being the critical load (P_{cr}) inversely proportional to the length of the column (h), where n is a correction factor, E_s is the Young's Modulus of the material and I is the second moment of area of the column axis [41]:

$$P_{cr} = \frac{n^2 * \pi^2 * E_s * I}{h^2} \quad 2.7$$

Chapter 3: Materials and Methods

3.1 Materials properties

3.1.1 PLA

PLA stands for polylactic acid and it is a polymer made entirely out of renewable resources that provide lactic acid. The good physical and mechanical properties as well as the associated low production costs, along with the fact that it is a biodegradable material, makes PLA very attractive for several applications, having emerged as an alternative to the traditional petrochemical-based plastics.

The material used for the specimens obtained in the present work was purchased from Filkemp, as shown in figure 3.1. As there wasn't a data sheet available, the properties displayed in table 3.1 below are taken from previous works [14, 23], which already result in averaged values from different raster angles upon printing the test specimens to determine PLA properties. Regarding the Young's Modulus, the value hereby used is an average between the ones referred at Miranda [14] and Silva [23].



Figure 3.1 - Filkemp PLA filament.

As mentioned further ahead, the FEM software uses true values of stress and strain. Therefore, it is necessary to obtain the true values as a function of the nominal (engineering) ones.

The true stress (σ_R) and strain (ε_R) values are dependent on nominal (or engineering) strain (ε_N) and nominal (or engineering) stress (σ_N) as follows:

$$\sigma_R = \sigma_N (1 + \varepsilon_N) \quad 3.1$$

$$\varepsilon_R = \ln (1 + \varepsilon_N) \quad 3.2$$

The nominal strain at yield can be obtained using the equation of the elastic zone:

$$\varepsilon_y = \frac{\sigma_y}{E} \quad 3.3$$

It is necessary to calculate the plastic component of the true strain ($\varepsilon_{pl,R}$), a fundamental parameter to define the material behavior at the FEM software. In order to isolate the real strain's plastic component, the elastic component must be subtracted to the total strain ($\varepsilon_{tot,R}$), where the maximum point on the material's curve ($\varepsilon_{tot,N}$, $\sigma_{max,N}$) is usually given by the manufacturer on the material's data sheet. This operation can be performed using the equation 3.4:

$$\varepsilon_{pl,R} = \varepsilon_{tot,R} - \frac{\sigma_{max,R}}{E} \quad 3.4$$

Table 3.1 details the considered mechanical and physical properties for PLA.

Table 3.1 - PLA properties used in the study.

Density [g/cm ³]	Young's Modulus [MPa]	Poisson's Ratio	Yield Strength [MPa]		Tensile Strength [MPa]		Maximum Plastic Strain	
			Nominal	True	Nominal	True	Nominal	True
1.252	1500	0.36						
			25	26	49	51	---	0.008

3.1.2 Aluminium

The aluminium alloy used for this work was produced using SLM technology. The present alloy is designated as AISi7Mg0,6, manufactured by SLM Solutions Group AG in accordance with the DIN EN 1706/EN AC-42200 standards. The considered material properties are shown on table 3.2. Regarding the Poisson's Ratio, it was considered a standard value of 0.33, typical for aluminium alloys, as this information wasn't available from the manufacturer's data sheet. The true values were computed following the equations 3.1 to 3.4.

Table 3.2 - Considered aluminium properties for the study.

Density [g/cm ³]	Young's Modulus [MPa]	Poisson Ratio	Yield Strength [MPa]		Tensile Strength [MPa]		Maximum Plastic Strain	
			Nominal	True	Nominal	Real	Nominal	True
2.680	59000	0.33						
			211	212	375	405	---	0.070

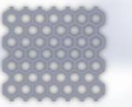
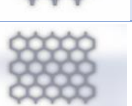
3.2 Modelling of CAD-3D Geometries

The 3D geometries are organized in groups according to the wall thickness design method for both regular and graded structures. The principle dimensional properties on the design process are the cell length, l , and the core height, h .

3.2.1 Regular Structures

Regarding the regular wall thickness honeycombs, the wall thickness, t , was set at 2,31 mm, so that the difference between the various regular geometries is their cell length and core height. For each cell length, l , two structures with different area and with different core heights, h , were designed. Table 3.3 contains the designed regular structures characteristics. The experimental specimens can be found at appendix D.

Table 3.3 - Characteristics of the hexagonal regular structures.

l [mm]	Specimen size [mm ²]	Solid area [mm ²]	$\bar{\rho}$	Specimen's image	h [mm]
4 ("L4")	48.51 x 48 = = 2328.48	1021.38	0.439		6
					10
					12
6 ("L6")	66.99 x 64 = = 4287.36	1879.45	0.438		6
					10
					12
8 ("L8")	65.81 x 66 = = 4343.46	1449.63	0.338		6
					10
					12
10 ("L10")	91.15 x 88 = = 8021.20	2653.95	0.331		6
					10
					12
6 ("L6")	50.82 x 56 = = 2845.92	775.68	0.273		6
					10
					12
8 ("L8")	83.15 x 84 = = 6984.60	1881.23	0.269		6
					10
					12
10 ("L10")	61.20 x 68 = = 4161.60	948.43	0.228		6
					10
					12
10 ("L10")	100.46 x 102 = = 10246.92	2309.45	0.225		6
					10
					12

3.2.2 Graded Structures

With respect to the graded structures, several geometries were made as a result of the different design methods.

All the designs on graded structures were based on radial symmetry: the gradient effect must be propagated in all symmetry directions, making the honeycomb core as even as possible.

Analysing a generic hexagonal regular core, it is possible to identify six lines of symmetry (figure 3.2), corresponding to those ones passing the mid-point of each hexagon side.

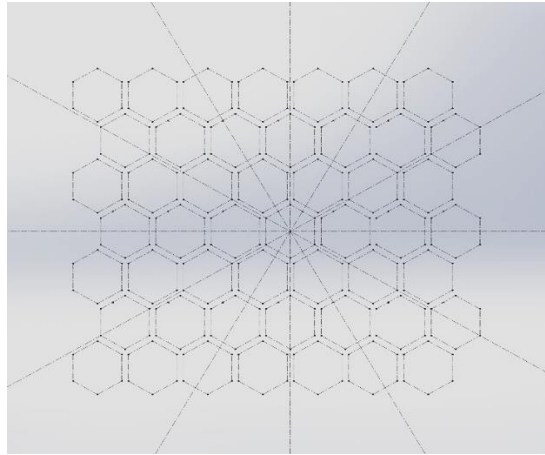


Figure 3.2 - Symmetry lines for the considered honeycomb graded structures.

The application of a gradient, along with the imposed six-line symmetry, results in the appearance of concentric circumferences composed by cells with same cell length l , from now on referred as belts (figure 3.3). Further ahead, it will be explained how the radial distance between the belts differs based on the type of symmetry lines (main or secondary).

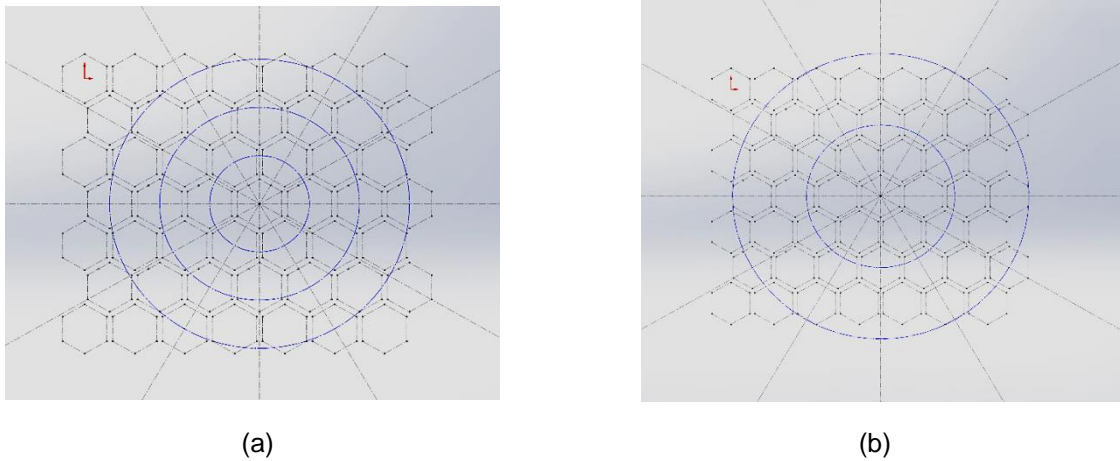
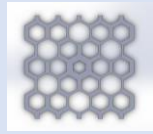
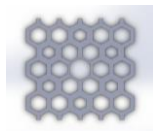
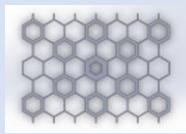


Figure 3.3 - Belts for (a) main and (b) secondary symmetry lines.

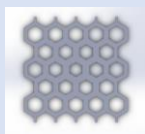
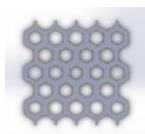
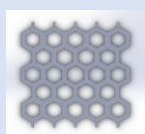
In the first design method, the cell length was the design characteristic; therefore, the wall thickness is a consequence of the imposed cell length. The core height was maintained constant (12 mm). Three variants were made: decreasing (cell length 6-8-10 mm) and increasing (cell length 10-8-6 mm) wall thickness, and a staggered gradient tendency (cell length 6-10-8 mm). The referred cell lengths are ordered by the direction from the centre cell to the ends. Table 3.4 shows the graded structures of the first design method.

Table 3.4 - Characteristics of the graded structures (first design method).

Configuration	Specimen size [mm ²]	Solid area [mm ²]	$\bar{\rho}$	Specimen's image	h [mm]
6 – 8 – 10 ("T6-8-10")	91.59 x 91.35 = = 8366.47	2698.21	0.322		12
10 – 8 – 6 ("T10-8-6")	91.59 x 91.35 = = 8366.47	3514.44	0.421		12
6 – 10 – 8 ("T6-10-8")	129.50 x 95.42 = = 12356.89	2483.73	0.201		12

In the second method, the increment in the cell length was the design characteristic, thus the cell length itself as well as the wall thickness appear as consequence of this increment. Again, the core height was kept constant (6 mm). Four different designs were considered: two with increasing density and two with decreasing density, from the centre to the corners, in which there are two alternatives for the cell length near the corners. The cell length varies between 7 and 9 mm, with a constant increase (or decrease) of 0.5 mm between cells. Table 3.5 shows the graded structures of the second design method.

Table 3.5 - Characteristics of the graded structures (second design method).

Configuration	Specimen size [mm ²]	Solid area [mm ²]	$\bar{\rho}$	Specimen's image	h [mm]
Decreasing density – 1st option ("S0.5+_10")	100.46 x 102 = = 10246.92	4534.70	0.443		12
Decreasing density – 2nd option ("S0.5+_20")	100.46 x 102 = = 10246.92	4776.32	0.466		12
Increasing density – 1st option ("S0.5-_10")	100.46 x 102 = = 10246.92	4368.43	0.426		12
Increasing density – 2nd option ("S0.5-_20")	100.46 x 102 = = 10246.92	4202.15	0.410		12

Finally, for the third method, graded structures were designed following two gradient parameters denoted R_1 and R_2 .

The R_1 parameter defines the cell length increment along the main symmetry lines, as a result of the first increment – from the centre cell to its first neighbours. The parameter is the slope of a linear function of two fractions: $\frac{x_i}{L^*}$ versus $\frac{d_i}{l}$, where:

- L^* represents the distance from the more distant wall of the centre cell to the side end of the structure;
- x_i represents the distance from the origin of the length L^* to the end of the i cell, along a main symmetry line;
- d_i represents the in-plane thickness of the i cell;
- l represents half of the base cell length.

The geometric parameters above mentioned can be seen in figure 3.4. The figure 3.5 shows the $\frac{x_i}{L^*}$ vs. $\frac{d_i}{l}$ plot, where it is possible to calculate the R_1 parameter.

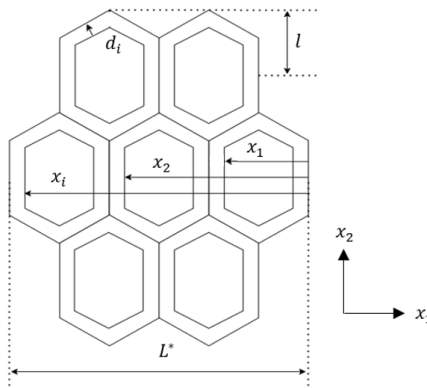


Figure 3.4 - Considered distance variables for R1 calculations.

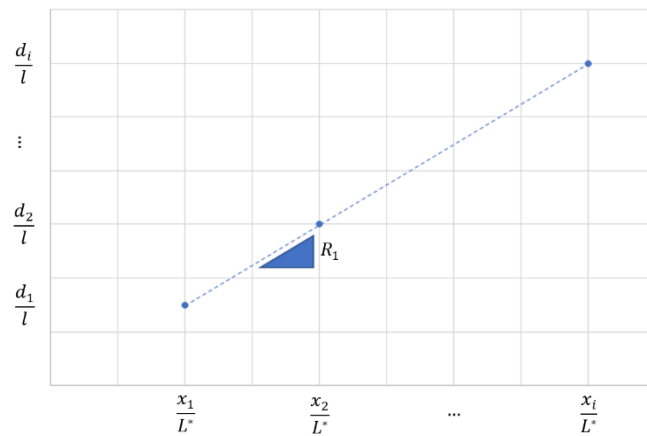


Figure 3.5 - R1 function for honeycomb graded structures.

The R_1 belts are concentric on the origin and distanced equally according to $k_1 = 2 * l_{base\ cell} * \cos\frac{\pi}{6}$.

The R_2 parameter is dependent on R_1 and defines the cell length increment along the secondary symmetry lines. The parameter can be calculated as the following: $R_2 = \frac{R_1}{3 * l_{base\ cell}}$. Like the R_1 belts, R_2 belts are concentric and the distance between them is $k_2 = 3 * l_{base\ cell}$. Its radius is expressed by the variable r , as illustrated on figure 3.6.

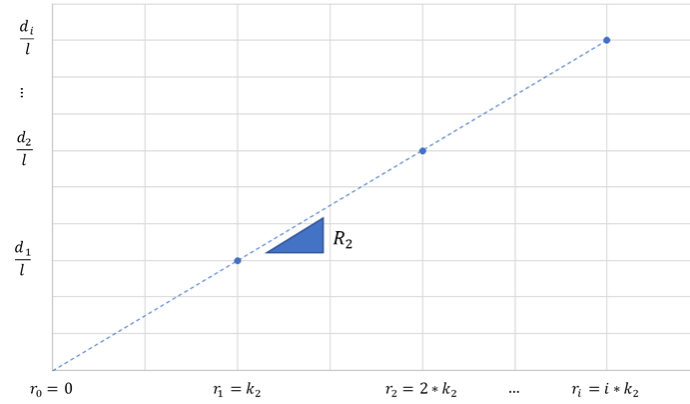
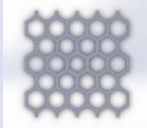
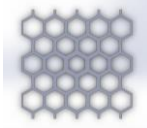
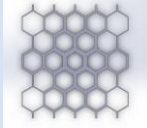
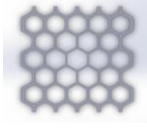
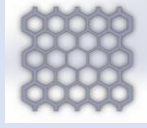
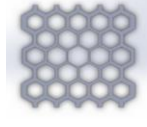


Figure 3.6 - R_2 function for honeycomb graded structures.

For this work, a total of six graded structures were designed according to this method: three on positive linear gradients (decreasing density from centre to the corners) and three on negative linear gradients (increasing density from centre to the corners). Table 3.6 shows the graded structures of the third design method.

Table 3.6 - Characteristic of the graded structures (third design method).

R_1 coefficient	Specimen size [mm ²]	Solid area [mm ²]	$\bar{\rho}$	Specimen's image	h [mm]
+ 0.22	88.51 x 90 = = 7965.90	2572.60	0.323		12
+ 0.31	88.51 x 90 = = 7965.90	2113.53	0.265		12
+ 0.37	88.51 x 90 = = 7965.90	1584.65	0.199		12
- 0.22	88.51 x 90 = = 7965.90	1910.90	0.240		12
- 0.31	88.51 x 90 = = 7965.90	2371.00	0.298		12
- 0.37	88.51 x 90 = = 7965.90	2668.46	0.335		12

3.3 Numerical Methodology

3.3.1 Computational model

For this work, the Finite Element Method was the adopted procedure for the numerical model, making use of the software *ABAQUS 2017*. The model was created under the “Standard & Explicit” model option.

The model consists of a uniaxial compression test, with two plates and the core of the honeycomb structure between them, being the lower plate static and the upper plate moving downwards at constant speed under a specified displacement on the simulation. The model was configured under the elasto-plastic regime for the regular PLA models and under only-elastic regime for all the remaining models (both PLA and Aluminium).

In this section, the model will be explained in detail, namely regarding the material properties, the compression test assembly and the boundary conditions, as well as the simulation parameters and the mesh configuration.

It is important to underline the following: ABAQUS does not have sensibility to units throughout the entire model. Thus, it is important to define the units used for the following parameters:

- For distance, the used unit is millimetre (mm);
- For force, the used unit is newton (N).

This implies that, relatively to the:

- Energy, the unit is millijoule (mJ);
- Stresses, the unit is megapascal (MPa) or newton per square millimetre (N/mm²);
- Densities, the units are tons per cubic millimetre (ton/mm³).

3.3.1.1 “Part” module

The first step in the model's build-up is to import and/or to create the intervening parts on the simulation. In this case, there are three: the honeycomb structure and the two compression plates (parts belonging to the compression test equipment). The procedure adopted for this module was to import a .IGS file of the structure (exported on the CAD software) and to create the two compression plates using ABAQUS tools, both with 5 mm of height. All the three parts were imported or created as “Deformable” bodies, modelled on a 3D space (as illustrated below).

It is important to make sure that, when importing or creating a new part, the scale option under “Scale” tab is turned off to prevent scaling incompatibilities between parts and avoid non-matching results.

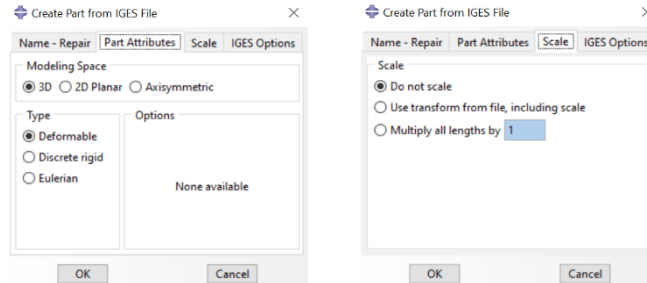


Figure 3.7 - Importing/creating a new part – “Part” module.

3.3.1.2 “Property” module

This module consists of inserting the properties of the materials used, creating sections and assigning them to each part. A section is a continuous closed region with the same material properties. Therefore, it will be created two sections: one for the structure, and another for both plates, each of the sections with the corresponding materials. The first step at this module is to create the materials in the model's library: in this case, the materials created PLA, aluminium and a generic material so called “plate”. The plate was assigned with a Young's Modulus with 4 orders of magnitude higher than the Young's Modulus of the structures. This ensures that the deformation is entirely induced on the structure and none over the plates, as in an ideal compression test.

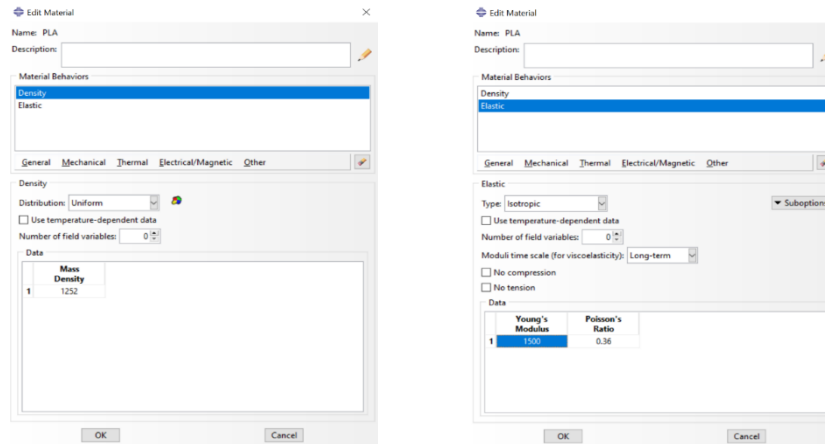


Figure 3.8 - Material properties of PLA for the elastic regime – “Property” module.

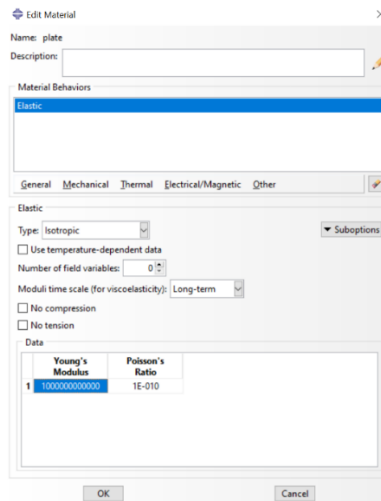


Figure 3.9 - Material properties for the compression plates – “Property” module.

The material properties for the PLA stated above are applicable to the elastic regime. For the elasto-plastic regime, it is necessary to have configured for the material both “elastic” and “plastic” properties. This way, the software will automatically assume a simulation under this regime.

For the plastic properties, multiple “stress-strain” pair points must be entered. The minimum required are two points, where the first one is the beginning of the plastic zone (yield stress, combined with null plastic strain) and the last one is the ultimate stress point, with the corresponding stress and strain.

ABAQUS makes use of true values (and not nominal) for the stress and strain, making it necessary to convert the nominal values into the true ones. The true values were introduced directly into the software, as they were already calculated in section 3.1.

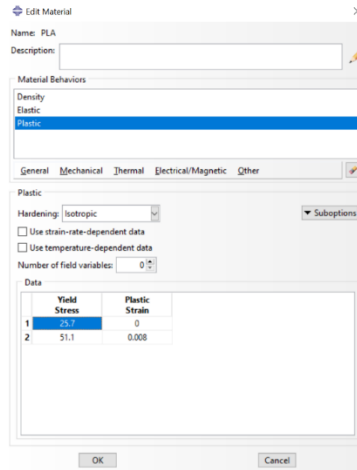


Figure 3.10 - Material properties of PLA for the elasto-plastic regime – “Property” module.

It is now necessary to create the sections and then assign them to each part. As already explained, it was created a section with PLA for the honeycomb structures and another one with this generic material with high Young’s Modulus for both plates. After the sections being created, the “assign section” command was used for attributing the sections to the parts.

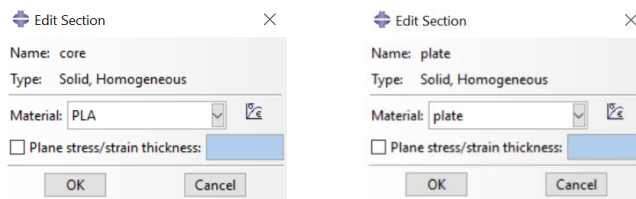


Figure 3.11 - Sections’ creation window – “Property” module.

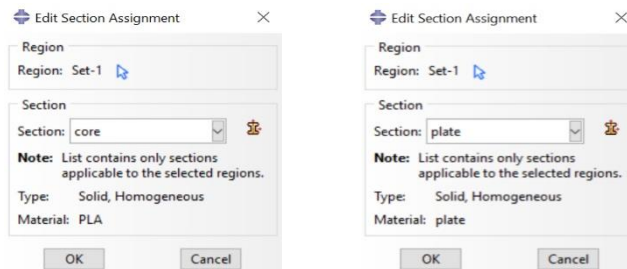


Figure 3.12 - Sections’ assignment window – “Property” module.

3.3.1.3 “Assembly” module

This module is responsible for bringing all parts to a unique assembly, reconstituting the compression test’s setup. First, it is necessary to create the instances: parts translated into entities ready to be assembled.



Figure 3.13 - “Create instance” window – “Assembly” module.

After the instances have been created, they are now in position to have geometric constraints – using the “create constraint” command – in order to assemble them according to the test’s setup. For this work, some auxiliar points were created to make both plates coincident with the structures.

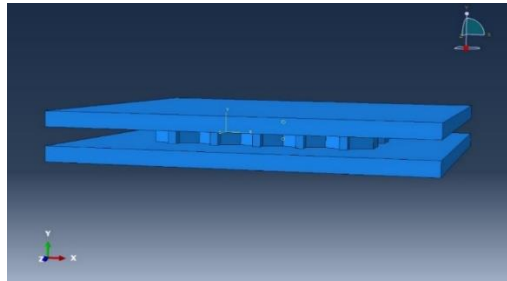


Figure 3.14 - Assembly for the compression test simulation – “Assembly module”.

3.3.1.4 “Step” module

This module is of high importance for the model solution: it is the module where a “step” is created. A “step” is a set of rules and procedures to calculate the model solution. It is possible to create multiple steps if the conditions of the problem vary with time. In this work, the conditions of the problem didn’t change throughout the whole simulation; therefore, only one step was created.

When creating a step, it is necessary to specify the type of problem. In this case, the selection must be made to “Static, General”.

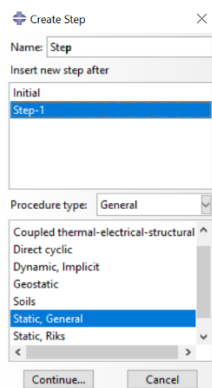


Figure 3.15 - “Create step” window – “Step” module.

After the step being created, it is now necessary to specify several parameters regarding the problem's solver. On the figures below, these parameters are discriminated for this case.

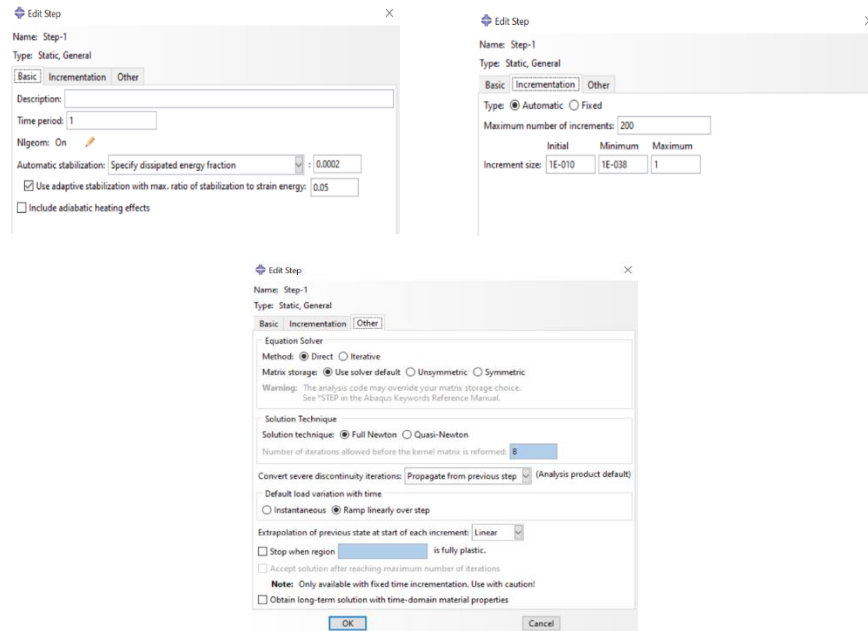


Figure 3.16 - Window for step's settings – “Step” module.

Yet in this module, it is also necessary to specify which variables and at what frequency they are needed to be recorded in the results' file. In ABAQUS, these features are denominated as the “Field Output Requests” and the “History Output Requests”. Both features write the output variables requested by the user into a results' file. While a “Field Output Request” refers to quantities distributed spatially over the whole model that can be visualized, the “History Output Request” refers to quantities at specific points or quantities which characterize the whole model or a region of the model, varying with time increments.

For this work, the field output variables requested were:

- “MISES” – von Mises equivalent stresses;
- “E” – total strain components;
- “RF” – reaction forces and moments;
- “U” – translations and rotations;

No history output variables were requested for this work.

3.3.1.5 “Interaction” module

Under this module, the interactions properties and their constraints between the different instances on the assembly are defined. This is a key module for the problem solution: different interactions or properties, even they represent the same physically, may generate different results or prevent the solution to converge.

The software allows to define different and multiple interactions under the same step or in between different steps, as well as defining some as an initial condition.

At the present case, all the interactions and their constraints were created as an initial condition and propagated into the created step.

Two interactions “Surface-to-surface” were created: one on the lower contact interface between the lower compression plate and the lower honeycomb structure’s face and another on the upper contact interface between the upper compression plate and the upper structure’s face. The software asks a “master” and a “slave” surface. For this work, the plates’ faces were defined as “masters” and the structure’s faces as the “slaves”.

Given the permanent contact of the interfaces referred above, it is necessary to define the interactions’ properties of “Contact” type, with the settings shown on figure 3.17.

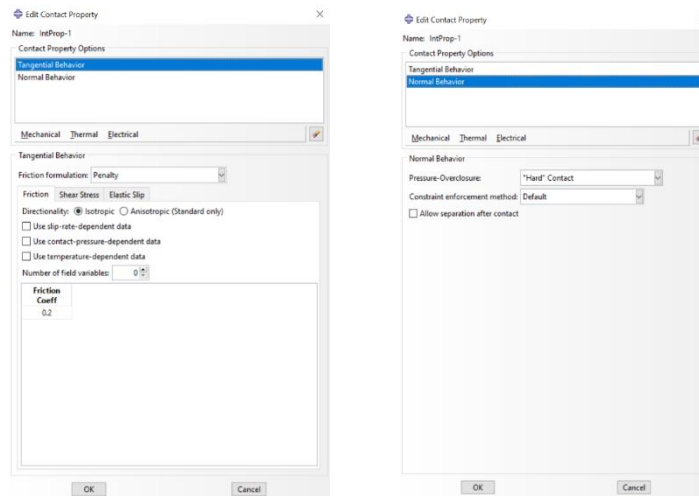


Figure 3.17 - Interaction creation and properties windows – “Interaction” module.

3.3.1.6 “Load” module

This is the module where the boundary conditions of the problem are defined. There are two parameters to be assigned at this point: the loads applied at the problem and the displacement boundary conditions themselves. As at this case there are no loads applied (forces appear as consequence of the contact between the structure and the upper plate moving downwards), only the boundary conditions will be assigned. It was necessary to define the fixation of the lower plate and the displacement of the upper plate. Therefore, three boundary conditions were created:

- Define the vertices of the lower plate’s lower face as totally constrained (neither rotational nor translational movement allowed) on the initial state – “ENCASTRE”;
- Define the vertices of the lower plate’s upper face as pinned (only rotational movement allowed) on the initial state;
- Define the displacement of the upper plate’s lower face as 0.5 mm on the negative vertical axis direction on the “step 1”.

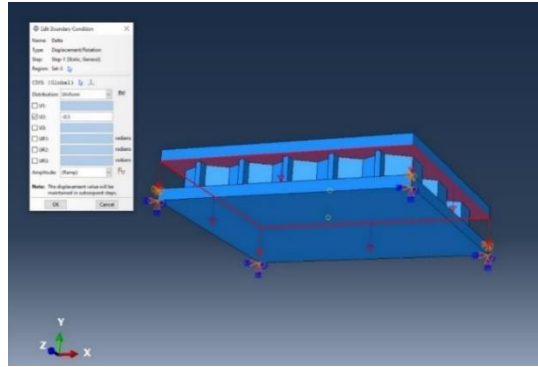


Figure 3.18 - Boundary conditions definition – “Load” module.

3.3.1.7 “Mesh” module

This is the last module before submitting the model into the solver. After all previous modules had been configured, it is now necessary to mesh all the parts of the model. In order to do so, there is a need to assign the mesh element types, to seed the part and to generate a mesh for the part.

For this work, elements of type C3D8R (3D stress, hexahedral shape of first order, reduced integration) were used.

It is very important to assign proper dimensions to the seed size and understand the concept. The seed is the first element to be created on a mesh, with an assigned size (called the “global seed size”), being the source of generation for the other elements of the mesh: the size and shape of other elements are based on the seed. As explained with more detail on the convergence analysis section ahead, the first mesh generated has an automatic seed size assigned, and it’s tuned subsequently when performing a mesh refinement.

Lastly, the mesh is applied to the part clicking on the “mesh part” command.

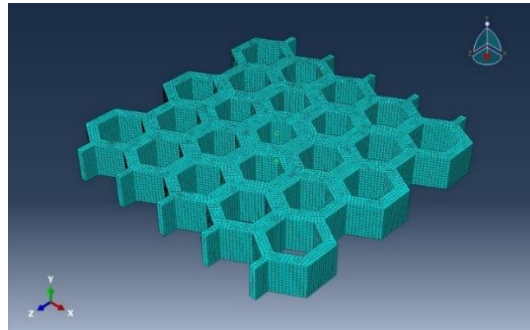
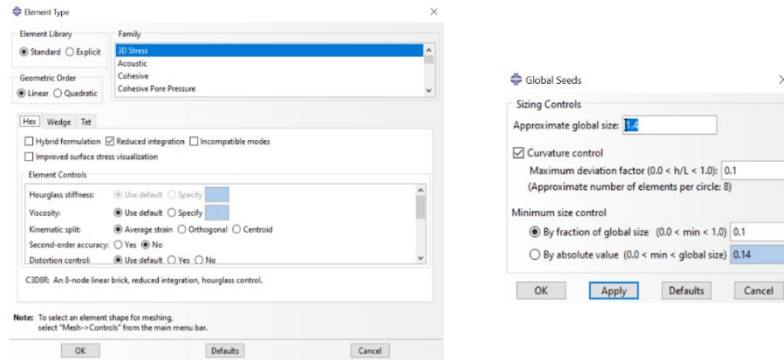


Figure 3.19 - Element types/seed control windows and mesh applied to the structure – “Mesh” module.

3.3.1.8 “Job” module

This is the last module on the model making procedure. It is where a “job” is configured to solve the problem, clicking on the command “create job”. A “job” is the programming of the model’s simulation run. For this work, all the job configurations were left to standard. After the job is created, it is necessary to submit it under the “job manager” tab.

It is possible to run a “data check”, where the software runs an analysis to the modelling in order to detect any committed errors or incongruences.

Once the job is submitted, it is possible to open the “monitor” window, where the solver data is displayed as the simulation is running.

3.3.1.9 “Visualization” module

Under this module, it is possible to visualize the requested variables over the model, as well as process them and export it to other platforms. In order to do so, it is necessary to click on the command “plot contours on deformed shape”, where any incrementation’s step of the simulation can be selected. It is also possible to select different “display groups” to view the results for some parts instead of the whole model.

For this work, three variables were processed under the software for the intended results: the von Mises stresses (“MISES”), the reaction force in the vertical axis (“RF2”) and the displacement on the same axis (“U2”).

Regarding the von Mises stress, a display group with the structure only was created, so that the only read values would be the ones from the structure, as well the stress distribution would be more perceptible. From the scale legend, the von Mises maximum stress is directly taken.

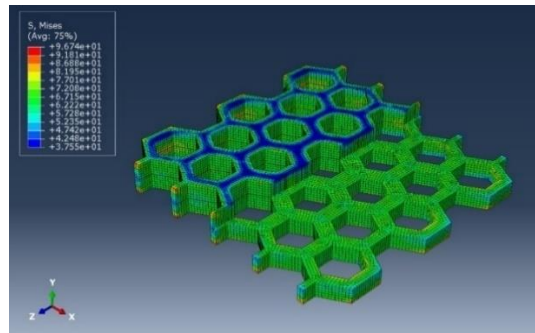


Figure 3.20 - Viewport for von Mises stress over the structure – “Visualization” module.

In order to obtain forces vs. displacement curves and stress-strain for all the simulated structures, it is necessary to process the variables “RF2” and “U2”. To do so, it is necessary to understand that:

- The displacement is set by the upper plate’s movement, therefore the variable “U2” must be evaluated at this part. As the plate’s Young’s Modulus is set as a very high value, the plate will behave as a rigid body: this is, all the part’s nodes must have the same displacement;
- The force is a reaction of the upper contact between the compression plate and the structure, and it must be a sum of all nodes in this contact; in other words, the force is the result of the sum of the “RF2” value in all nodes of the upper plate’s lower face and the structure’s upper face.

For the variable “U2”, it was requested an “ODB field output” using the command “create XY data”. A dialogue window is opened and, under the “Variables” tab, the “U2” variable must be selected with the “position” set to “unique nodal”. Next, under the “Elements/Nodes” tab, the selection method must be set to “Pick from viewport” and then select any node on the upper plate. The software is now in conditions to draw the plot. The user needs to save the plot, since the software only keeps temporary plots.

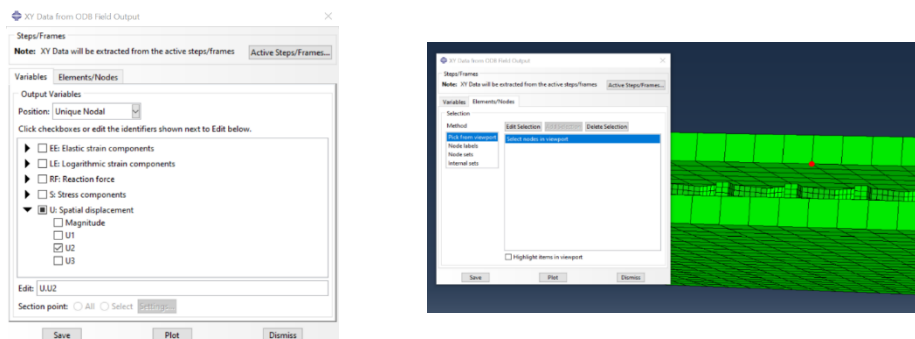


Figure 3.21 - “U2” field output procedure – “Visualization” mode.

For the variable “RF2”, similarly to the “U2” variable, it is necessary to request an “ODB field output” as “unique nodal”. Under the “Elements/Nodes” tab, the method can now be set to “Internal sets” and select both the structure’s upper face and the upper plate’s lower face, simultaneously.

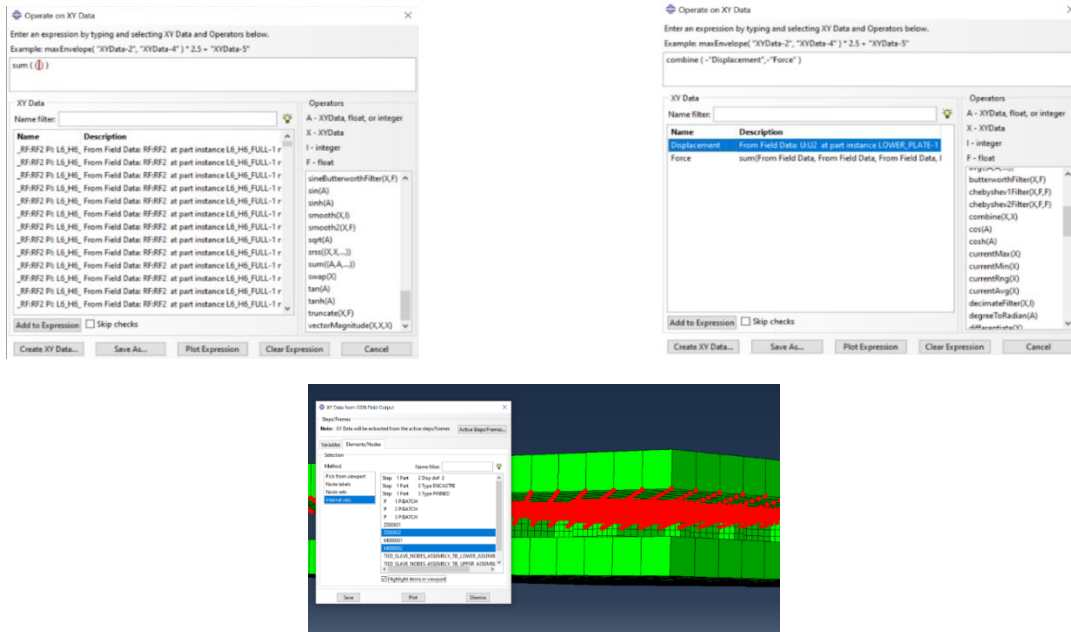


Figure 3.22 - “RF2” field output procedure – “Visualization” module.

Given the multiple plots due to the request for several nodes, it is now necessary to sum all the plots to have the real reaction force value. For this, it is necessary to use the command “operate on XY data”, using the operation “sum” with all the nodes selected. This will generate a single plot with the intended force value.

To finalize the results obtaining process, both variables (“U2” and “RF2”) need to be gathered. For this, the user should make use of the command “operate on XY data”, now using the operation “combine (X,X)” where the “X” must be replaced by “U2” and “RF2”. respectively. At the present case, a minus signal was added to the variables on the expression to make positive the values (negative by standard due to the plate’s displacement in the contrary direction to the positive axis’ direction).

The final plot can be exported to an Excel file with the force and displacement values for each time increment.

3.3.2 Mesh Refinement

At the FEM software, the main control parameter for the mesh is the “global seed size”, which is a multiplication factor with reference to the size of the seed element (the first generated mesh element on the model). This way, the mesh refinement was done based on the global seed size. The first size is suggested by the software.

The convergence analysis was made based on the evaluation of the average von Mises stress at three specific nodes, with the respective deviation being calculated according to the equation 3.5:

$$Error [\%] = \frac{|\bar{\sigma}_{VM_i} - \bar{\sigma}_{VM_{i-1}}|}{\bar{\sigma}_{VM_{i-1}}} * 100 \quad 3.5$$

The meshes parameters and their simulation time for the full-geometry model are presented on table 3.7.

Table 3.7 - Parameters and simulation time for various meshes (full model).

	Global seed size [mm]	Number of nodes	Number of elements	Simulation time [s]
Full model	1.4	26662	13880	282
	1.2	29926	15671	444
	1.1	31630	16646	359
	1.0	51111	28212	637
	0.95	50969	28212	567

The figure 3.23 shows convergence analysis of the full model for three different nodes.

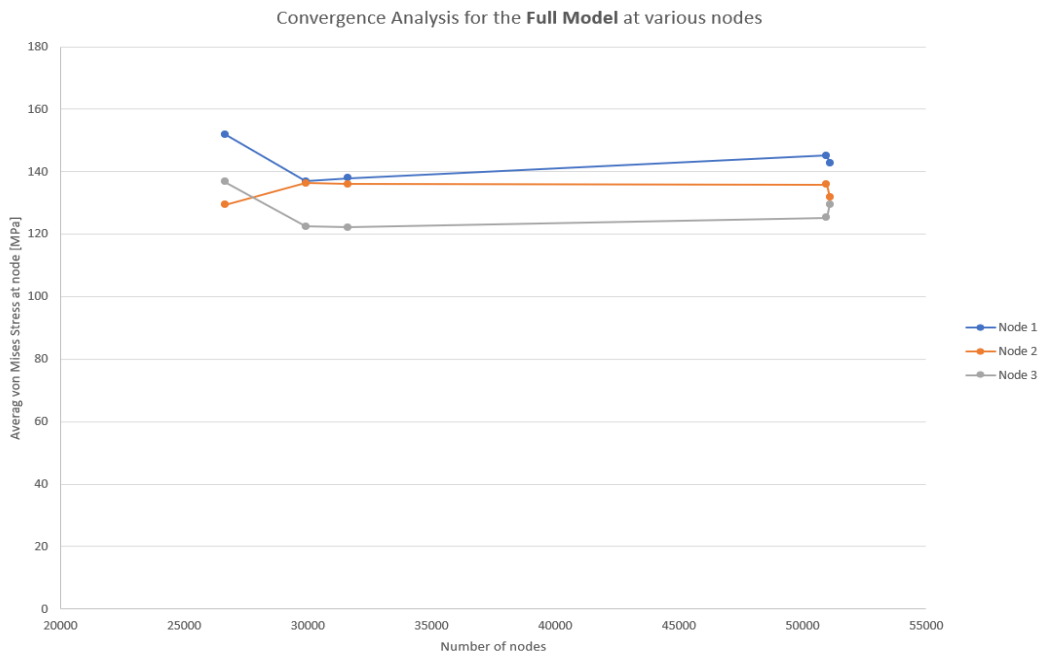


Figure 3.23 - Convergence analysis for the full model at various nodes.

Given the convergence analysis, the mesh chosen for the numerical analysis was the one with global seed size of 1.0 mm, due to the good convergence of the average von Mises stress as shown in the figure above.

3.4 Specimens 3D-printing

3.4.1 PLA samples

For the experimental tests, PLA specimens were 3D-printed using Fused Filament Fabrication (FFF), at Laboratório de Desenvolvimento de Produto – Departamento de Engenharia Mecânica, Instituto Superior

Técnico. Three specimens of each geometry were printed in order to evaluate error statistics, ensuring the results validity on the experimental tests.

The equipment used to produce the PLA specimens was Ultimaker 3, using the software *Ultimaker Cura*.

Regarding to the preparation for the printer's input, there were alterations to the coded information inside the model files. It was necessary to export the CAD 3D models as a “.3mf” (“3D Manufacturing Format”) file under *Solidworks*. Once exported, the file was uploaded into *Ultimaker Cura*. Under *Cura*, it was necessary to position the model centred on the build platform and to lay it flat. The next step was to connect the printer to the software, as well as to set the printing parameters of the process.

Regarding the printing parameters, the following were set:

- Layer thickness: 0.2 mm;
- Infill density: 100%;
- Printing temperature (material's temperature at the extruder nozzle): 210 °C;
- Build platform temperature: 60 °C;
- Printing speed: 80 mm/s.

Figure 3.24 shows the equipment used for printing and *Ultimaker Cura* software.



Figure 3.24 - (a) Ultimaker 3 printer; (b) Ultimaker Cura software interface.

Once the parameters were configured, the software was ordered to “slice” the model. “Slicing” is a software’s operation to build the printing tool’s path as well as the printing layers, transforming then the 3D model information into G-code (a code language that translates the tool’s path information into instructions for the machine), creating a new file. After the slicing operation, the model is now ready for printing.

3.4.2 Aluminium samples

The aluminium samples were produced using the SLM fabrication process, with the same process parameters and equipment as in Miranda’s work [14]. The specimens were produced in École Nationale Supérieure des Mines d’Albi-Carmaux, at Institut Clément Ader. SLM Solutions 125HL was the equipment used for the process, having a 400 W laser beam with diameter varying between 70 μ_m and 100 μ_m , and a

maximum speed of 10 m/s. According to the materials data sheet, the samples were produced with a layer thickness of 50 μ_m .

3.5 Experimental Test

In this section, the experimental tests procedure is detailed. Various specimens (PLA and Aluminium) were submitted to a compression test, according to the ASTM C365-94 [42] standard. The tests were performed at Laboratório de Mecânica Experimental – Departamento de Engenharia Mecânica, Instituto Superior Técnico, and the equipment used at the was an Instron 3369, with a load cell of 50 kN (visible on figure 3.25). The test setup consisted of two compression plates, being the upper plate attached to the load cell, while the lower plate is fixed. Test data was acquired through the software *Instron Bluehill* (figure 3.26).

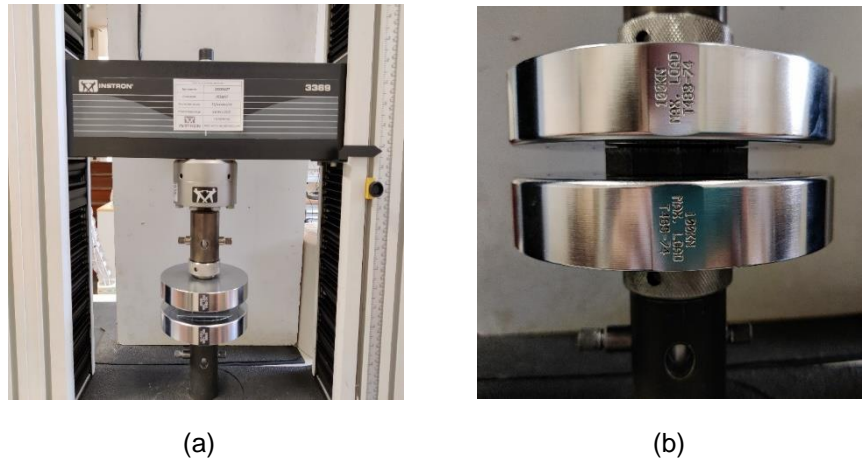


Figure 3.25 - (a) Instron 3369; (b) load cell installed on the test equipment.

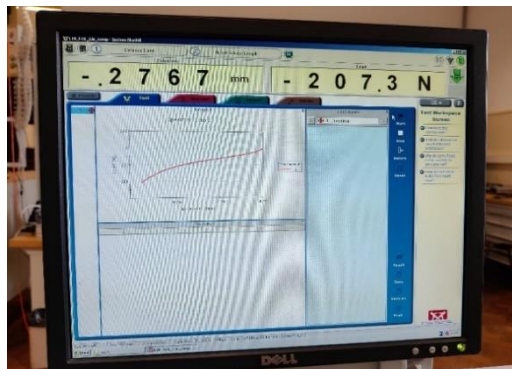


Figure 3.26 - View of Instron Bluehill software for data acquisition.

Different tests were performed regarding the material's mechanical regime. For PLA samples, the tests were performed under elasto-plastic regime until failure. For the aluminium samples, the test was performed with an imposed displacement of 0.5 mm. All the tests were performed at a constant speed of 0.5 mm/min.

Not all 3D modelled geometries were submitted to test. Therefore, table 3.8 details which of the geometries were experimentally tested. It is important to clarify that in order to ensure the validity of results, there were

three specimens for “h12” geometry types of PLA and three specimens for “h10” geometry types of aluminium.

Table 3.8 - List of geometries tested experimentally.

Material	Geometry type [L – cell length; h – core height]	General dimensions [mm x mm]
Aluminium	Regular L6 – h6, h10, h12	65.81 x 66
	Regular L8 – h6, h10, h12	83.15 x 84
	Regular L10 – h6, h10, h12	61.20 x 68
PLA	Regular L4 – h12	66.99 x 64
	Regular L6 – h12	91.15 x 88
	Regular L8 – h12	83.15 x 84
	Regular L10 – h12	100.46 x 102
	Graded, “T6-8-10” – h12	91.59 x 91.35
	Graded, “S0.5+_20”	100.46 x 102
	Graded, “S0.5-_20”	100.46 x 102
	Graded, R1 = + 0.31	88.51 x 90
	Graded, R1 = - 0.31	88.51 x 90

Chapter 4: Results and Discussion

4.1 Preliminary Notes

It is important to refer some aspects regarding the methodology and the physical aspects of the specimens used on this work.

Firstly, it must be referred that, for the Finite Element analysis, two models were elaborated: one with the entire structure (“full model”) and another with a quarter of the original structure, according to its symmetry planes (“quarter model”). The quarter model (described on appendix A – “Use of Symmetry”) was not used to analyse the structures, being the full model the one used during all numerical analysis. Although mesh studies showed a good correspondence between both models and savings in computation time, it was decided to use the full model for the FEA.

Regarding the specimens production, it shall be noted that:

- On aluminium specimens, a large porosity was noted inside the cell walls, which could eventually lead to structures with different densities rather than the expected. This may lead to non-relatable experimental values on the studied variables, in comparison to the numerical values. In addition to this, some imperfections at the ends of the structures were also noted;
- The filament roll was changed in between the production of the PLA structures. Although the used material has no difference between rolls, this may result in values discrepancies over the studied variables;
- Yet in some PLA specimens, there were noticed some infill gaps. This happens due to the wall thickness not matching with the extruder nozzle diameter or multiples of it. Although this has been discussed prior to the specimens printing, it wasn’t possible to match every wall thickness values with the extruder nozzle diameter or its multiples. Hence, it may induce some less conservative results when evaluating the performance of the 3D-printed structures.

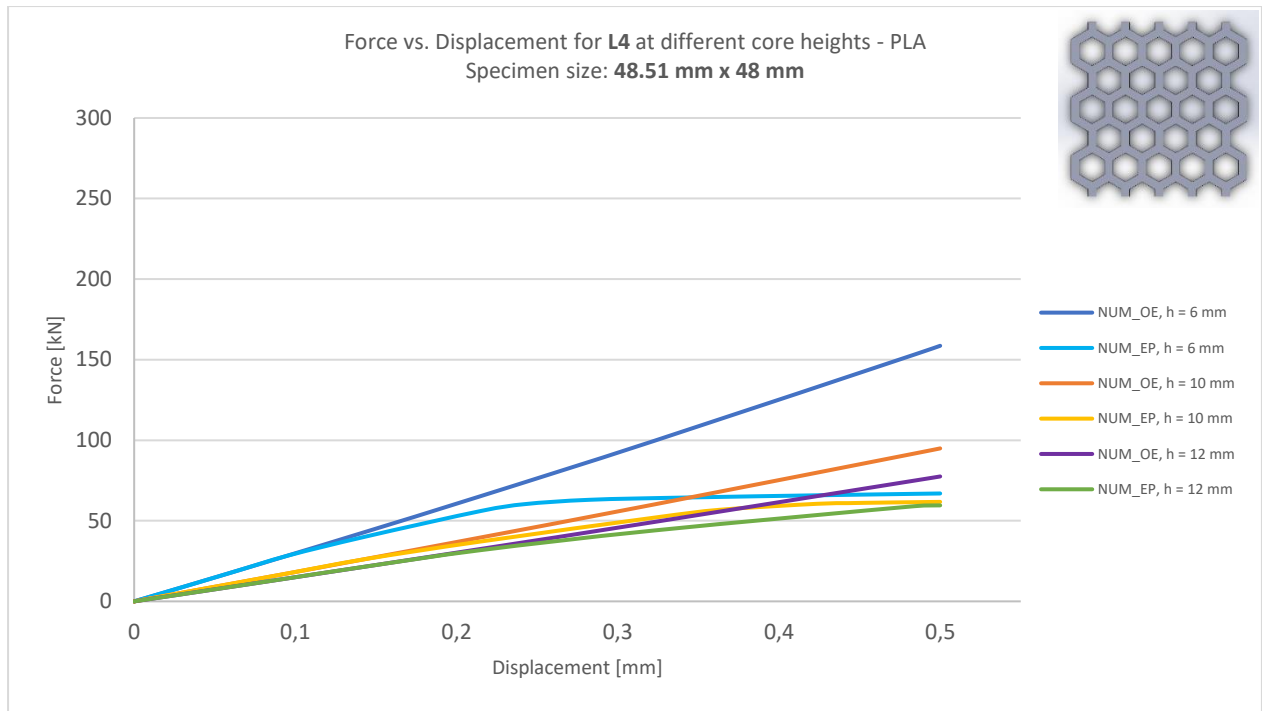
4.2 Force vs. Displacement Curves

Each model had its force vs. displacement curve taken for further processing, as will be described in section 4.3. In this section, the results are shown for PLA and aluminium specimens, for regular and graded structures. The elasto-plastic mechanical regime simulation and testing were only executed for PLA regular structures. All the other models were executed under only-elastic mechanical regime conditions.

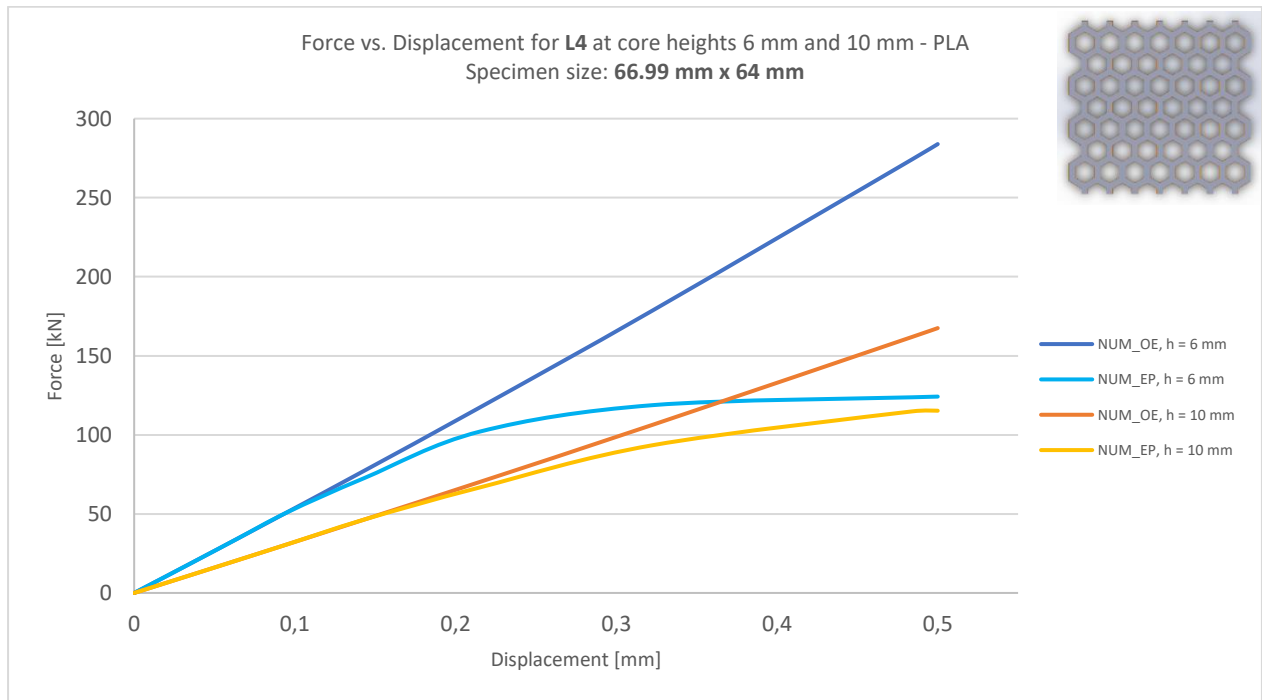
4.2.1 PLA

4.2.1.1 Regular structures

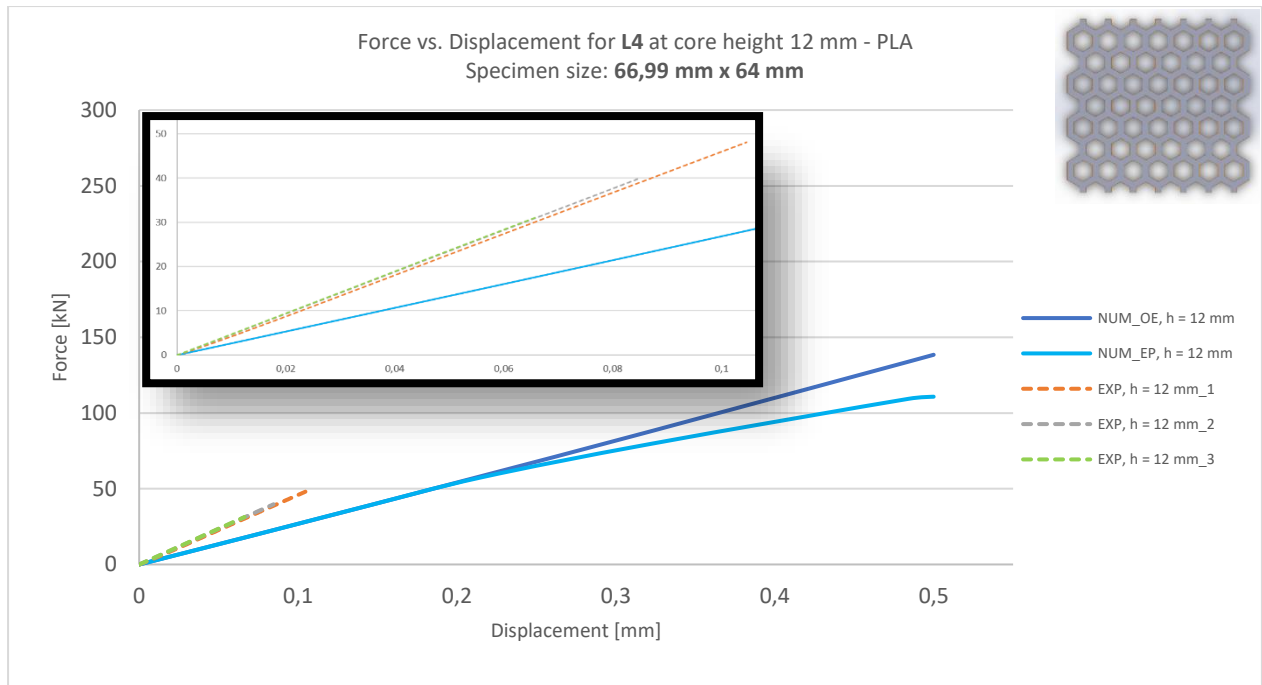
The results obtained for PLA regular structures are presented in figure 4.1. For each geometry, there are two plots: one for only numerically analysed structures (core heights equal to 6 mm and 10 mm, both submitted to only-elastic – “NUM_OE” – and elasto-plastic – “NUM_EP” – simulations) and another for core height equal to 12 mm, subjected to both FEA (“NUM”) and experimental testing (“EXP”).



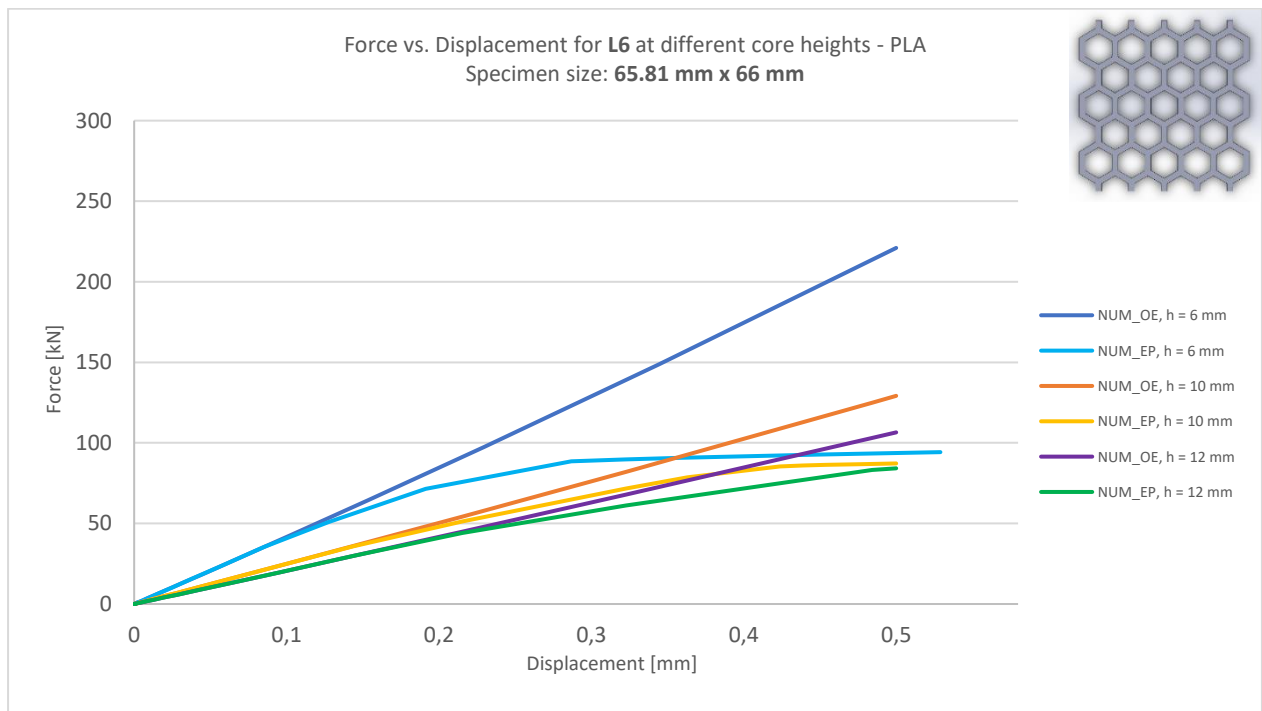
(a)



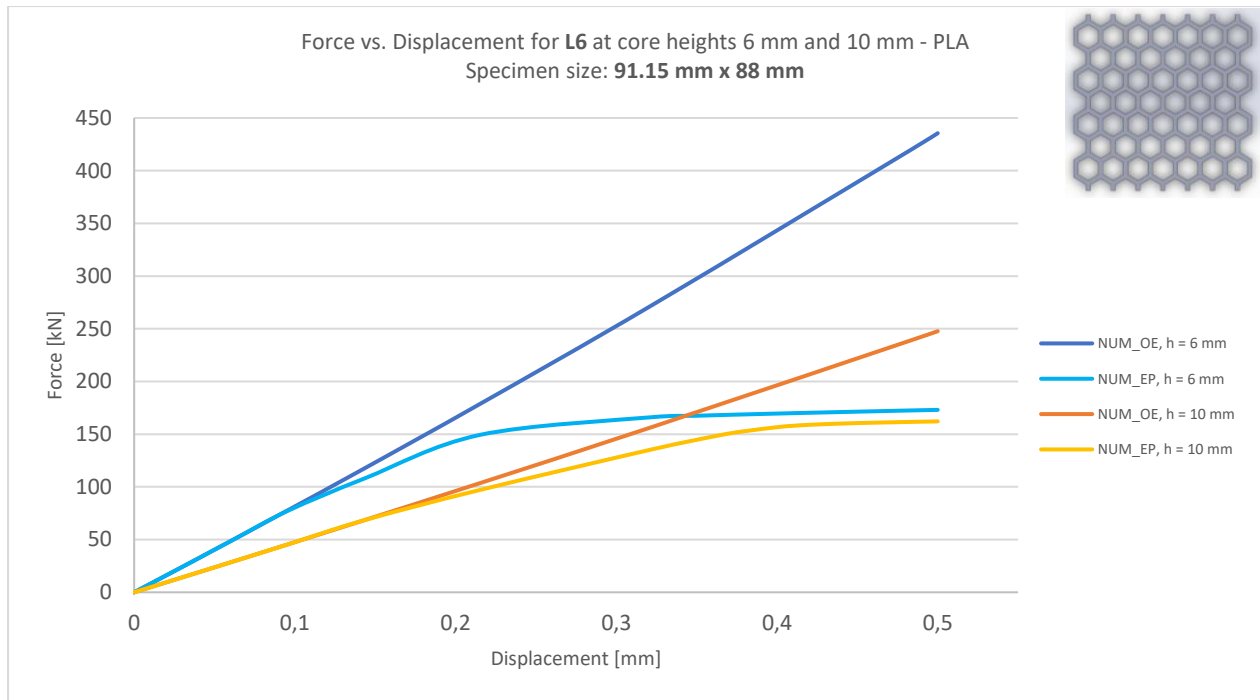
(b)



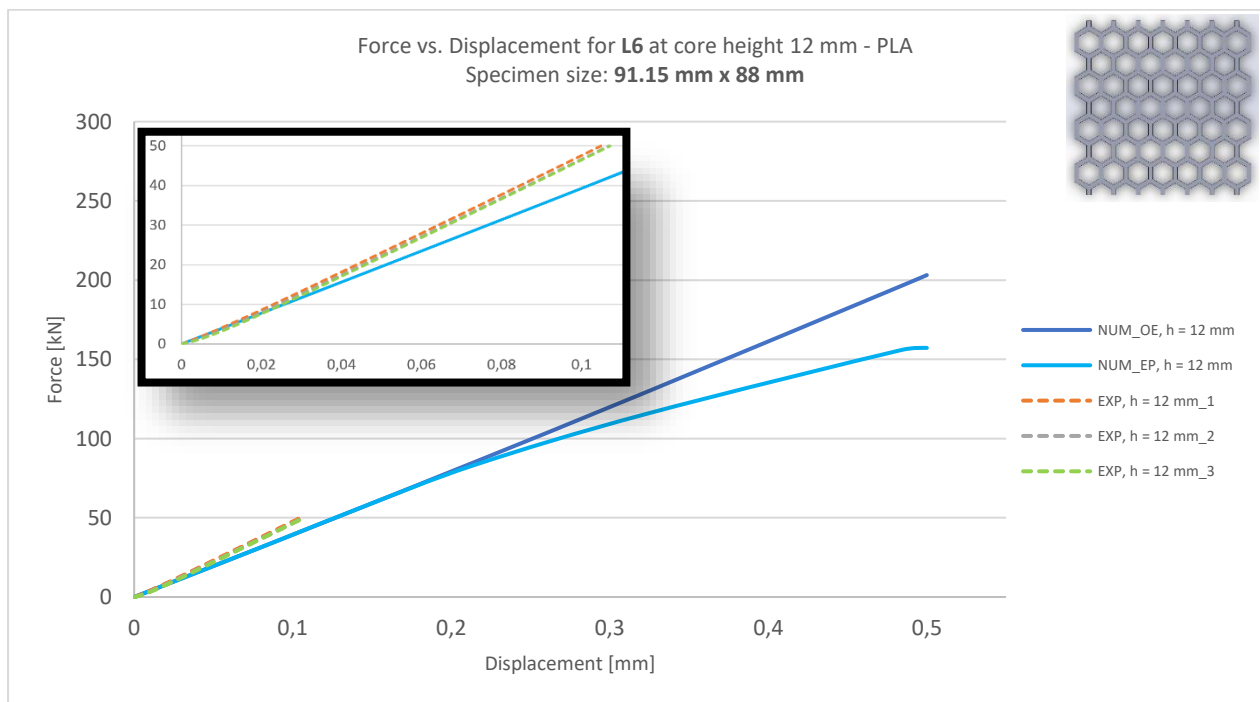
(c)



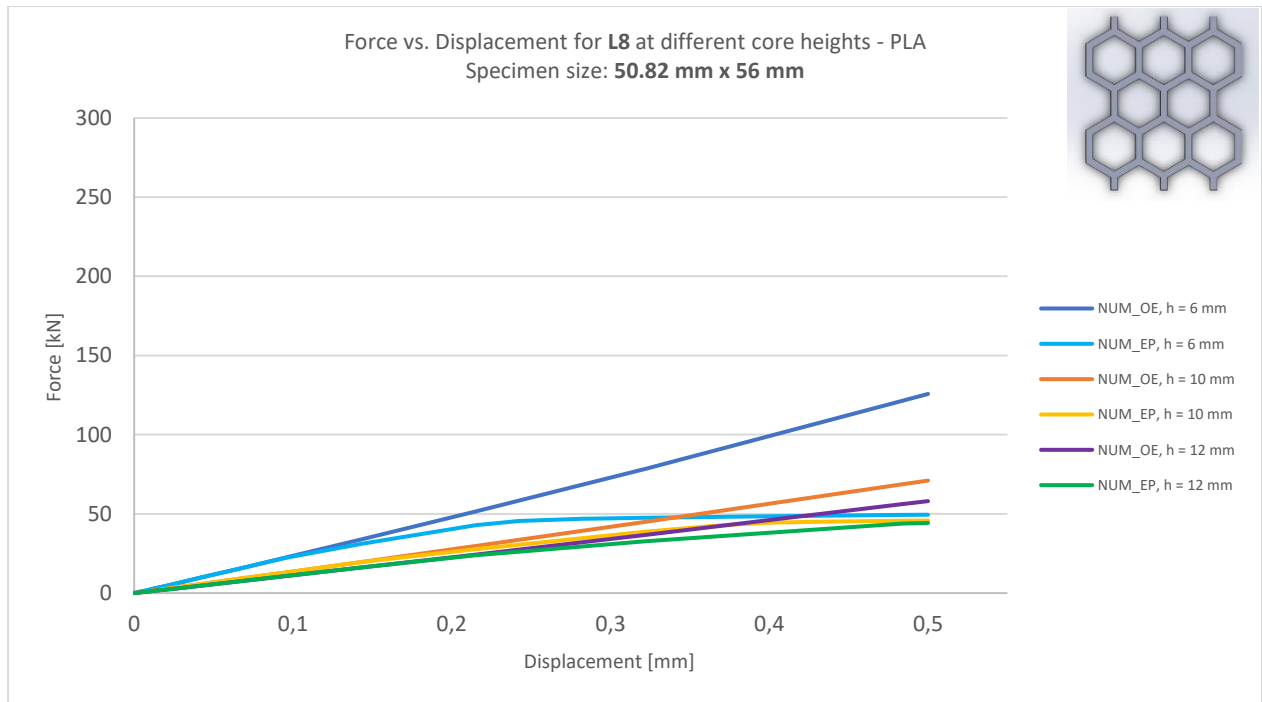
(d)



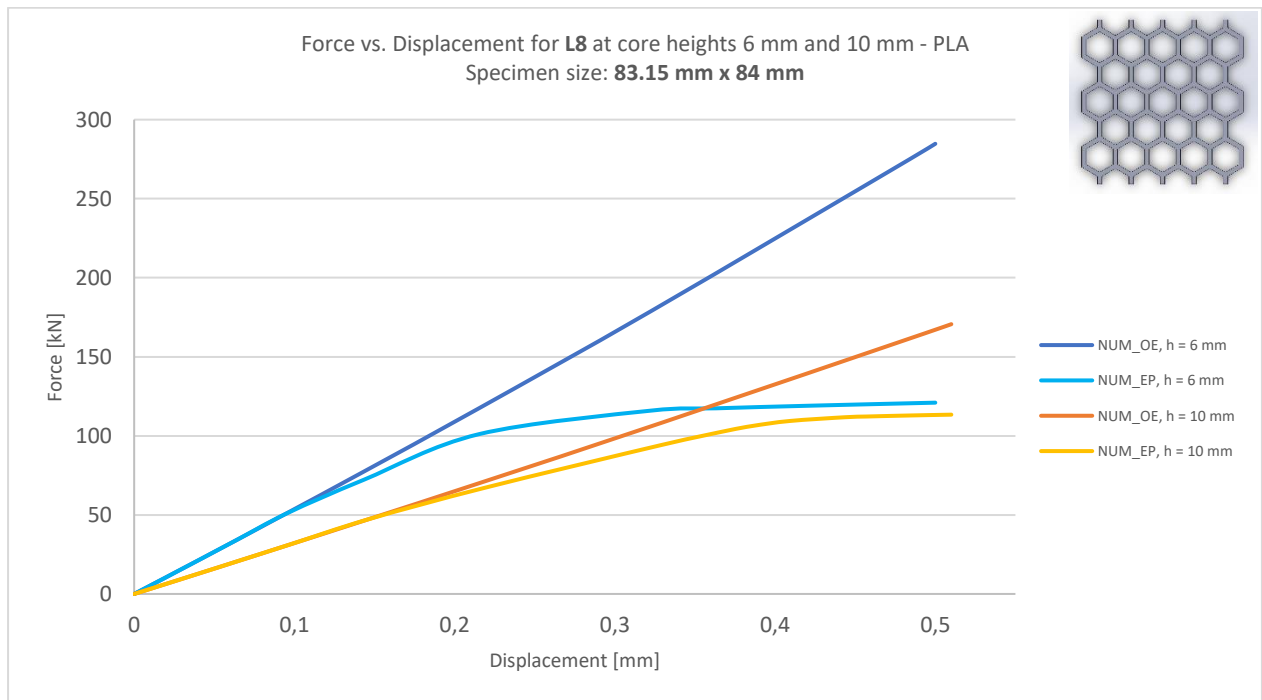
(e)



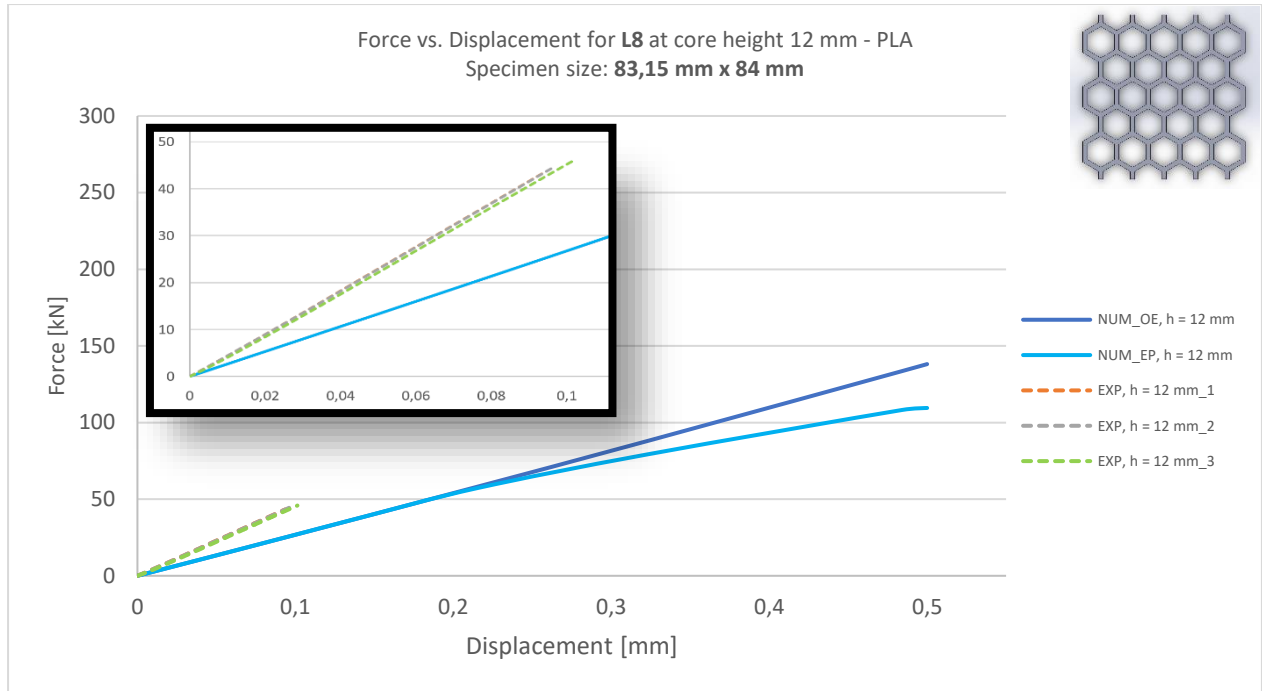
(f)



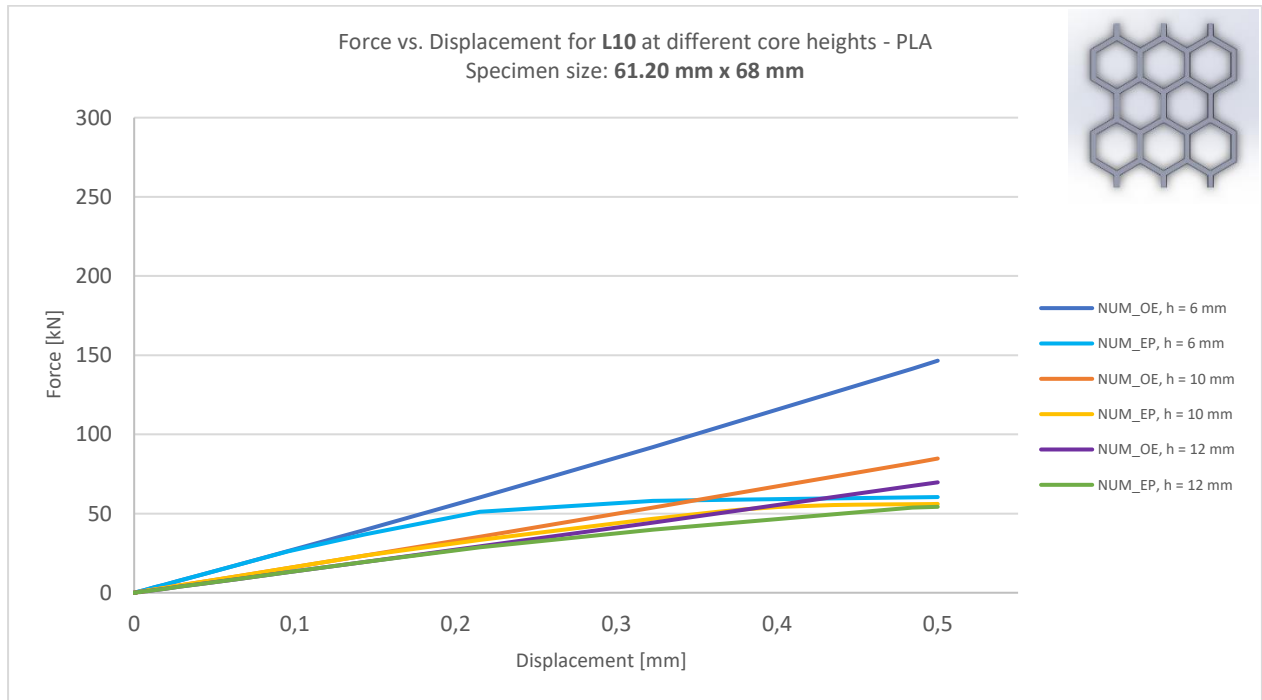
(g)



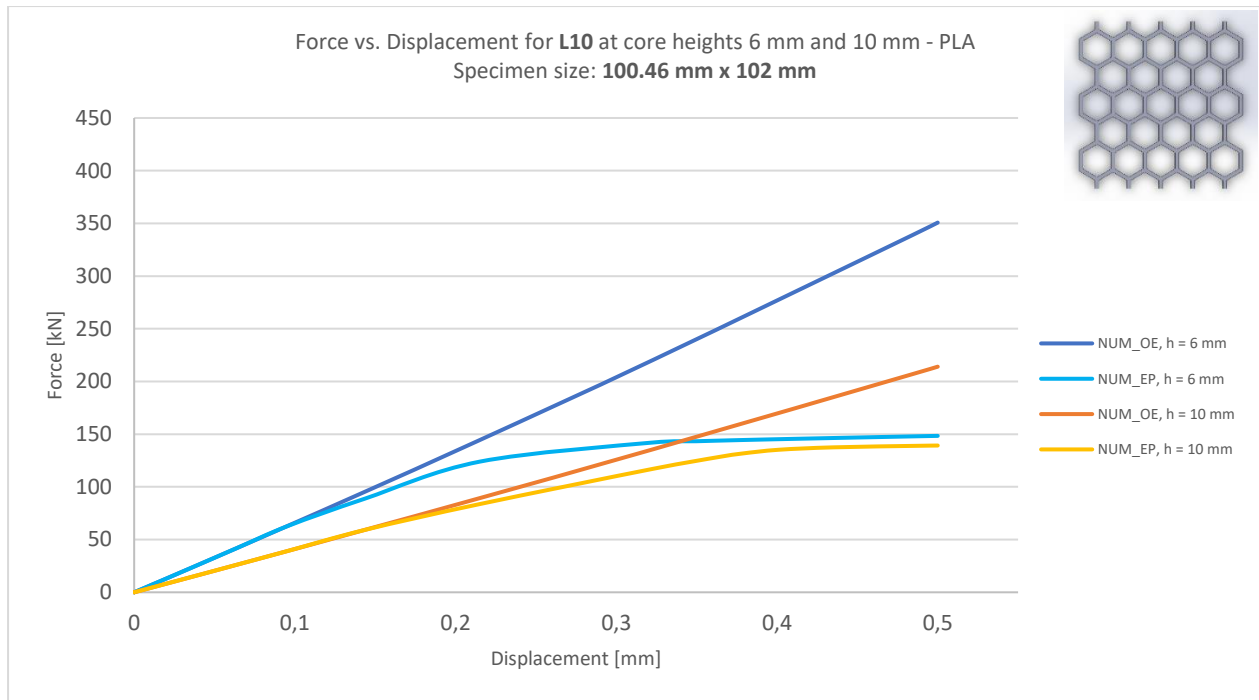
(h)



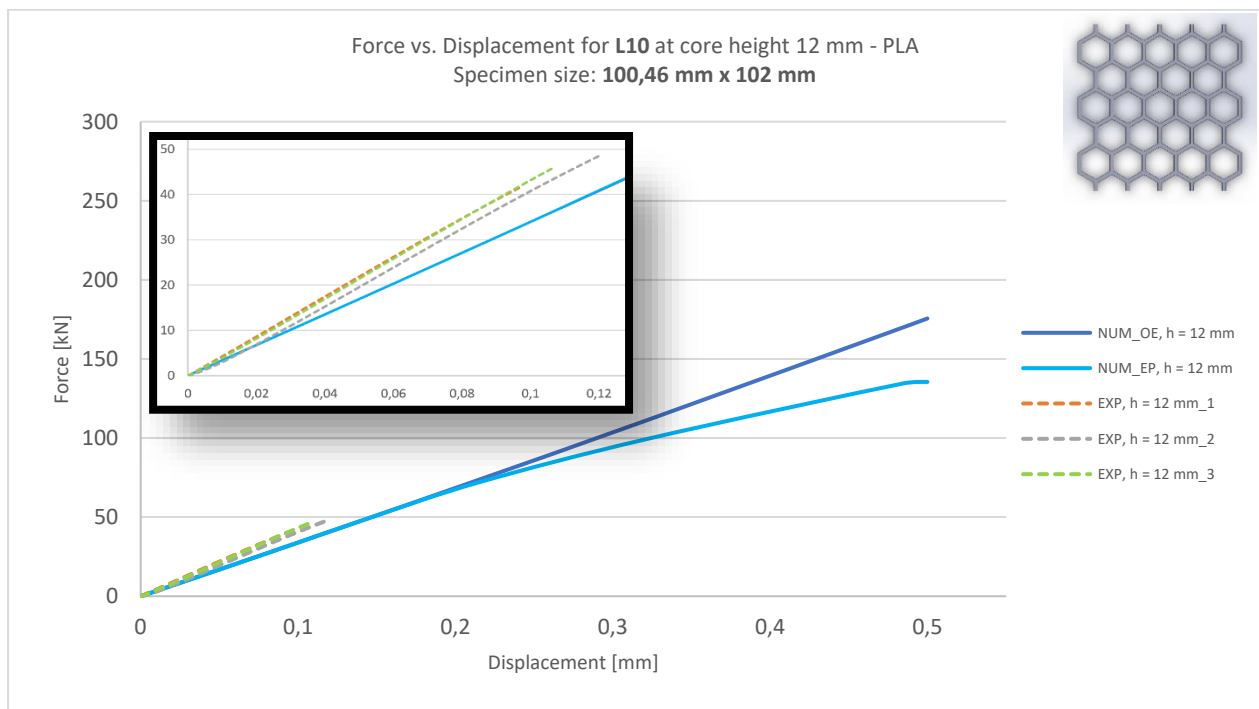
(i)



(j)



(k)



(l)

Figure 4.1 - Force vs. Displacement curves for aluminium regular structures with different specimen size:
(a) (b) (c) L4; (d) (e) (f) L6; (g) (h) (i) L8; (j) (k) (l) L10.

4.2.1.2 Graded structures

The results obtained for PLA graded structures – designed by the three methods stated in section 3.2 – are presented below. Each plot contains the numerical (“NUM”) and experimental (“EXP”) results for the same case, studied at constant core height of 12 mm.

Figure 4.2 shows the numerical results for the two geometrical configurations of the first design method and the corresponding experimental results for only one case (“T6-8-10”).

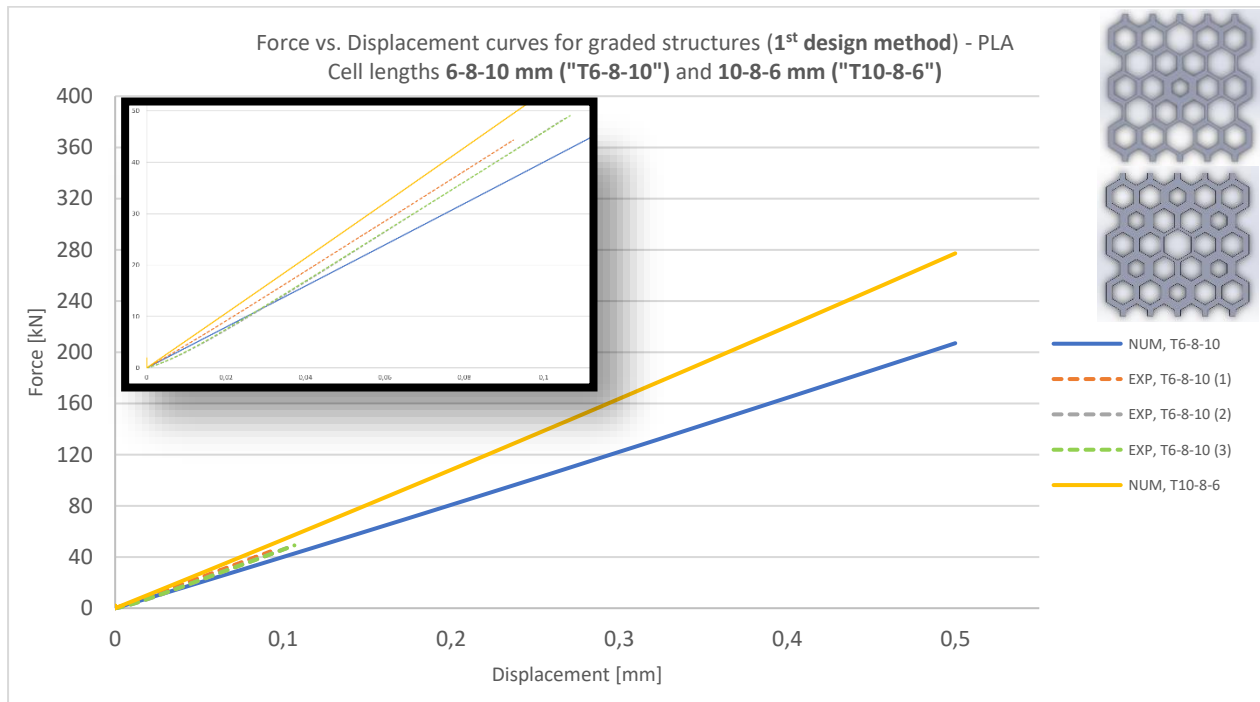
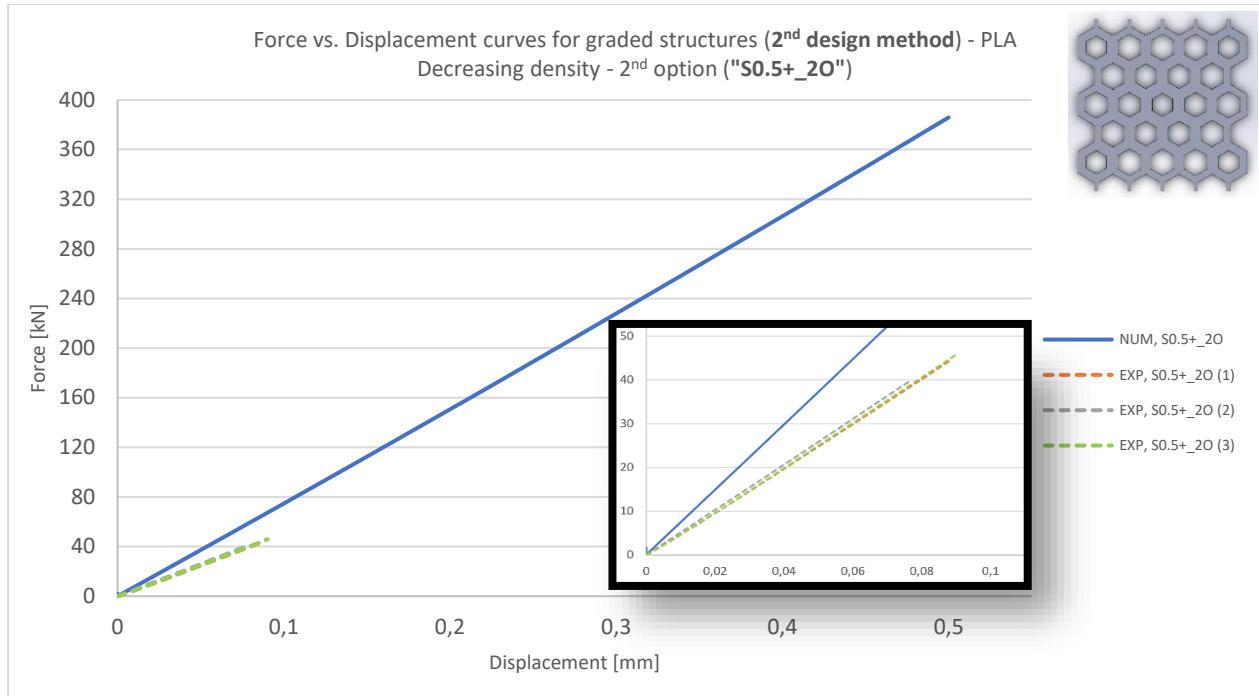
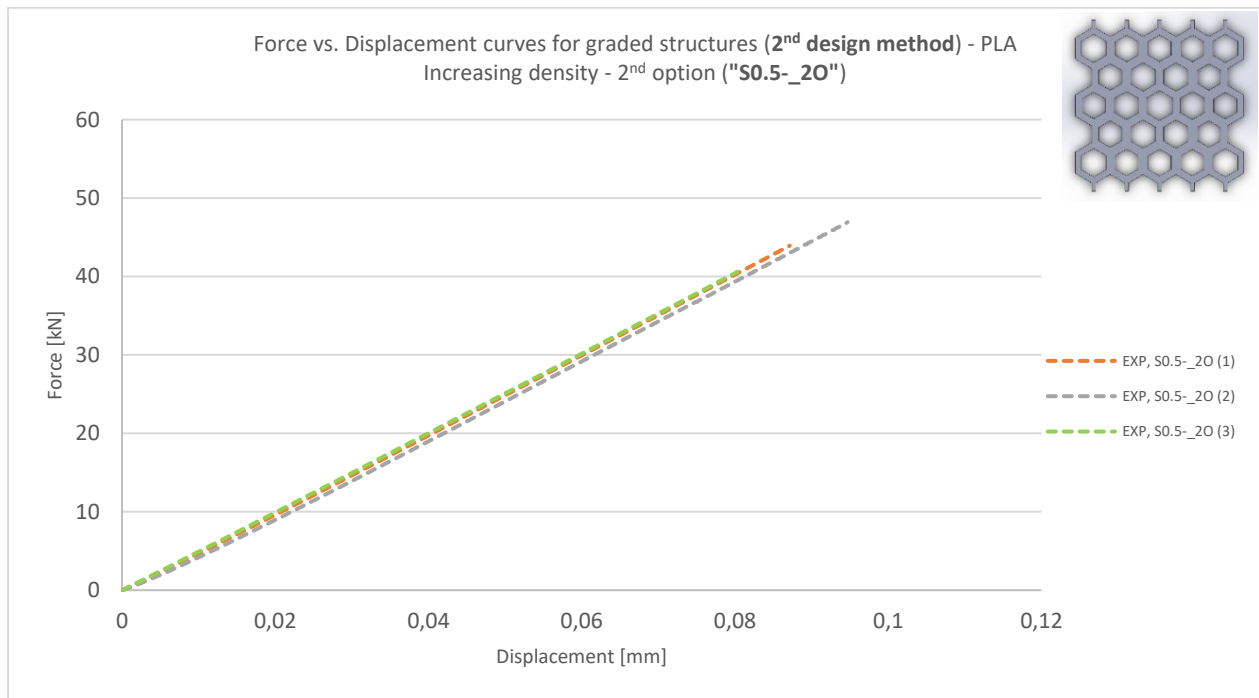


Figure 4.2 - Force vs. Displacement for PLA graded structures (first design method).

Figure 4.3 shows the experimental results for two of second design method's geometries and the numerical for only one case ("S0.5+_20"), present on first plot [4.3 (a)].



(a)



(b)

Figure 4.3 - Force vs. Displacement for PLA graded structures (second design method): (a) Decreasing density; (b) Increasing density.

Figure 4.4 translates the results obtained for the second design method's cases that were only submitted to numerical analysis.

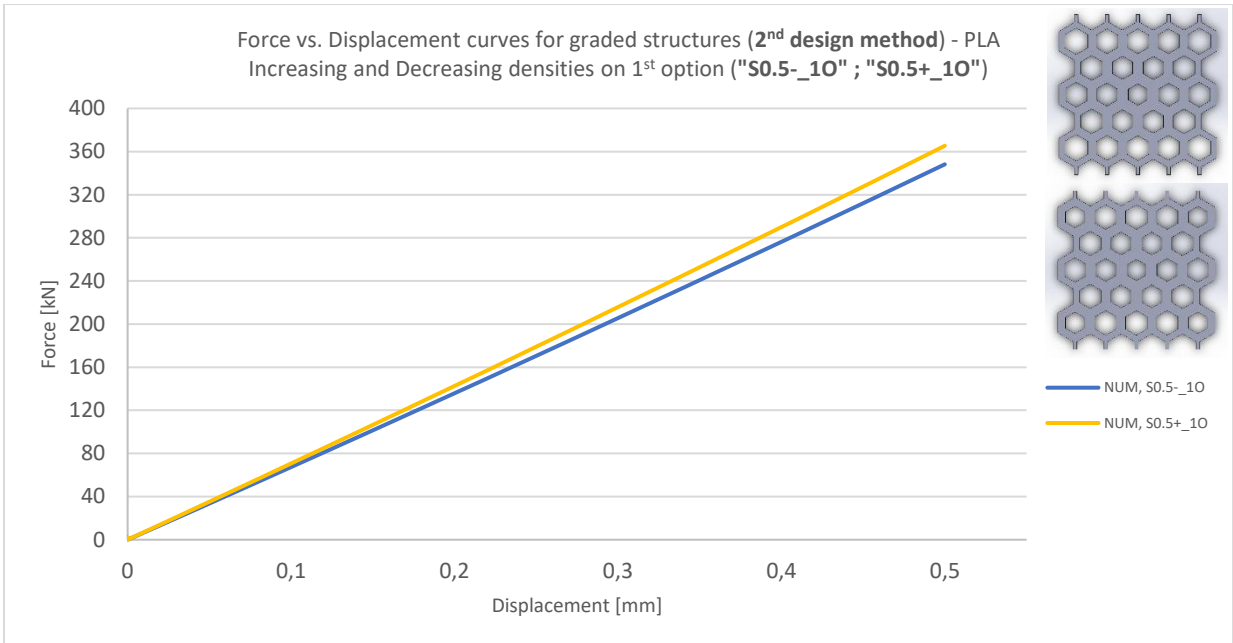
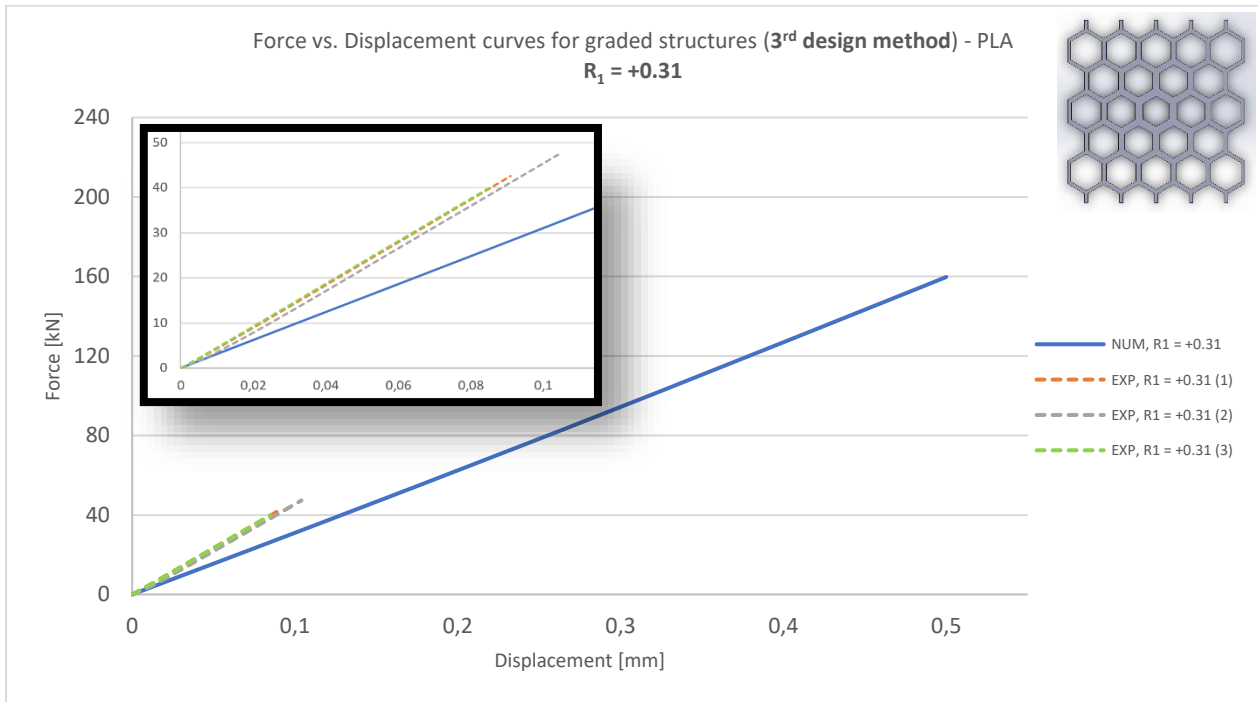
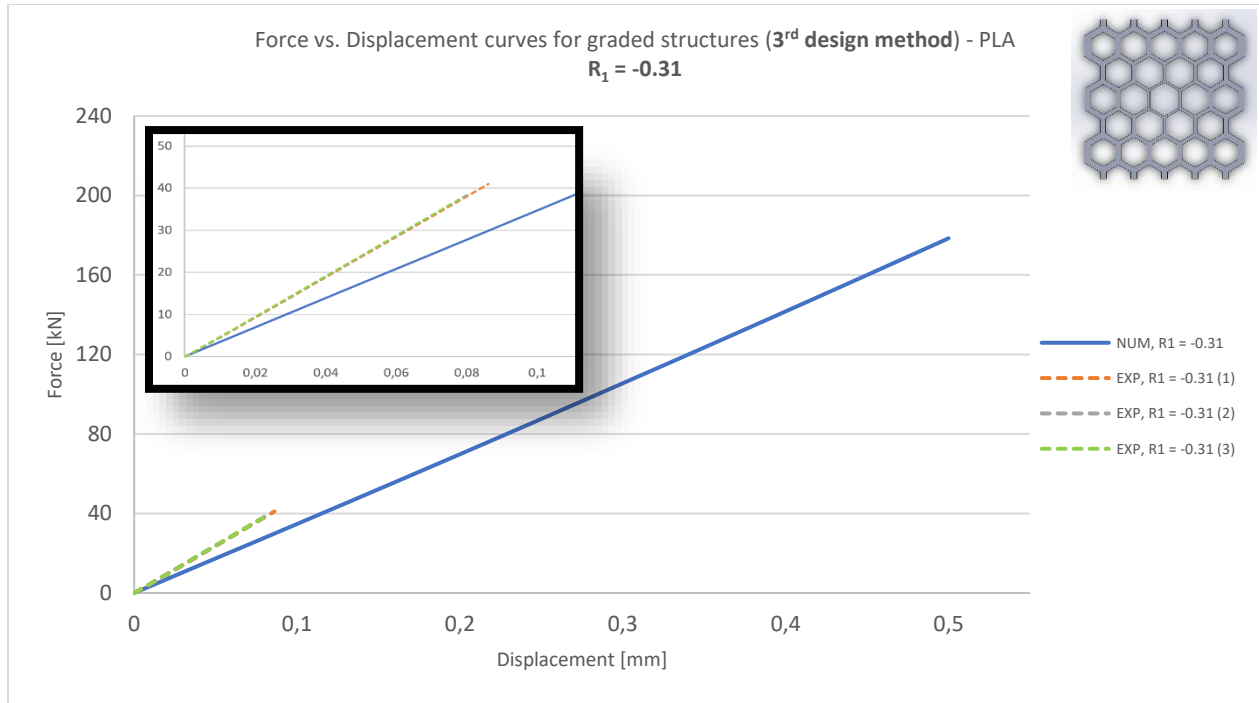


Figure 4.4 - Force vs. Displacement for PLA graded structures (second design method): increasing and decreasing densities on first option.

Figure 4.5 shows the numerical and experimental results for two of the third design method's geometries: $R_1 = +0,31$ [4.5 (a)] and $R_1 = -0,31$ [4.5 (b)].



(a)



(b)

Figure 4.5 - Force vs. Displacement for PLA graded structures (third design method): (a) $R_1 = +0,31$; (b) $R_1 = -0,31$.

Figure 4.6 shows the other cases of the third design method that were only submitted to numerical analysis.

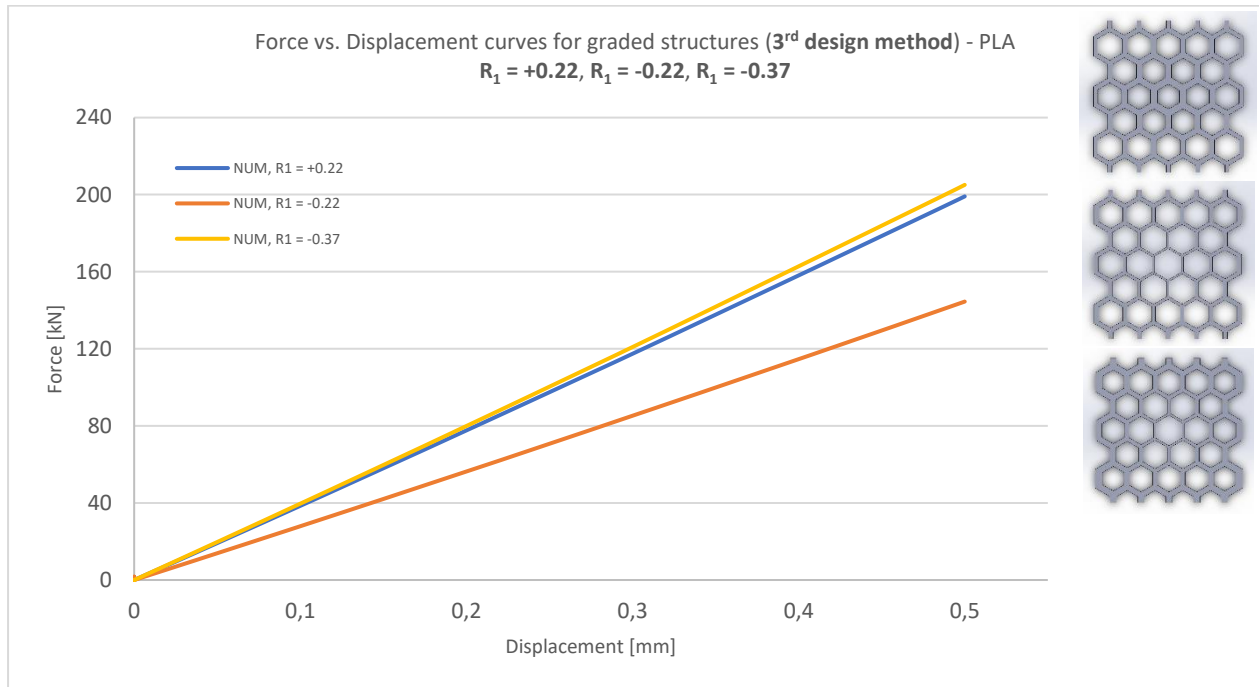


Figure 4.6 - Force vs. Displacement for PLA graded structures (third design method): $R_1 = +0.22$, $R_1 = -0.22$, $R_1 = -0.37$.

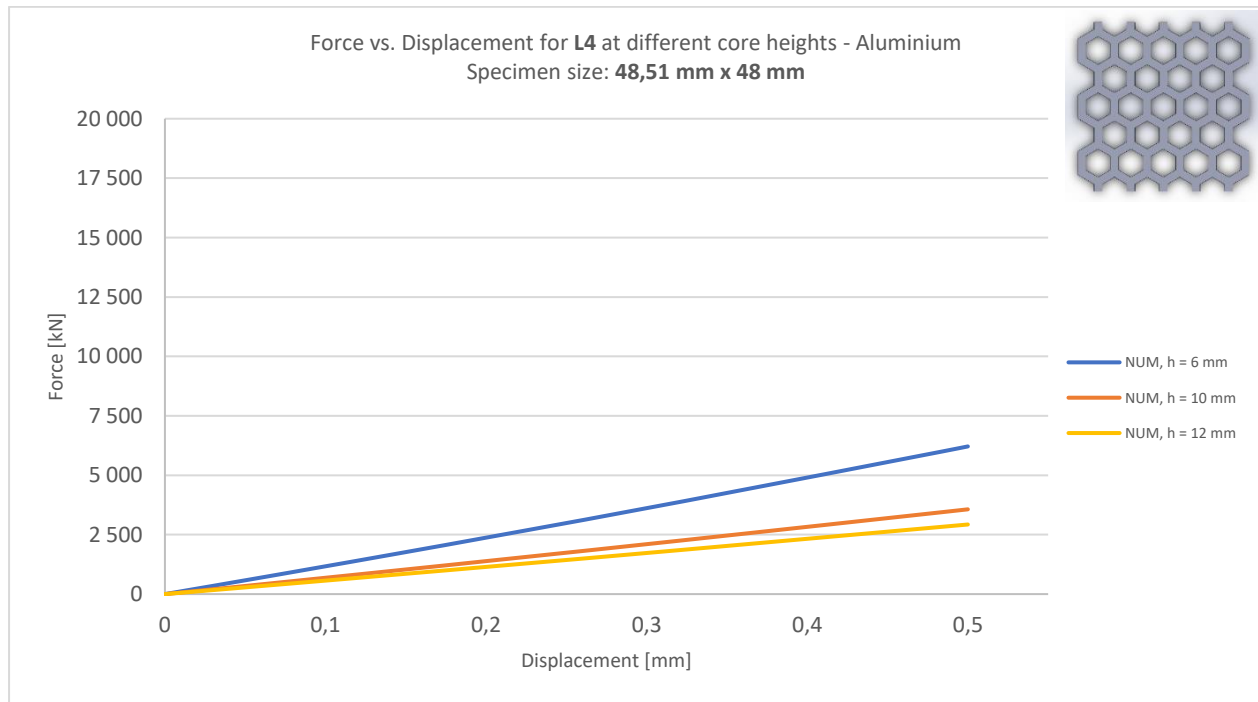
4.2.2 Aluminium

4.2.2.1 Regular structures

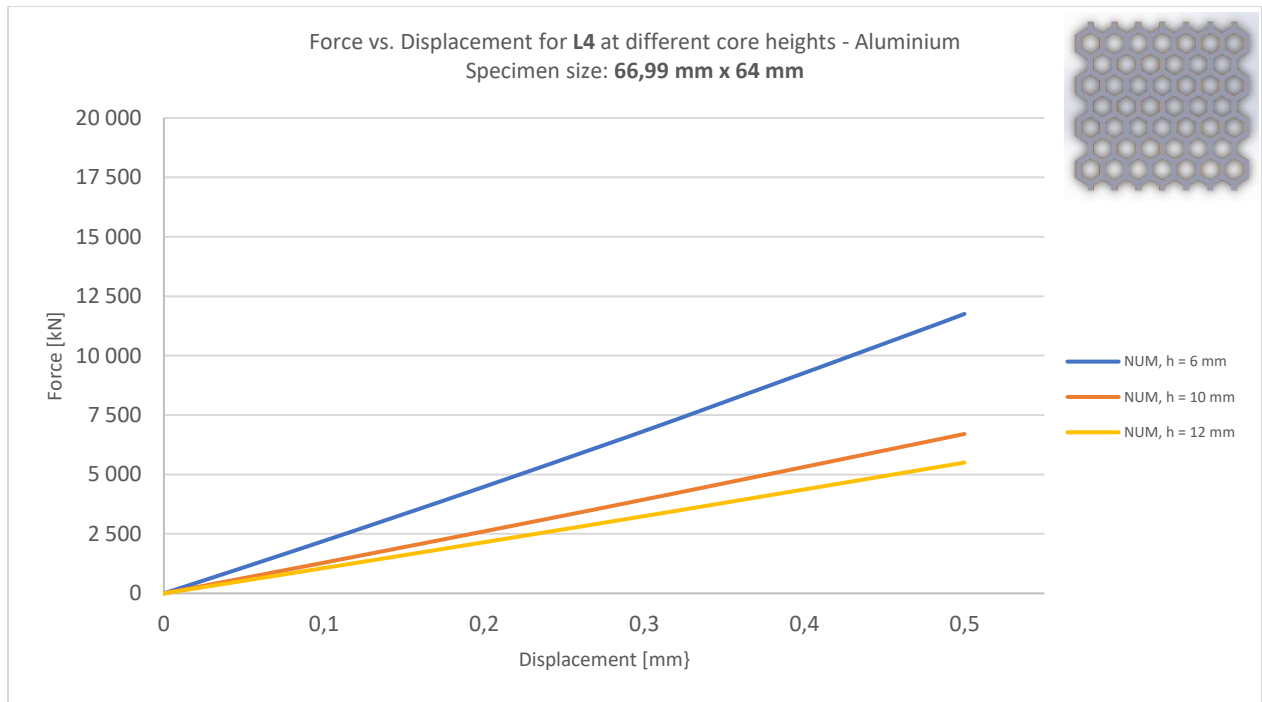
The results obtained for Aluminium regular structures are presented below on figure 4.7. The plots are organised according to the following scheme:

- Identical specimens on size that have been only submitted to numerical analysis (under only-elastic regime) have the results for core heights 6 mm, 10 mm and 12 mm on the same plot;
- Identical specimens on size that have been submitted to both numerical analysis and experimental test have one plot for core height 6 mm and 12 mm and one plot for the three experimental specimens of core height 10 mm plus the numerical analysis for the same height.

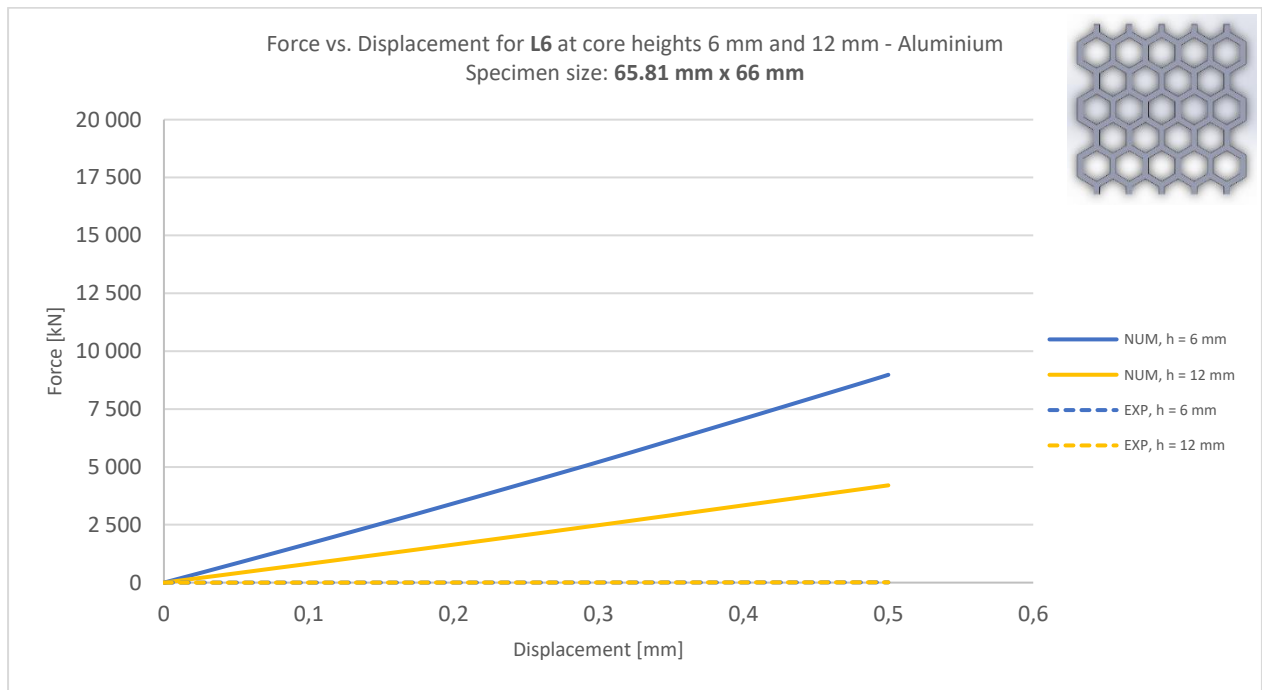
To what it comes on the experimental testing specimens, it was possible to observe that the force vs. displacement curves, compared to the numerical results, show very low values of force that are only achieved for displacements near 0.5 mm. Further ahead, in table 4.6 of section 4.3.2, the observed phenomenon is quite visible on the values of the study variables.



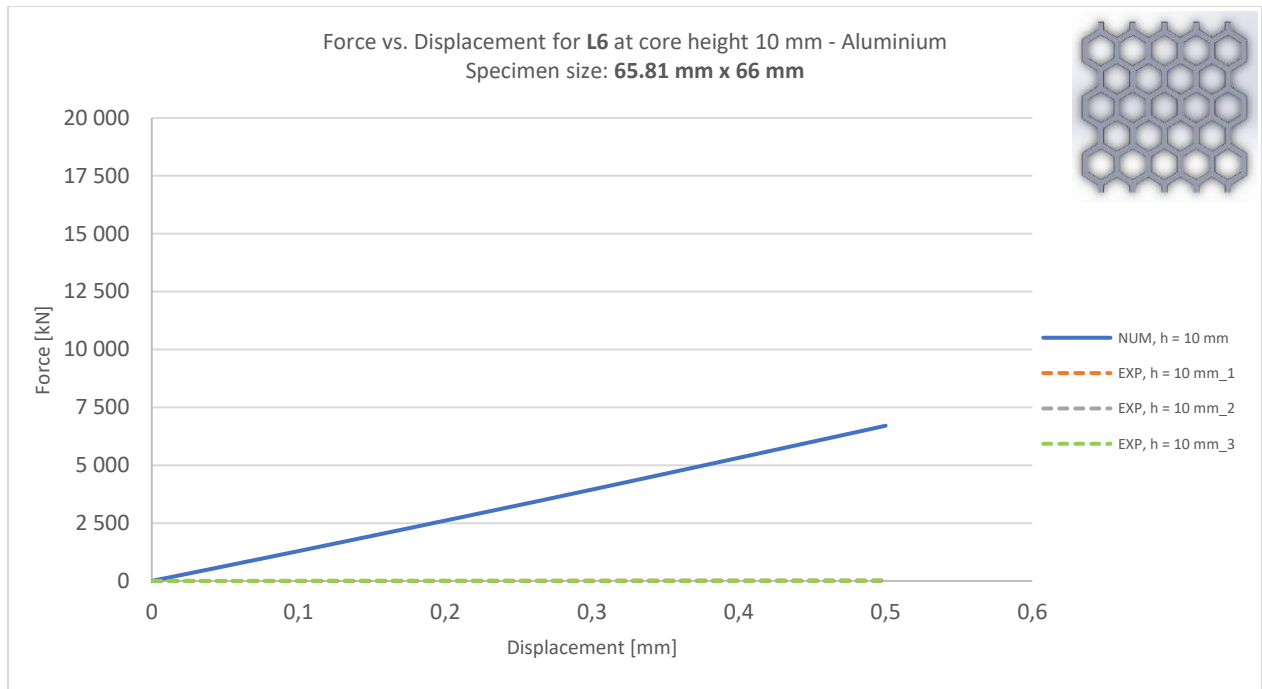
(a)



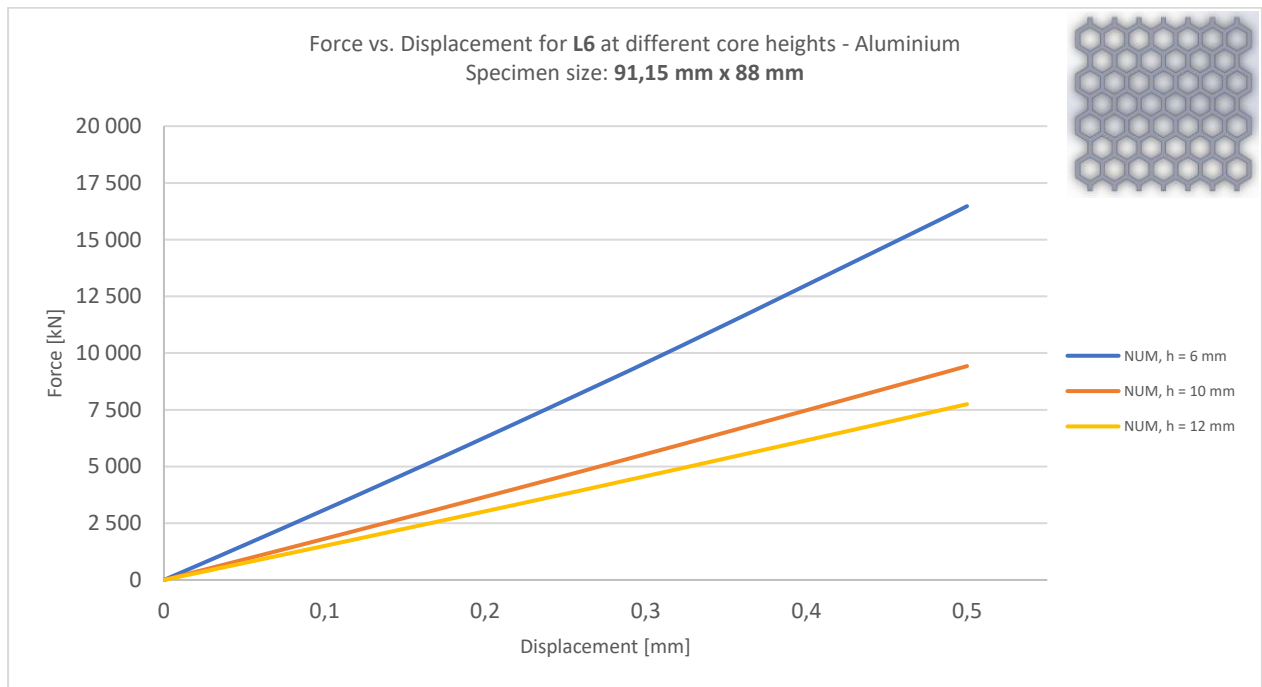
(b)



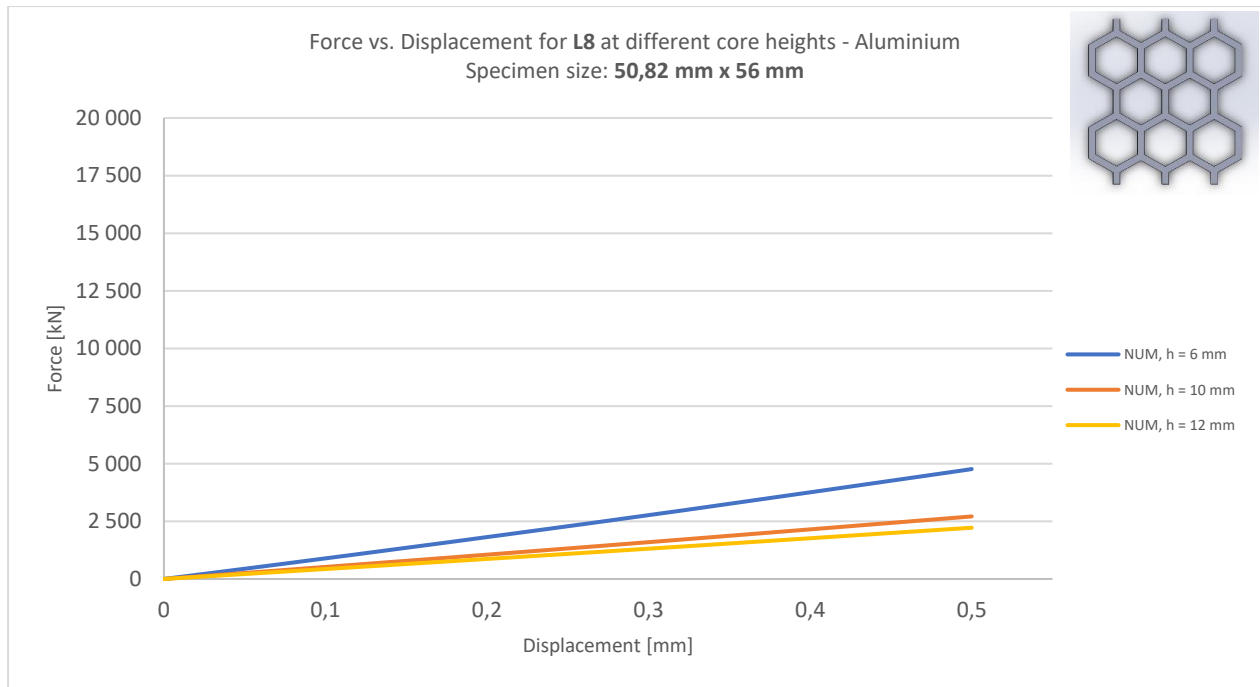
(c)



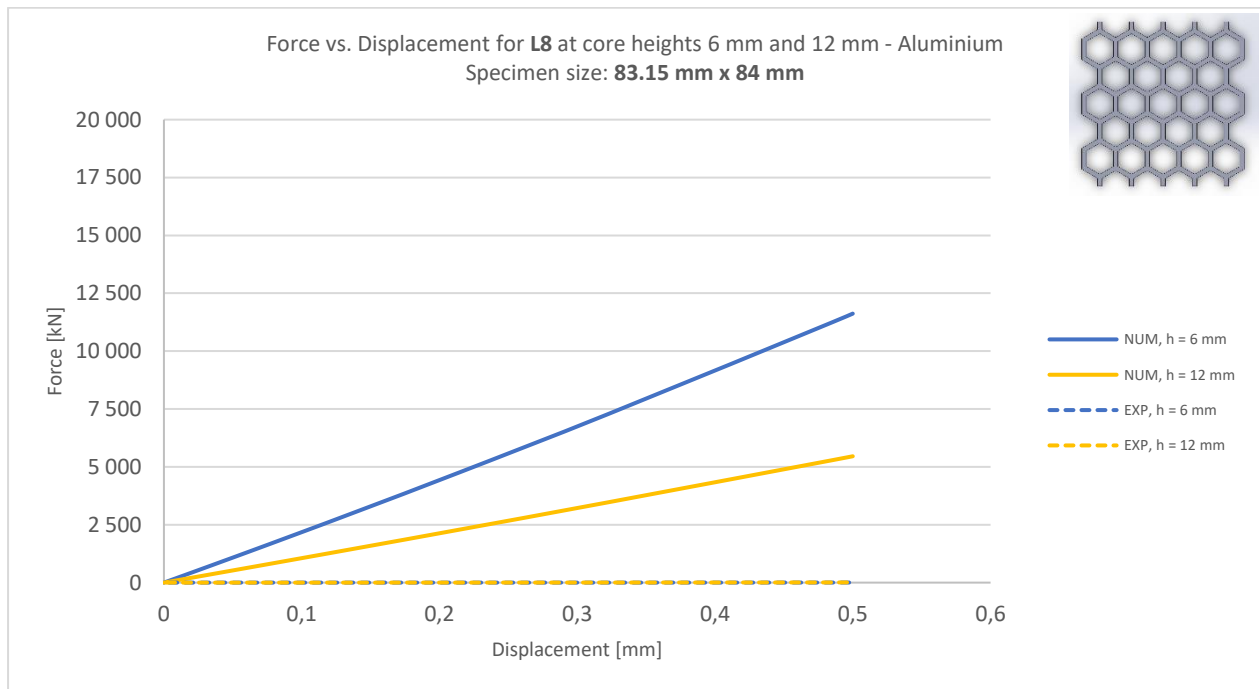
(d)



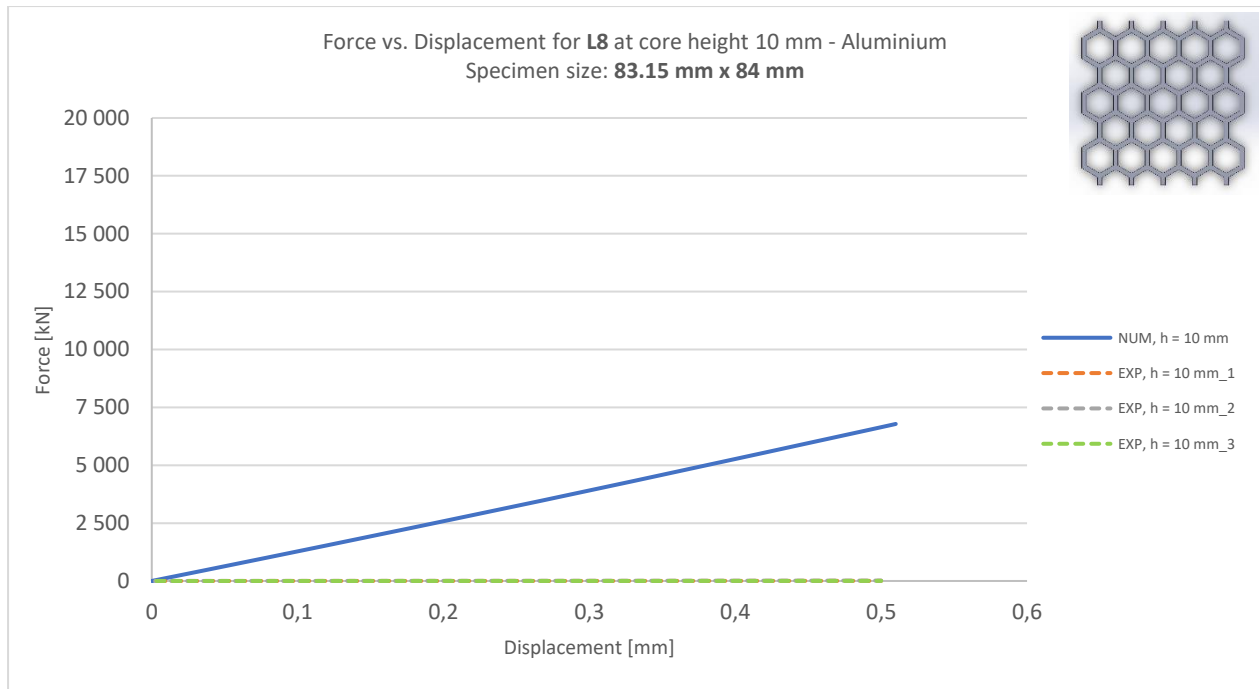
(e)



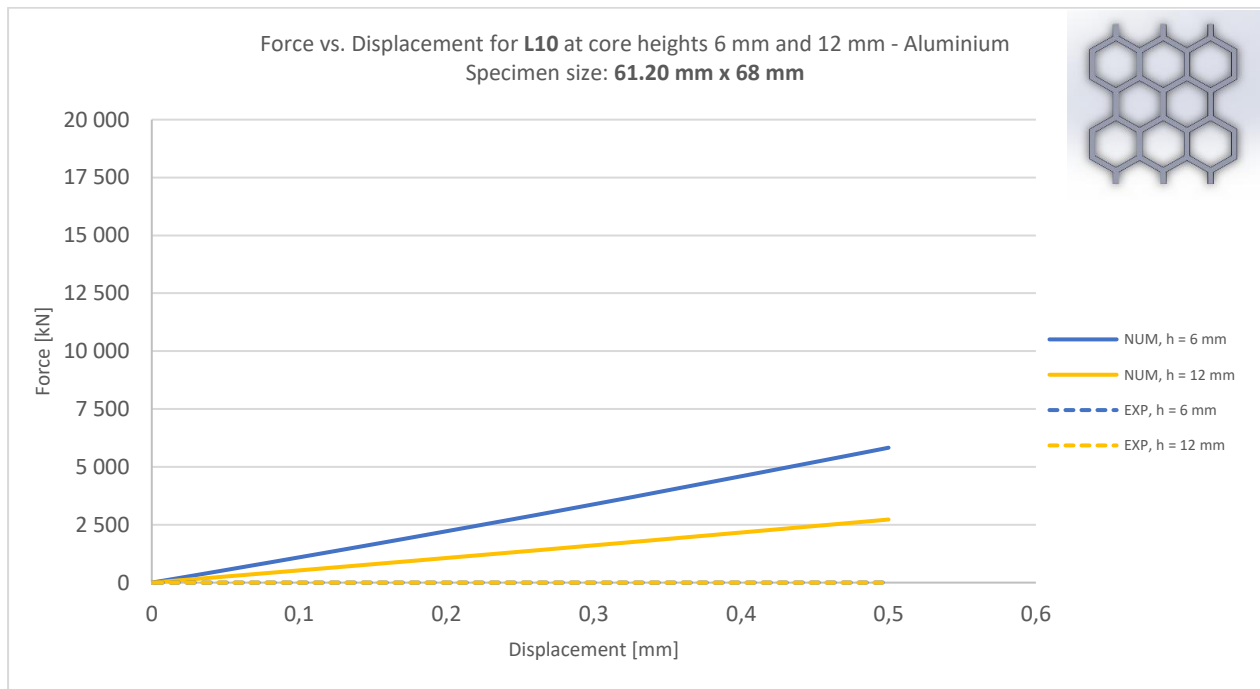
(f)



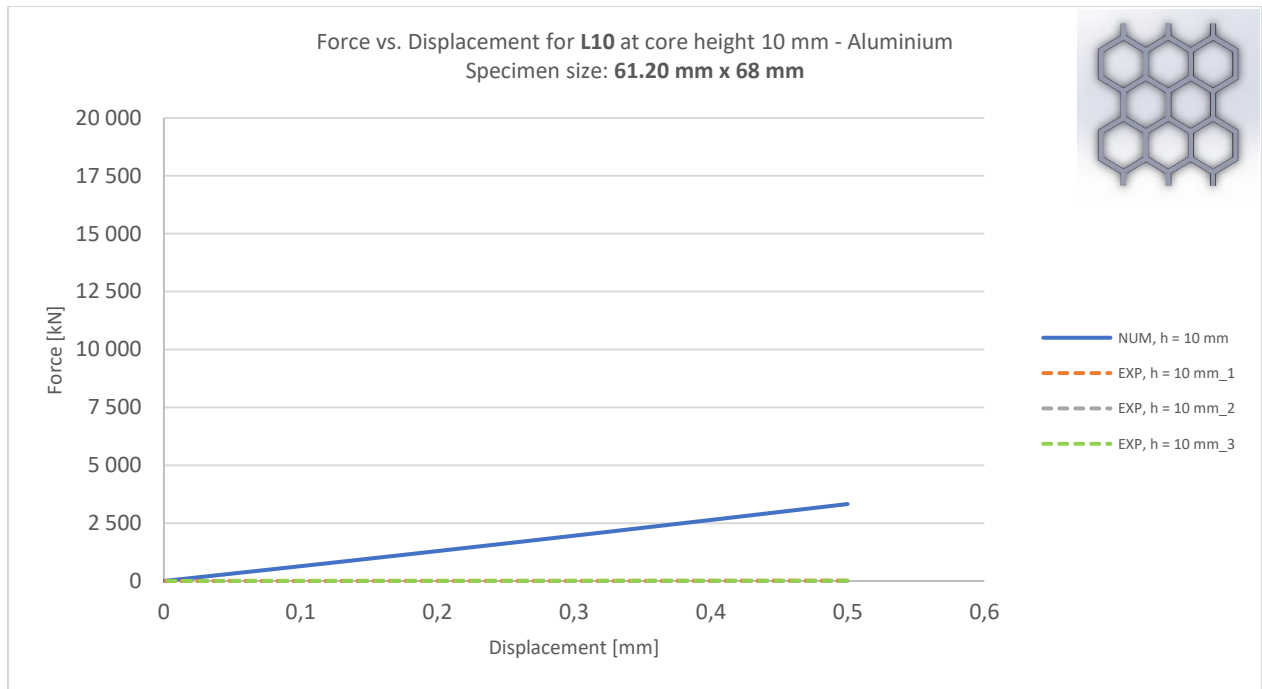
(g)



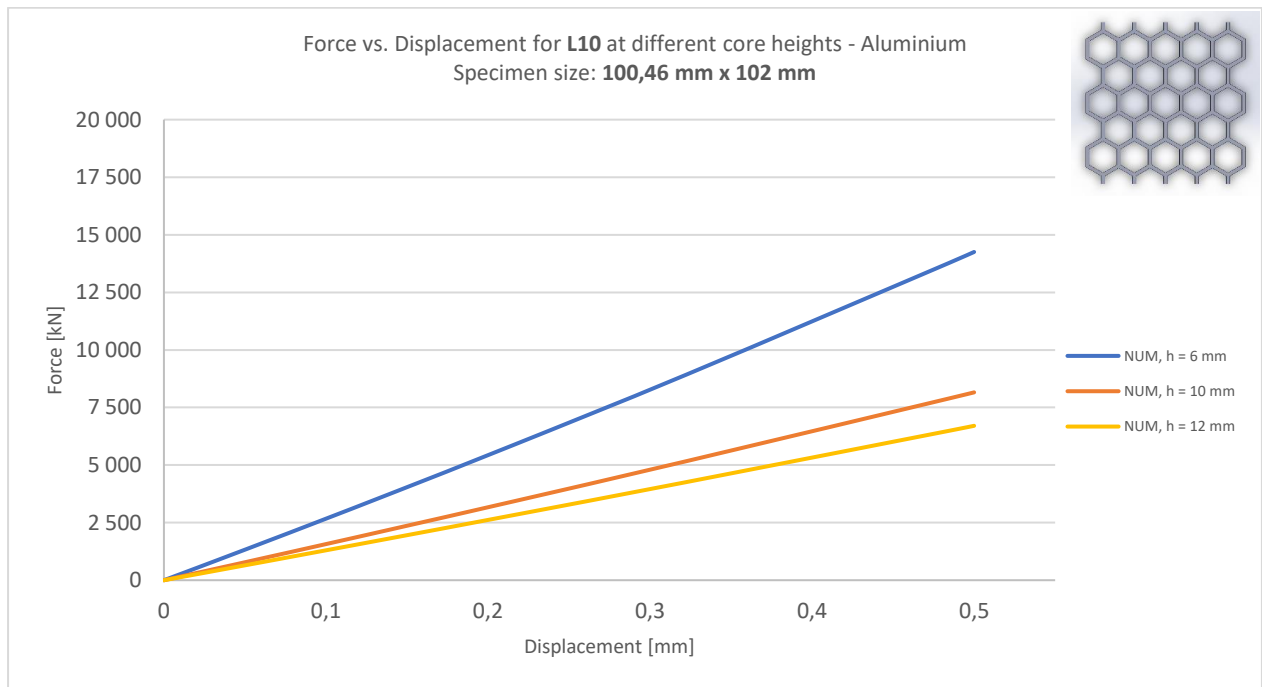
(h)



(i)



(j)



(k)

Figure 4.7 - Force vs. Displacement curves for Aluminium regular structures – Numerical and experimental results:
(a) (b) L4; (c) (d) (e) L6; (f) (g) (h) L8; (i) (j) (k) L10.

4.3 Discussion

In the treatment of the results, the first step was to compute three main study variables from the force vs. displacement curves: specific energy absorbed ($\frac{E_a}{\rho}$), specific stress ($\frac{\sigma}{\rho}$) and specific stiffness ($\frac{K}{\rho}$), until a fixed displacement of 0.1 mm for all cases (the maximum common displacement between all numerical analysis and experimental tests). As the relative density varies with the geometric parameters of each structure, it is important to normalize the variables, dividing the values from each structure by its relative density. In this way, the comparison of the same study variable between different geometries is valid.

The study variables are defined as follows:

- Stiffness is defined as the derivative of the force in order to the displacement; this means the slope of the force vs. displacement curve in the elastic region;
- Energy absorbed is defined as the integral of the force by the displacement; i.e., the area below the force vs. displacement curve until the considered value of displacement;
- Stress is defined as the measured value of the reaction force divided by the area of the structures.

Regarding the stress value, it is important to clarify that it is calculated dividing the force value (at the fixed displacement of 0.1 mm) over the solid area of the structure. It should be also mentioned that, regarding the experimental value of aluminium “h10” samples and PLA “h12” samples, it is an average of the variable value at the three structures that represent the same case (“h10_1”, “h10_2”, “h10_3” and “h12_1”, “h12_2”, “h12_3”), with the respective standard deviation.

4.3.1 PLA samples

4.3.1.1 Regular structures

Table 4.1 contains the numerical and experimental values – both conducted under elastic regime – for the three mentioned study variables at the PLA **regular structures**.

Table 4.1 - Specific energy absorbed, specific stiffness and specific stress for PLA regular structures – Numerical and experimental results.

	h [mm]	$\frac{E_a}{\rho}$ [kN.mm]		$\frac{K}{\rho}$ [kN/mm]		$\frac{\sigma}{\rho}$ [MPa]	
		Numerical	Experimental	Numerical	Experimental	Numerical	Experimental
L4 – 48.51 x 48	6	3.11	---	776	---	60	---
	10	1.90	---	454	---	39	---
	12	1.56	---	368	---	32	---
L4 – 66.99 x 64	6	5.60	---	1385	---	62	---
	10	3.37	---	798	---	38	---
	12	2.80	4.64 ± 0.76	656	1005 ± 92	31	49 ± 8
L6 – 65.81 x 66	6	6.43	---	1375	---	87	---
	10	3.37	---	799	---	49	---
	12	2.79	---	655	---	40	---
L6 – 91.15 x 88	6	11.25	---	2845	---	89	---
	10	6.57	---	1570	---	52	---
	12	5.43	7.10 ± 0.09	1277	1473 ± 136	43	53 ± 1
L8 – 50.82 x 56	6	3.93	---	999	---	99	---
	10	2.28	---	546	---	62	---
	12	1.88	---	443	---	51	---
L8 – 83.15 x 84	6	9.12	---	2270	---	101	---
	10	5.69	---	1302	---	62	---
	12	2.29	7.84 ± 0.33	1066	1696 ± 112	51	83 ± 4
L10 – 61.20 x 68	6	5.51	---	1385	---	120	---
	10	3.27	---	779	---	72	---
	12	2.71	---	636	---	60	---
L10 – 100.46 x 102	6	13.41	---	3349	---	121	---
	10	8.35	---	1998	---	76	---
	12	6.90	8.56 ± 1.01	1626	1701 ± 102	62	74 ± 9

Analysing the three study variables, it was possible to identify some patterns dependent on the geometrical properties of the specimens.

Regarding the **numerical analysis to regular structures**, the following was observed:

- There is an increase in the specific stiffness and specific energy absorbed with the increment of the specimen size;
- There is a decrease in the specific stiffness and specific energy absorbed with the increment of the core height for each structure.

This pattern is visible in all numerical analyses of the regular structures. Moreover, it appears that there is no significant influence of relative density in these two variables with distinct specimen size: structures with very similar relative density but with significantly different specimen size present very different values. However, for similar specimen size and different relative density, some differences in these two variables values are noted, even though it may not be significant. For instance, regarding the “L4 – 66.99 x 64” and “L10 – 61.20 x 68” with relative densities equal to 0.228 and 0.438 respectively, the values of both specific stiffness and specific energy absorbed are higher in the first one than the second one.

Given these observations, a hierarchy of the geometric variables and physical properties influence over the energy absorption capacity and stiffness of the structures may be established: the specimen size has the greatest influence on the out-of-plane behaviour of these structures. Apart from this, the relative density of the structures influences their energy absorption capacity and stiffness. Thus, the specimen size is the first variable to consider, followed by the relative density of the structures. Figures 4.8 and 4.9 highlight the identified patterns on the specific stiffness and the specific energy absorbed, respectively.

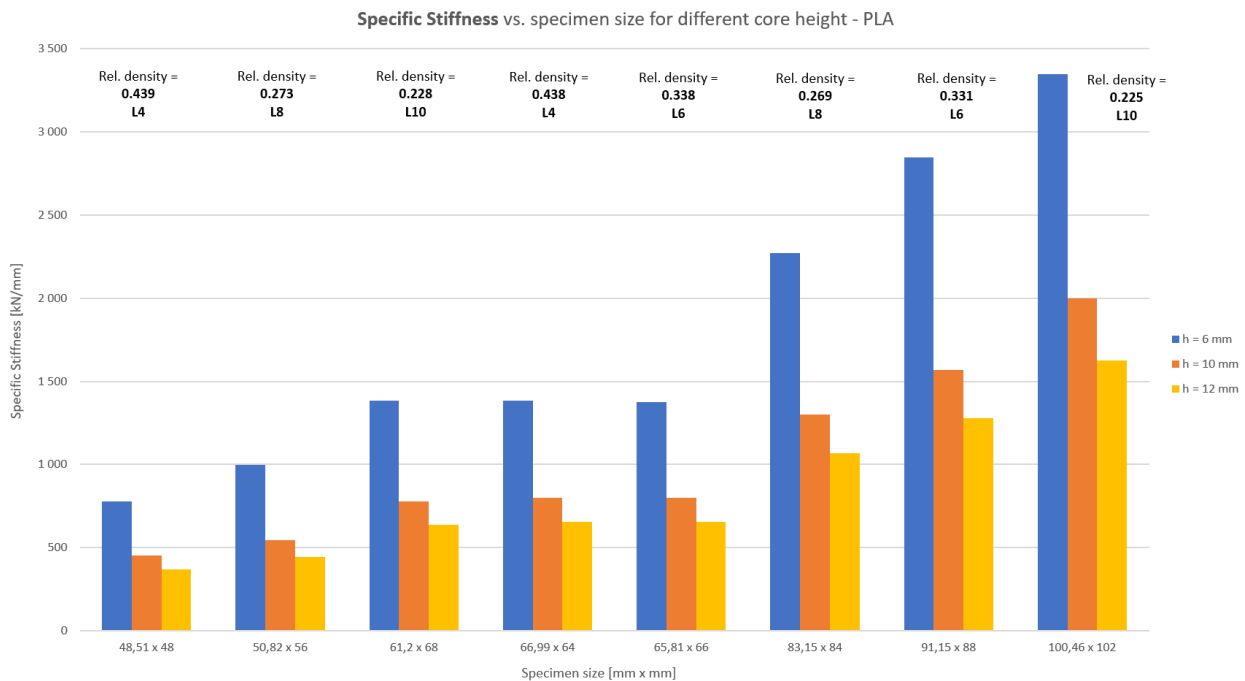


Figure 4.8 - Specific stiffness vs. specimen size for PLA regular structures – Numerical analysis.

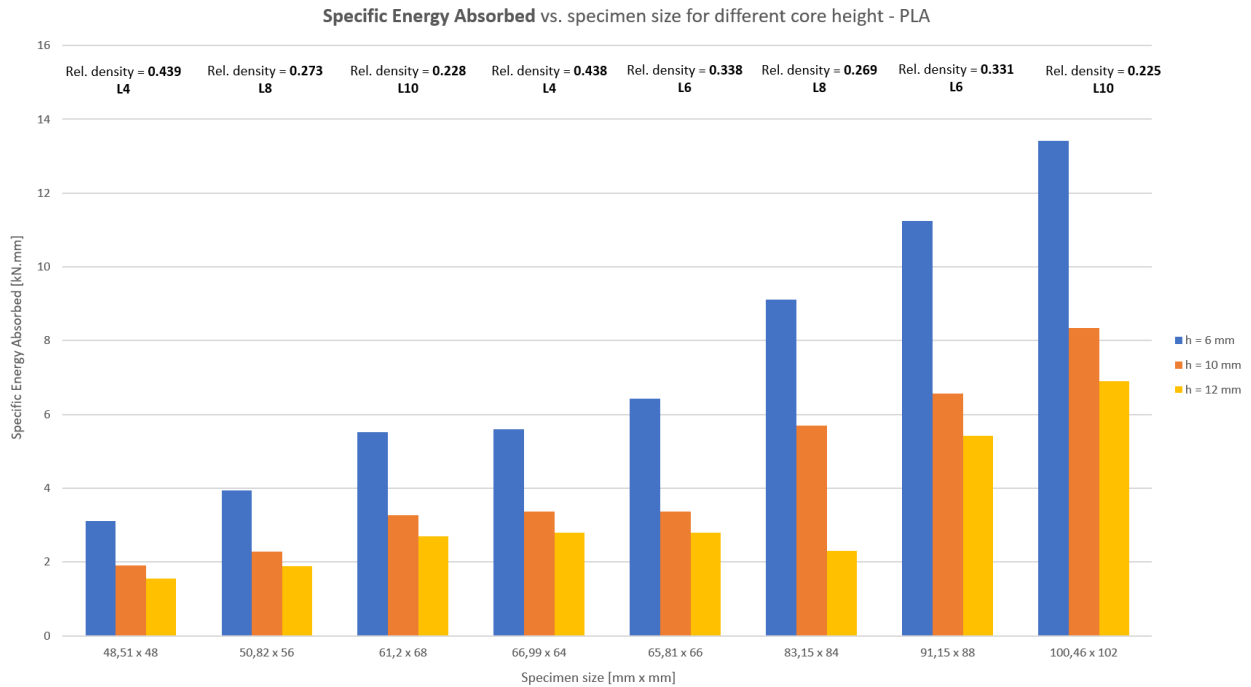


Figure 4.9 - Specific energy absorbed vs. specimen size for PLA regular structures – Numerical analysis.

Regarding the specific stress, it was observed that the higher the relative density of the structures is, the lower the specific stress is. Contrary to the energy absorption and stiffness, no relationship between the specimen size and the specific specimen size was identified. That said, it is possible to affirm that the stress magnitude on the structure is only dependent on the relative density. Relatively to the core height, the same was observed as in the specific stiffness and specific energy absorbed: the higher the core is, the lower is the value of the specific stress.

It is also important to refer that it wasn't established any direct influence of the cell length (l or "L") and the three study variables. However, the cell length pre-determines the relative density of the structure, having an indirect impact on the behaviour of the structure. The dependence of the specific stress on relative density is expressed in figure 4.10.

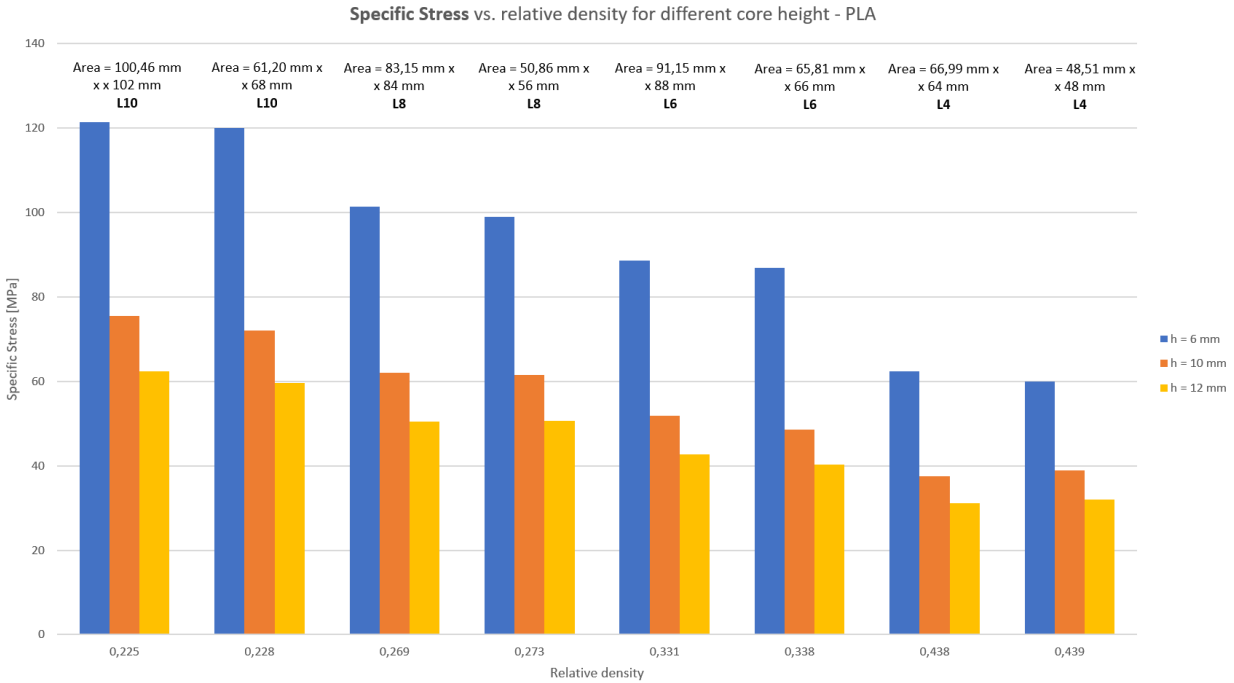


Figure 4.10 - Specific stress vs. relative density for PLA regular structures – Numerical analysis.

Regarding the **elasto-plastic numerical analysis** to the same structures, it is possible to verify that the transition from elastic to plastic regime happens generally for a displacement of (around) 0.2 mm, which can be confirmed by inspecting the force vs. displacement plots (figure 4.1). The specific stiffness, specific energy absorbed and specific stress are also evaluated in order to check if the patterns from the only-elastic analysis maintain.

Table 4.2 establishes a comparison of results between the only-elastic and the elasto-plastic numerical analysis on PLA regular structures.

Table 4.2 - Values of specific energy absorbed, specific stiffness and specific stress for only-elastic and elasto-plastic analysis – PLA regular structures.

	h [mm]	$\frac{E_a}{\rho}$ [kN.mm]		$\frac{K}{\rho}$ [kN/mm]		$\frac{\sigma}{\rho}$ [MPa]	
		O.Elastic	Elasto-plastic	O.Elastic	Elasto-plastic	O.Elastic	Elasto-plastic
L4 – 48,51 x 48	6	3.11	3.10	776	671	60	60
	10	1.90	1.90	454	413	39	39
	12	1.56	1.56	368	339	32	32
L4 – 66,99 x 64	6	5.60	5.59	1385	1211	62	62
	10	3.37	3.37	798	732	38	39
	12	2.80	2.80	656	609	31	31
L6 – 65,81 x 66	6	6.43	5.59	1375	1239	87	84
	10	3.37	3.37	799	736	49	49
	12	2.79	2.79	655	607	40	40
L6 – 91,15 x 88	6	11.25	11.18	2845	2464	89	88
	10	6.57	6.57	1570	1438	52	52
	12	5.43	5.43	1277	1179	43	43
L8 – 50,82 x 56	6	3.93	3.91	999	861	99	100
	10	2.28	2.28	546	500	62	60
	12	1.88	1.88	443	418	51	51
L8 – 83,15 x 84	6	9.12	9.09	2270	1996	101	101
	10	5.69	5.69	1302	1197	62	62
	12	4.45	4.55	1066	663	51	51
L10 – 61,20 x 68	6	5.51	5.49	1385	1207	120	121
	10	3.27	3.27	779	715	72	72
	12	2.71	2.71	636	592	60	60
L10 – 100,46 x 102	6	13.41	13.37	3349	2937	121	121
	10	8.35	8.35	1998	1827	76	76
	12	6.90	6.90	1626	1509	62	62

Looking at the elasto-plastic results for the specific stiffness, it is noted that the values from this analysis are slight lower than the only-elastic ones. This may be associated to error accumulation on the calculation due to changes between the criteria in only-elastic regime and in elasto-plastic regime. This might also be

associated to local plastic deformation on the upper contact interface (between the structure and the upper plate) that may be occurring, even if it may be negligible.

Taking a look at the variation of the values on this last analysis, the same patterns at the only-elastic analysis are identified: the values of specific stiffness and specific energy absorbed vary mainly with the specimen size and secondly with the relative density. Furthermore, the specific stiffness and the specific energy absorbed also vary with the core height, repeating the same pattern as in the only-elastic simulation. Regarding the specific stress, the relative density pattern is also identified: the higher the relative density is, the lower the stress is. Also, the stress in structures decreases with the decrement of the core height, equally to what was observed at the only-elastic simulation. The bar charts that evidence the patterns of the geometrical influence over the structures behaviour can be found at the appendix C.

On the other hand, regarding the **experimental tests on regular specimens**, different patterns were identified relatively to the studied variables. In the three variables, the specimen size influence wasn't determined in the results, being the relative density the main factor to influence the specimen's behaviour: as the relative density increases, the specific stiffness and specific energy absorbed decrease. Reviewing the results for the "L8 – 83.15 x 84" and "L6 – 91.15 x 88", with relative densities 0.269 and 0.331 respectively, the specific stiffness and the specific energy absorbed are higher on the first one, even though its specimen size is smaller than the second one and contrary to the numerical analysis. However, with the exception for these two cases, there is a notable difference in stiffness and energy absorption between the larger and the smaller specimens: the first one has better stiffness and energy absorption capacity. This may also be verified comparing the "L10 – 100.46 x 102", "L6 – 91.15 x 88" and "L4 – 66.99 x 64": the first structure has higher values of specific stiffness and specific energy absorption than the second one, being the last structure the one with lower values. Samples with the similar relative density and different specimen size would have confirmed which one of these factors has the greatest contribution regarding the energy absorption capacity and stiffness of the structure.

Looking to the specific stress, it is possible to verify in figure 4.11 that the experimental specimens follow the same behaviour as the numerical models: generally, the higher the relative density is, the lower is the specific stress.

As the specimens were tested at a constant height, the relationship between the core height and the study variables wasn't evaluated.

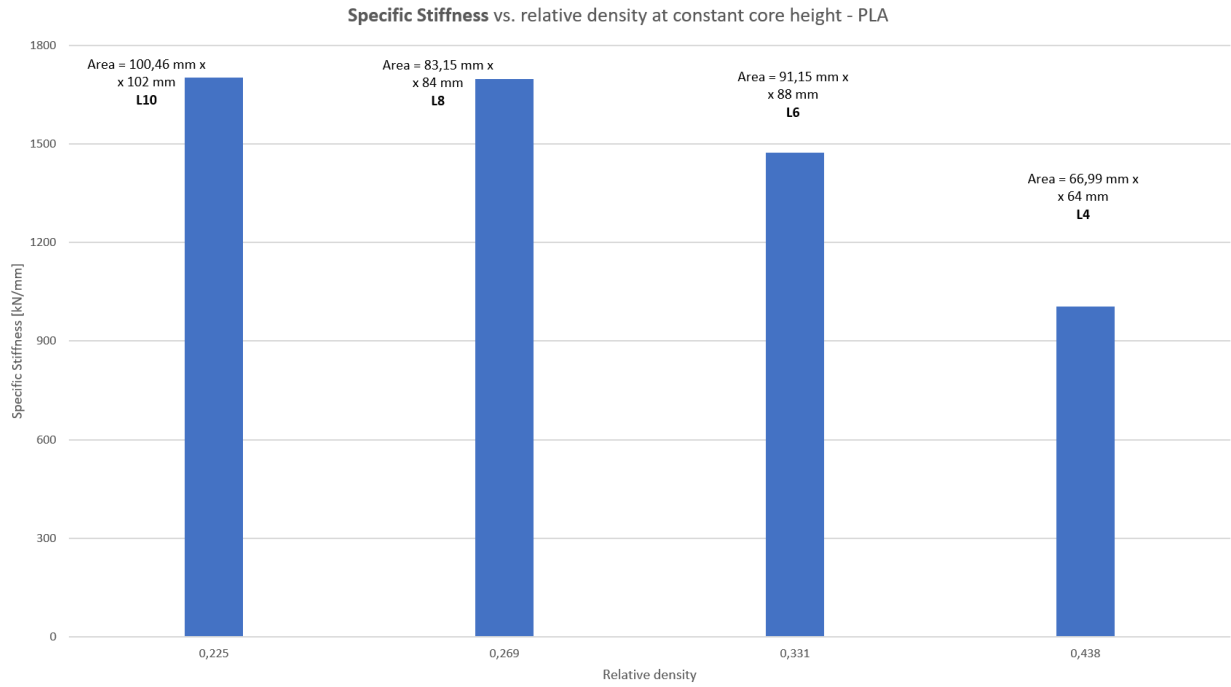


Figure 4.11 - Specific stiffness vs. relative density at PLA regular structures – Experimental test.

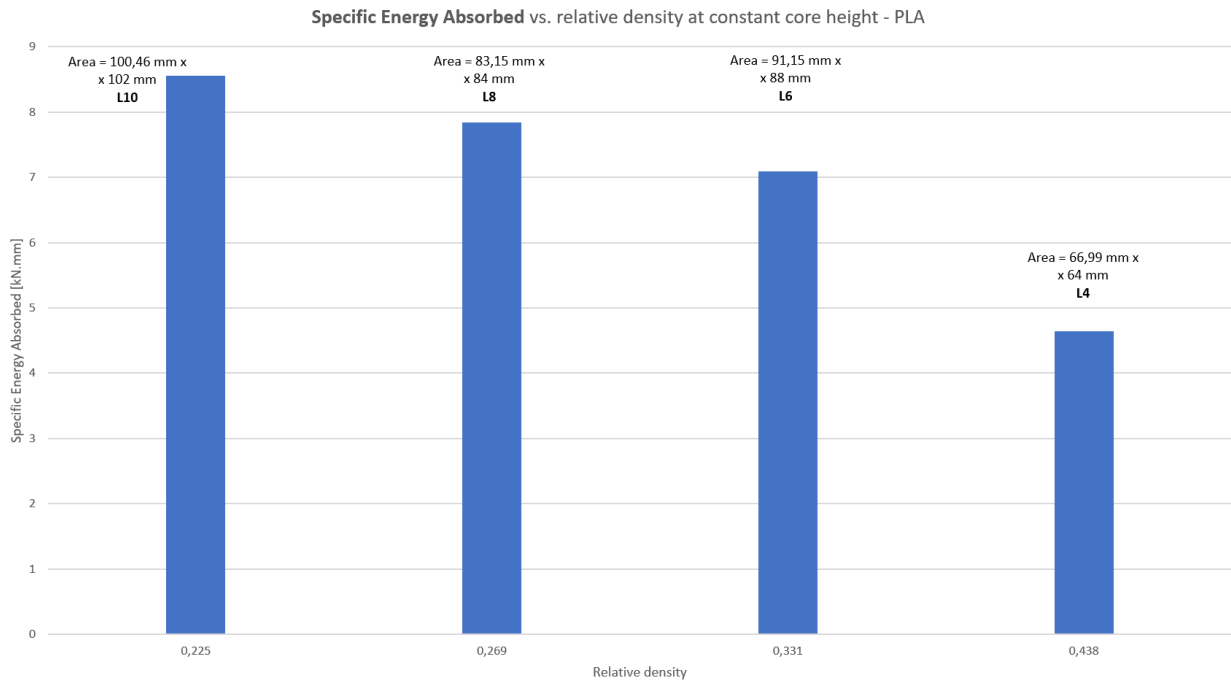


Figure 4.12 - Specific energy absorbed vs. relative density at PLA regular structures – Experimental test.

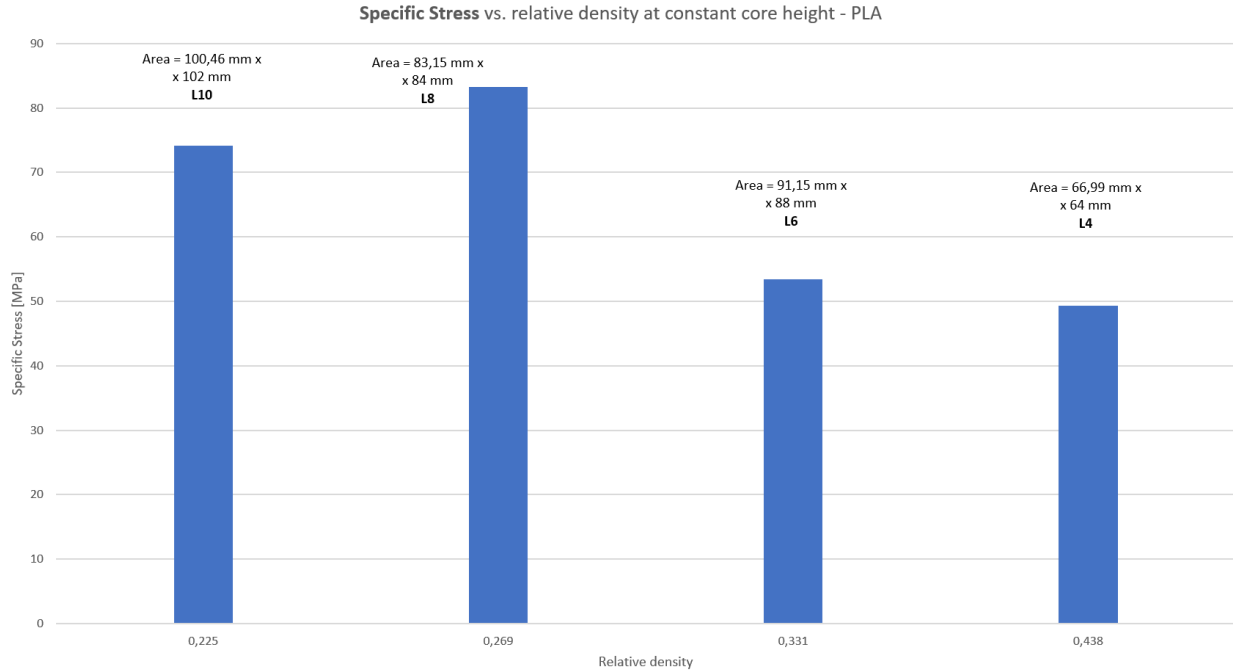


Figure 4.13 - Specific stress vs. relative density at PLA regular structures – Experimental test.

4.3.1.2 Graded structures

In what concerns to the PLA **graded structures**, tables 4.3, 4.4 and 4.5 contain the numerical and experimental values – both conducted under elastic regime – for the three mentioned study variables.

Table 4.3 - Numerical and experimental values of specific energy absorbed, specific stiffness and specific stress – PLA graded structures (first design method).

	h [mm]	$\frac{E_a}{\rho}$ [kN.mm]		$\frac{K}{\rho}$ [kN/mm]		$\frac{\sigma}{\rho}$ [MPa]	
		Numerical	Experimental	Numerical	Experimental	Numerical	Experimental
T6-8-10	12	5.17	5.52 ± 1.08	1298	1302 ± 57	43	38 ± 5
T10-8-6	12	5.50	---	1362	---	29	---

Table 4.4 - Numerical and experimental values of specific energy absorbed, specific stiffness and specific stress – PLA graded structures (second design method).

	h [mm]	$\frac{E_a}{\rho}$ [kN.mm]		$\frac{K}{\rho}$ [kN/mm]		$\frac{\sigma}{\rho}$ [MPa]	
		Numerical	Experimental	Numerical	Experimental	Numerical	Experimental
S0,5- _10	12	6.00	---	1690	---	29	---
S0,5- _20	12	---	5.32 ± 0.45	---	1343 ± 468	---	25 ± 2
S0,5+ _10	12	6.15	---	1705	---	28	---
S0,5+ _20	12	6.35	5.03 ± 0.30	1712	1036 ± 176	27	20 ± 0

Table 4.5 - Numerical and experimental values of specific energy absorbed, specific stiffness and specific stress – PLA graded structures (third design method).

	h [mm]	$\frac{E_a}{\rho}$ [kN.mm]		$\frac{K}{\rho}$ [kN/mm]		$\frac{\sigma}{\rho}$ [MPa]	
		Numerical	Experimental	Numerical	Experimental	Numerical	Experimental
R1 = + 0,22	12	4.53	---	1284	---	44	---
R1 = + 0,31	12	4.17	5,97 ± 0.88	1252	1714 ± 412	53	53 ± 8
R1 = + 0,37	12	---	---	---	---	---	---
R1 = - 0,22	12	3.78	---	1246	---	56	---
R1 = - 0,31	12	3.95	5.81 ± 0.29	1242	1630 ± 192	50	49 ± 2
R1 = - 0,37	12	4.41	---	1276	---	41	---

Regarding the **numerical analysis to gradient structures**, there were identified some similarities with the regular structures, regarding the influence of geometric parameters on the structures behaviour.

In what concerns to the specific stiffness and specific energy absorbed, it was identified the specimen size pattern: the values of these two variables increase with the specimen area; i.e., smaller structures absorb less energy, as well as they are less stiff. However, given that the structures of each design method have the same specimen size but different relative densities and mass distributions, a closer inspection to the results made possible the observation that, for the same specimen size, structures with higher relative density show higher values of stiffness and energy absorption. This is visible in the:

- first design method structures, where the “T10-8-6” structure (with relative density equal to 0.421) presents higher specific stiffness and higher specific energy absorbed than the “T6-8-10” structure (with relative density equal to 0.332);
- second design method structures, where the higher the relative density is, the higher the values of these two variables are.

Further inspection to the third design method structures allows the identification of the relative density pattern identified above: in general, structures with higher relative density present higher values of energy absorption and stiffness. Nevertheless, the magnitude of the gradient and its signal have an influence over these study variables. The results show that:

- For the same absolute value of gradient, a positive gradient has better energy absorption and a greater stiffness than a negative gradient. This may be observed for the $R_1 = + 0.31$ and $R_1 = - 0.31$ structures, where the first one has higher values than the second one, even though its relative density is lower than the last one (0.265 and 0.298, respectively);
- For structures with positive gradient, the lower the gradient is, the higher the values of these two variables are;
- For structures with negative gradient, the higher the gradient is, the higher the values of these two variables are.

Given the observations above it is then possible to state that structures with a positive R_1 coefficient perform better than the ones with a negative R_1 coefficient. Also, it is correct to affirm that the denser the structure is around the symmetry planes (as it is the case of the “ $R_1 = +0.22$ ” structure), the better their performance is. This makes possible to conclude that the mass distribution is an important factor when it comes to the influence of geometrical parameters in the structure’s out-of-plane performance: bringing more mass around the centre of structure enhances the stiffness and the energy absorption capacity of these structures.

Figures 4.14, 4.15 and 4.16 highlight the patterns for specific stiffness, specific energy absorbed and specific stress, respectively.

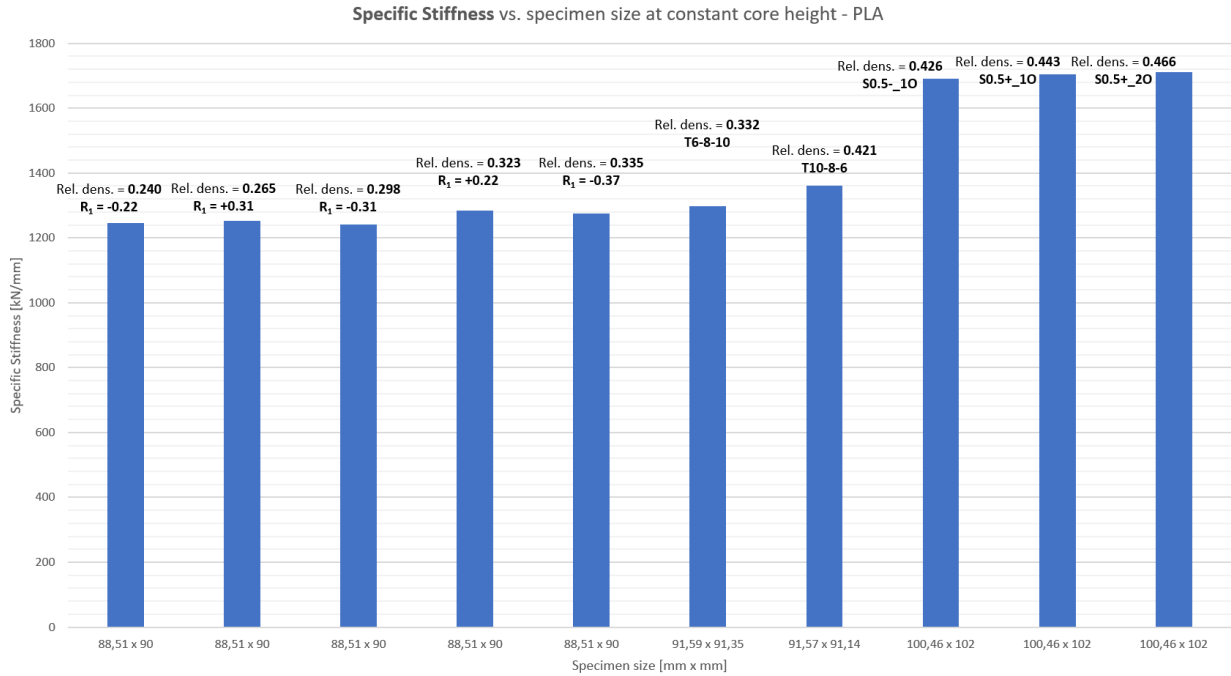


Figure 4.14 - Specific stiffness vs. specimen size at PLA graded structures – Numerical analysis.

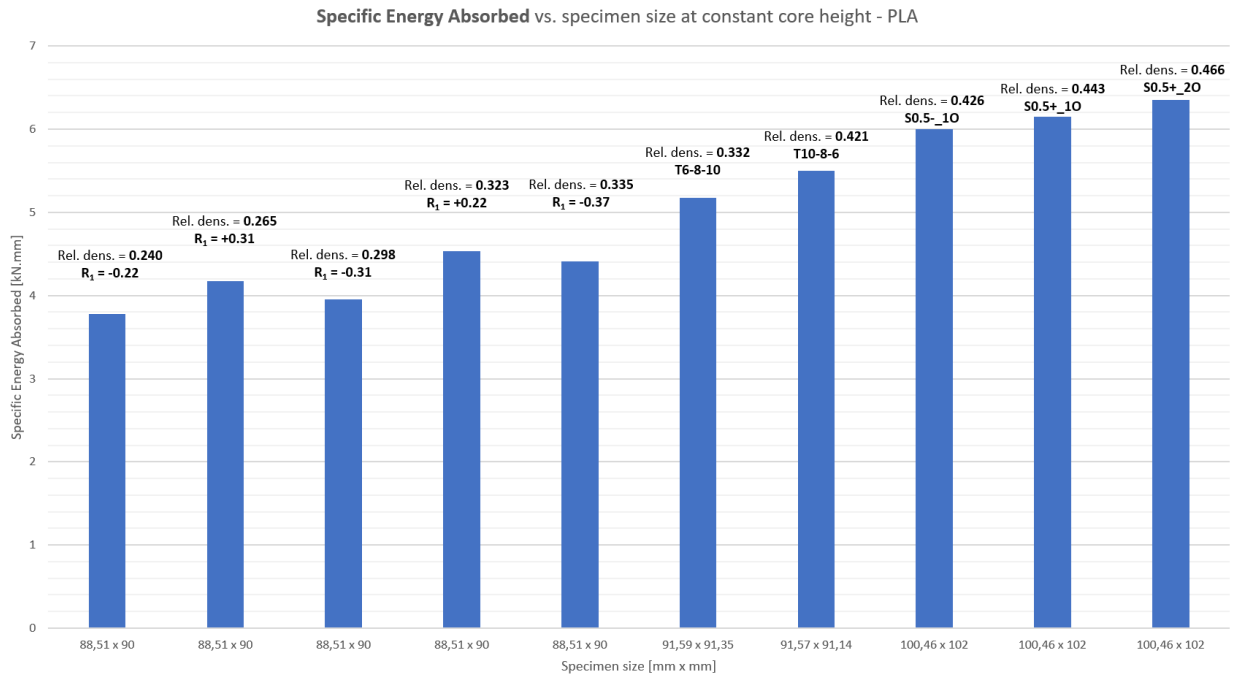


Figure 4.15 - Specific energy absorbed vs. specimen size at PLA graded structures – Numerical analysis.

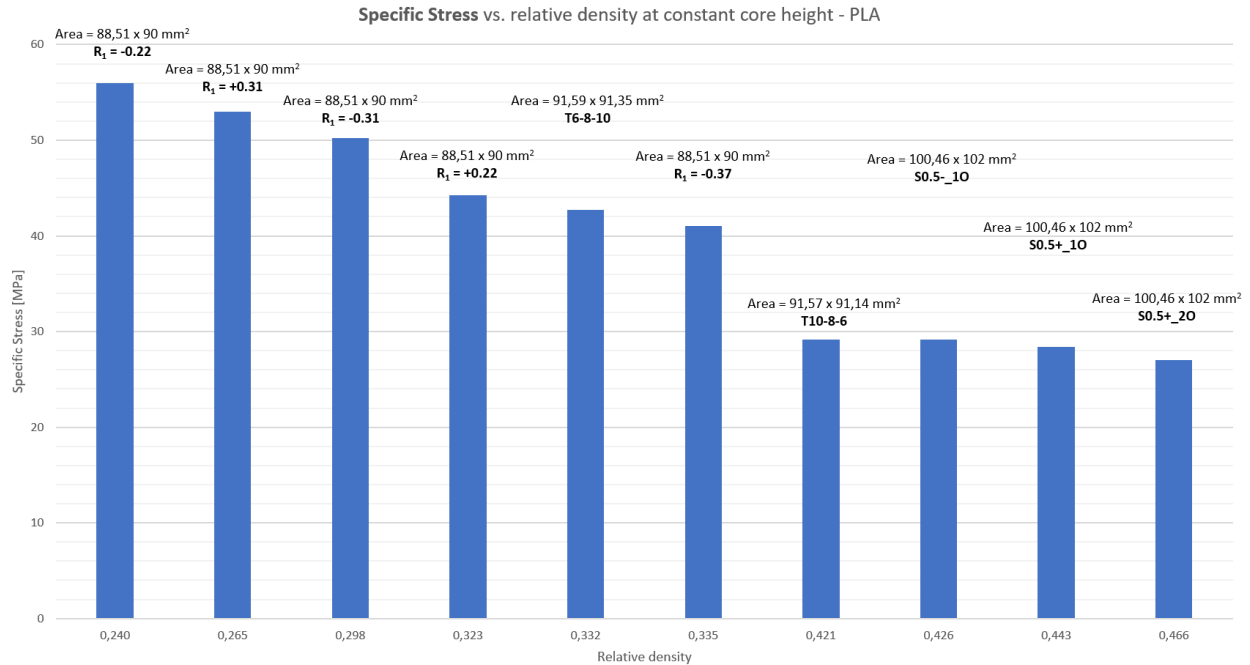


Figure 4.16 - Specific stress vs. relative density at PLA graded structures – Numerical analysis.

Based only on the numerical analyses and once the patterns are established, it is possible to properly identify a hierarchy of the parameters influence over the out-of-plane performance of structures: the specimen size has the greatest importance regarding the stiffness and the energy absorption – structures with higher specimen size perform better in both regular and graded structures. On a next level, the relative density is the most important parameter. For the same specimen size, structures tend to perform better with higher relative density values. In last place, and specifically for the graded structures, the mass distribution impacts the performance of these structures under out-of-plane conditions. Structures with a positive gradient and a lower absolute value perform better; i.e., a higher mass concentration next to the centre cell enhances the structures stiffness and the energy absorption capacity, under out-of-plane loadings.

Regarding the specific stress, the results show the exact same pattern as in the regular structures: there is no influence of the geometric parameters or physical properties, other than the relative density of the structures; i.e., the higher the relative density is, the higher is the specific stress on the structure. The same pattern was identified among all graded geometries of the three design methods.

In what concerns to the **experimental tests on graded specimens**, like in the regular structures case, the structures behaviour differs from the one detected on the numerical results and doesn't follow some of the trends on the experimental results at the regular structures: the specific stiffness (in general) decreases with the increase of the relative density, and contrary to the numerical analysis on graded structures, the specimen size appears to have no effect on this matter. Although looking at "S0.5+_20" and "T6-8-10" it may appear that the specimen size has greater impact than the relative density, the "S0.5+_20" structure contradicts this fact, as it has the same specimen size as "S0.5+_20" but distinct specific stiffness values.

The “S0.5-_20” specimen is also the one with higher deviation in the specific stiffness values, hence this “out-of-pattern” behaviour may also be attributed to the experimental error. Regarding the specific energy absorbed, it is possible to observe that, the higher the relative density is, the lower the energy absorption is. Moreover, it is possible to verify that structures with larger dimensions not only absorb less energy, as it can also be noted that structures with similar specimen size but different relative density have different values of specific energy absorbed. Based on the experimental testing results, it is then possible to affirm that an increase in relative density results in lower energy absorption and lower stiffness, being these two variables independent from the specimen size. The mass distribution factor is once again verified: structures with more mass concentration near the centre have their energy absorption enhanced and higher stiffness. Regarding the specific stress, the results are in accordance with both numerical and experimental results, on regular and graded structures: in general, this value increases as the relative density increases, disregarding the interest of the specimen size in the strength of the structures.

Figures 4.17, 4.18 and 4.19 highlight the patterns for specific stiffness, specific energy absorbed and specific stress, respectively.

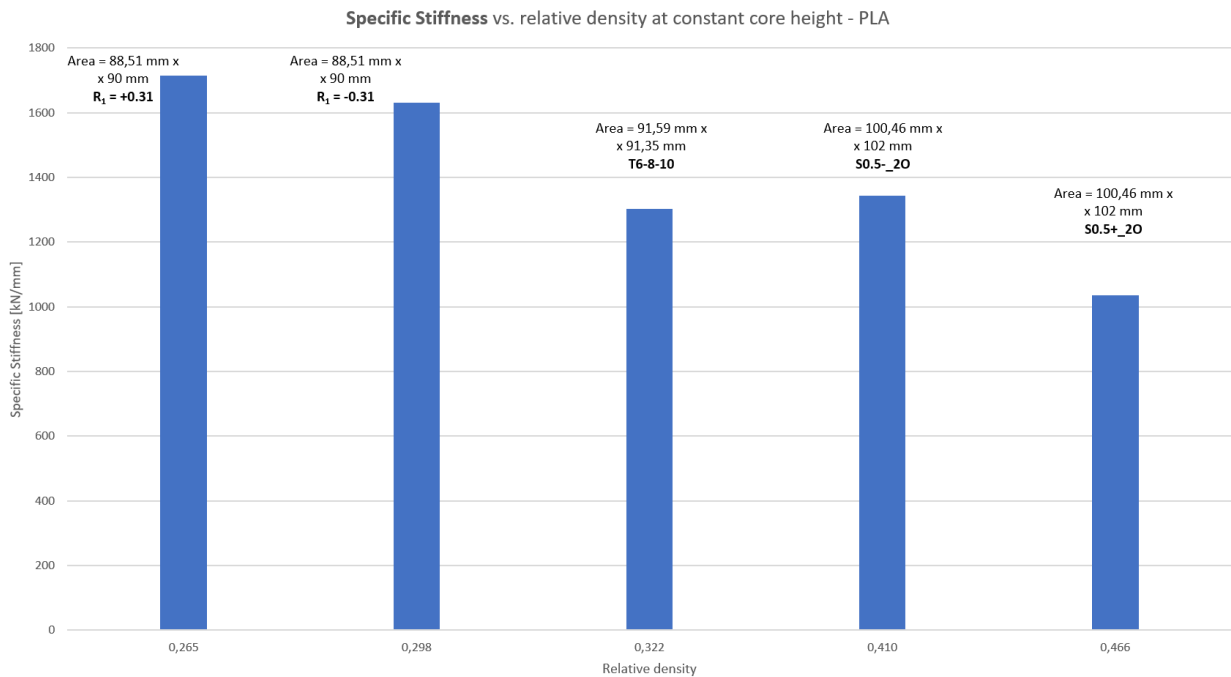


Figure 4.17 - Specific stiffness vs. relative density at PLA graded structures - Experimental test.

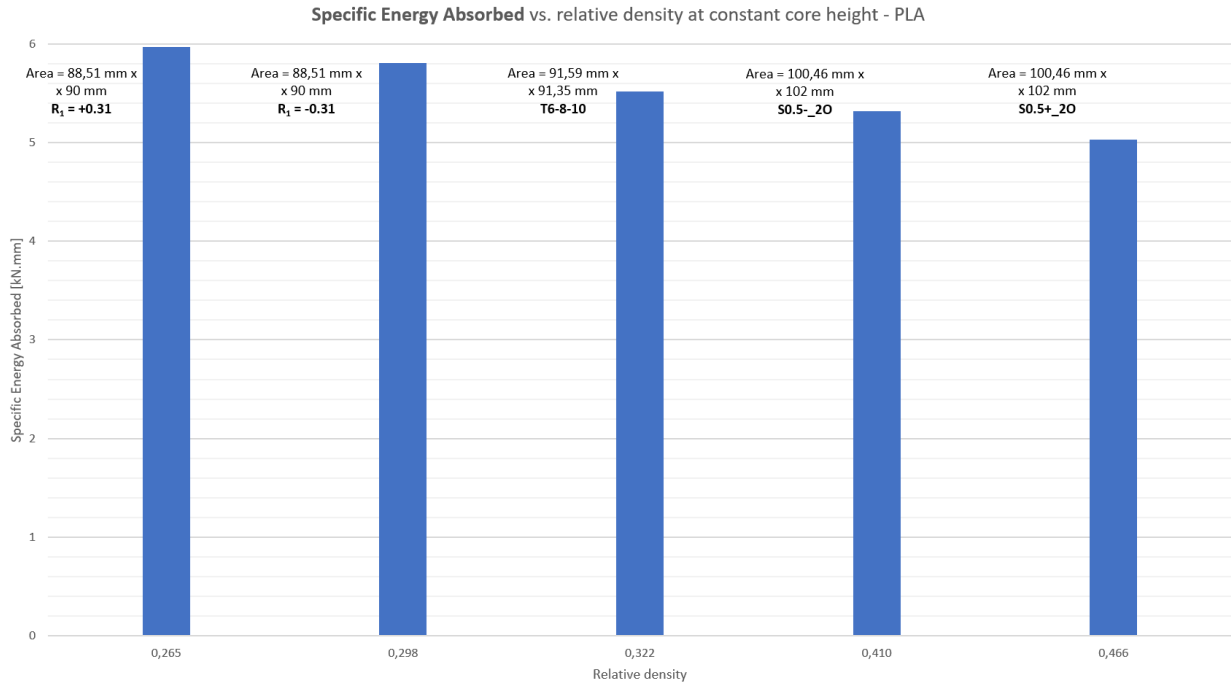


Figure 4.18 - Specific energy absorbed vs. relative density at PLA graded structures - Experimental test.

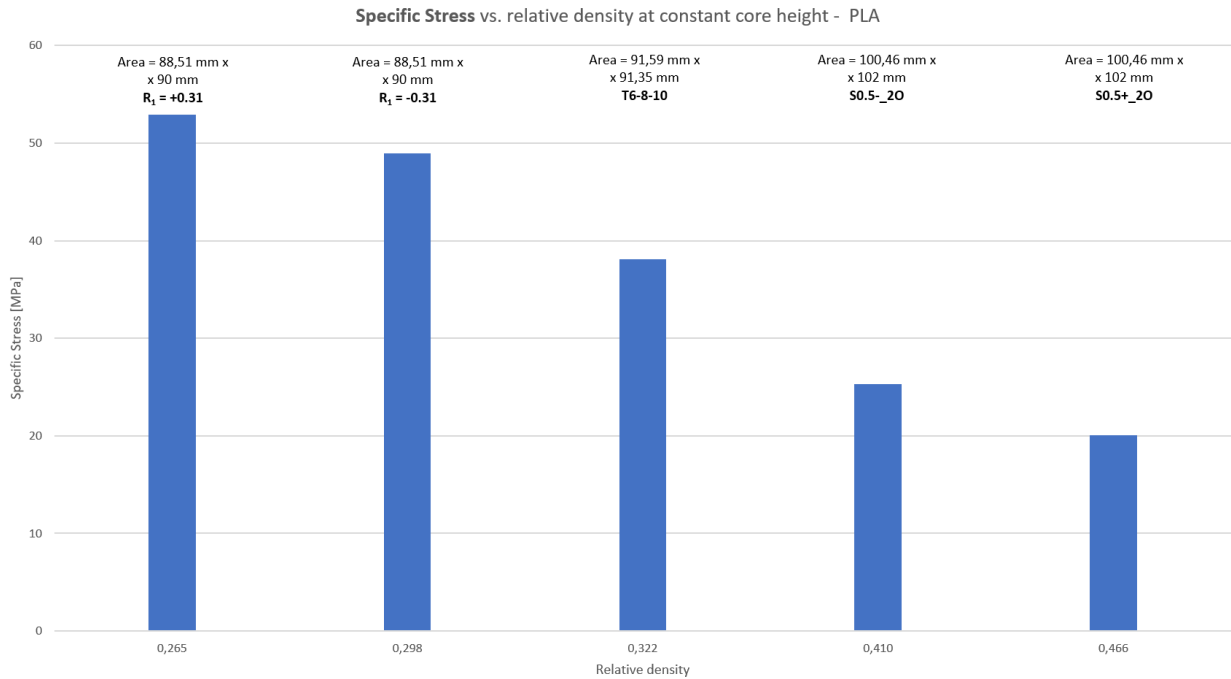


Figure 4.19 - Specific stress vs. relative density at PLA graded structures - Experimental test.

Some differences, although small, are noted in the values of the studied variables. That is due to the difference in the considered Young's Modulus: for the numerical analysis – as explained in section 3.1 – the considered value was the average between the Young's Modulus values of two previous works. As there was no technical data sheet available from the manufacturer, only after the completion of the experimental

tests, the specimens Young's Modulus was determined evaluating the slope of the elastic zone in the stress-strain curve. Evaluating the Young's Modulus at PLA regular structures, the mean value of each geometry's "h12" batch varies between 1872 MPa and 2352 MPa, which are normal values for this material as some literature may confirm [14, 23, 42]. Stress-strain curves for the PLA regular specimens can be found at the appendix B.

4.3.2 Aluminium samples

4.3.2.1 Regular structures

Table 4.6 contains the numerical and experimental values – both conducted under elastic regime – for the three mentioned study variables at the aluminium **regular structures**.

Table 4.6 - Specific energy absorbed, specific stiffness and specific stress for Aluminium regular structures – Numerical and experimental results.

	h [mm]	$\frac{E_a}{\rho}$ [kN.mm]		$\frac{K}{\rho}$ [kN/mm]		$\frac{\sigma}{\rho}$ [MPa]	
		Numerical	Experimental	Numerical	Experimental	Numerical	Experimental
L4 – 48,51 x 48	6	122	---	30426	---	2493	---
	10	72	---	16986	---	1465	---
	12	59	---	13846	---	1211	---
L4 – 66,99 x 64	6	231	---	57795	---	2565	---
	10	135	---	32031	---	1500	---
	12	111	---	26092	---	1239	---
L6 – 65,81 x 66	6	228	41	57277	74478	3286	1752
	10	133	74 ± 24	31736	98068 ± 19115	1924	3482 ± 930
	12	110	95	26834	81026	1589	3391
L6 – 88 x 91,15	6	427	---	107252	---	3366	---
	10	251	---	59581	---	1975	---
	12	207	---	48602	---	1634	---
L8 – 50,82 x 56	6	150	---	37706	---	4035	---
	10	87	---	20814	---	2357	---
	12	72	---	16922	---	1945	---
L8 – 83,15 x 84	6	370	4	93239	74188	4117	150
	10	226	39 ± 50	51807	91465 ± 14458	2464	1645 ± 1777
	12	180	49	42161	91353	1998	1160
L10 – 61,20 x 68	6	219	7	55261	90507	4828	303
	10	128	49 ± 18	30543	77345 ± 8543	2826	4408 ± 746
	12	106	4	24854	7483	2334	287
L10 – 100,46 x 102	6	543	---	136821	---	4915	---
	10	319	---	75965	---	2887	---
	12	264	---	61943	---	2389	---

Regarding the **numerical** analysis, the same patterns from the PLA numerical results were identified:

- There is an increase in the specific stiffness and specific energy absorbed with the increment of the specimen size;

- There is a decrease in the specific stiffness and specific energy absorbed with the increment of the core height for each structure;
- There is a decrease in specific stress with the increment of the relative density, without any interference of the specimen size.

Equally to the PLA numerical analysis, it is also possible to verify that:

- Structures with similar relative densities but different specimen size have different values of specific stiffness and specific energy absorbed;
- Structures with similar specimen size and different relative densities have a slight difference in specific stiffness and specific energy absorbed – the higher the relative density is, the higher are the values of these variables. This can be verified at the “L4 – 66,99 x 64” and “L6 – 65,81 x 66” structures.

Given the observations, it is then possible to conclude that, as expected, the hierarchy of the geometrical parameters influence over the structures maintains: the specimen size has the greatest contribution for the improvement in stiffness and energy absorption capacity, being the relative density the second most important parameter on this matter. Regarding the structures strength, it is only affected by the relative density. The patterns can be identified looking at the bar charts present in the appendix C.

In what concerns to the **experimental results**, it wasn't possible to verify the same patterns as in PLA numerical models and test specimens. It wasn't possible to relate any geometrical parameters with the specimens behaviour. Moreover, computing error statistics at the “h10” structures, a large uncertainty is noted at the three geometries, as can be seen in the table C.1 at the appendix C. This may be attributed to low displacement values that might be lower than the ones necessary to obtain reliable values. Given the large uncertainty associated to the values of the same study variable between different specimens (and therefore, different geometrical parameters), it isn't possible to go into further detail of discussion.

4.3.3 Comparison With Analytical Expressions

4.3.3.1 Relationship Between Relative Density and Thickness-to-Length Ratio

The relative density of the structures can be related to the wall thickness (t) and cell length (l) through a constant value, C . Recalling expression 2.3, this constant can be determined by a linear regression of the relative density versus the $\frac{t}{l}$ ratio plot for regular structures, visible on the figure 4.20. As there are different values of relative density for the same values of $\frac{t}{l}$ (due to different specimen sizes with equal cell length), two regressions are made: one for smaller structures and another for larger structures.

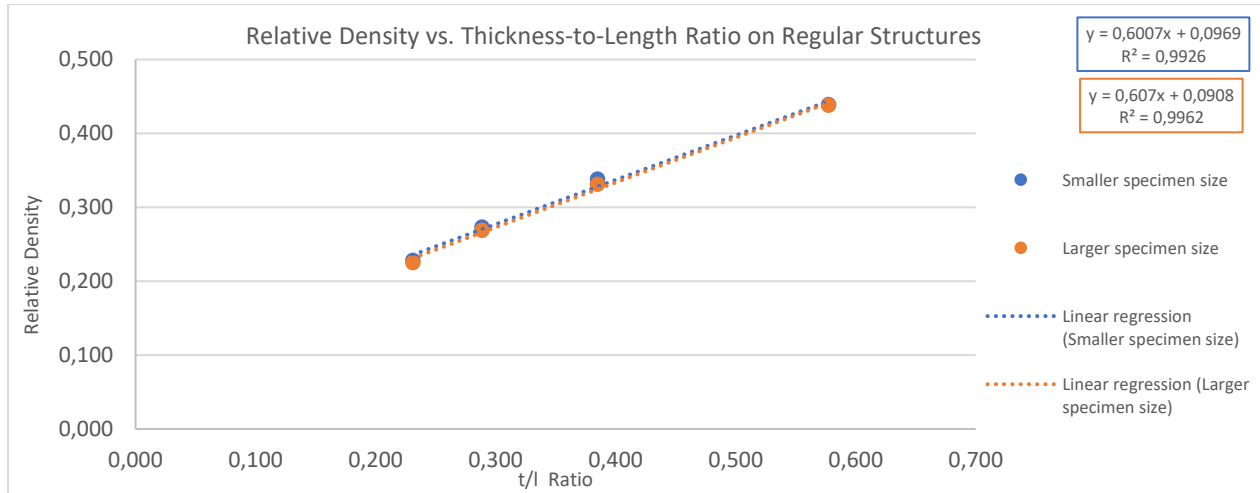


Figure 4.20 - Relative Density vs. Thickness-to-Length Ratio on Regular Structures.

Finding the average from the slope values of both linear regressions, it is possible to conclude that value of the constant C is equal to 0,604.

4.3.3.2 Relationship Between Study Variables and Thickness-to-Length Ratio

In an attempt to establish a linear relationship between the study variables, the wall thickness and the cell length, each study variable is plotted against the thickness-to-length ratio, once again one plot for smaller structures and another for larger ones, within the same study variables. Figures 4.21, 4.22 and 4.23 show the plots for the specific stiffness, specific energy absorbed and specific stress for the regular structures against the $\frac{t}{l}$ ratio, respectively. The considered values are taken from the numerical analysis.

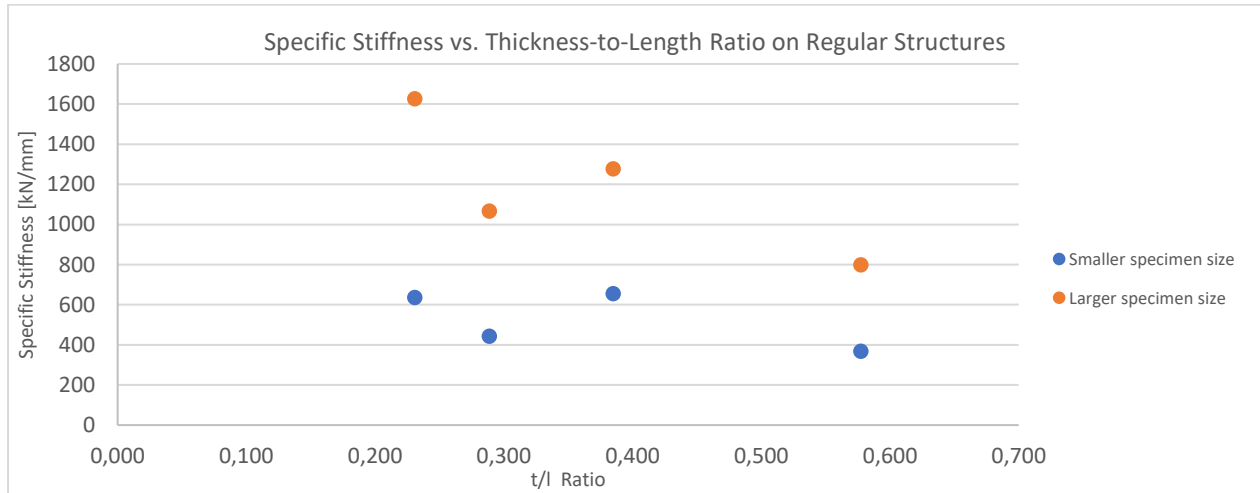


Figure 4.21 - Specific Stiffness vs. Thickness-to-Length Ratio on Regular Structures.

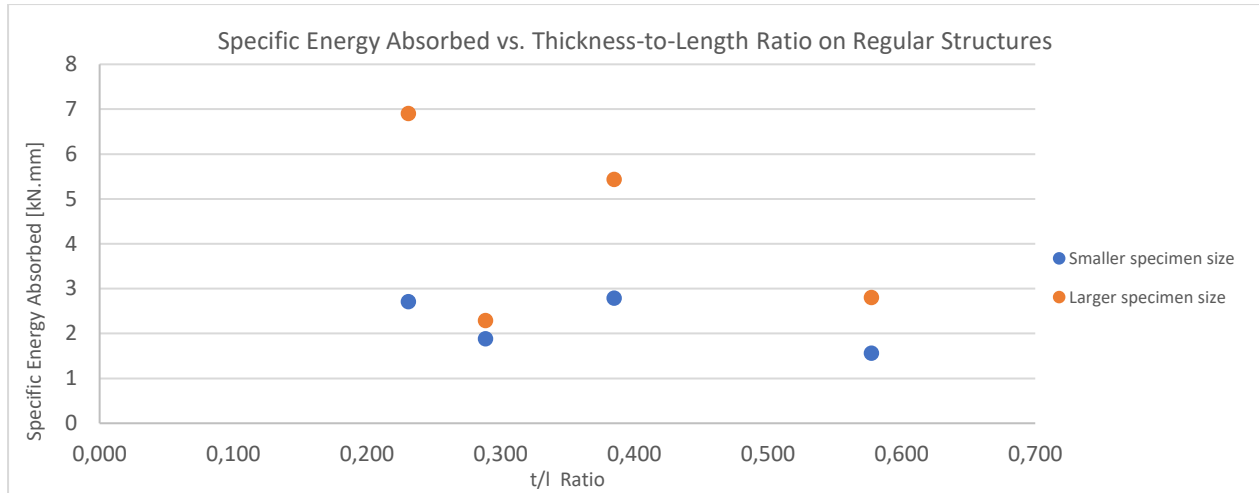


Figure 4.22 - Specific Energy Absorbed vs. Thickness-to-Length Ratio on Regular Structures.

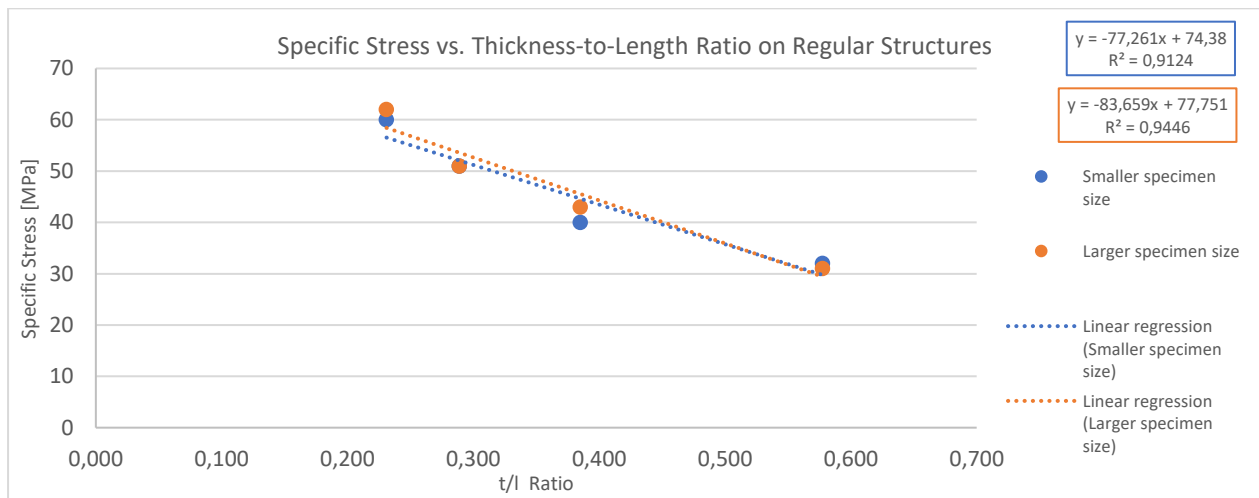


Figure 4.23 - Specific Stress vs. Thickness-to-Length Ratio on Regular Structures.

Observing figures 4.23, it is not possible to establish a linear relationship between either the specific stiffness or the specific energy absorbed with the thickness-to-length ratio, as in the work of Gibson and Ashby [10]. However, though the correlation coefficient values are lower than the general ones, it is possible to identify a linear relationship between the specific stress and the $\frac{t}{l}$ ratio. For the smaller structures case, the proportionality factor is the -77.261 , whereas for the larger structures case, the proportionality factor is -83.659 .

4.3.3.3 Determination of Euler's Critical Load and Comparison with Maximum Load

As stated further above in chapter 2, there may occur instabilities on the cells' walls when a certain value of applied vertical load is reached. Taking equation 2.7 into consideration with the factor n equal to 1, an attempt to establish a linear dependency of the maximum load (P_{max}) with the inverse of the squared core height. The last equation is then rewritten as follows:

$$P_{max} = (\pi^2 * E_s I) * \frac{1}{h^2} \quad 4.1$$

In order to obtain the theoretical critical load (P_{cr}), it is necessary to calculate in first place the second moment of area (I) for a regular hexagonal geometry. It is dependent on the cell's length (l) and can be calculated according to the following:

$$I = \frac{5\sqrt{3}}{16} * l^4 \quad 4.2$$

Computing the analyses' maximum load and the theoretical critical load of PLA versus the inverse of the squared core height for largest regular structures of each cell length (L4, L6, L8 and L10), it is possible to verify that maximum load has a linear dependency from $\frac{1}{h^2}$. However, the slope value returned from the linear regression is, in all cases, 1 to 2 orders of magnitude lower than the theoretical slope from the critical load's linear regression. This may be attributed to an area effect that is not being considered here. In further analysis to the plots, it is also possible to verify that, for L4 and L6 structures, the maximum load is higher than the critical load, meaning that, for the rehearsed values of displacement, these structures may present instabilities. The charts here referred can be found at the appendix C, along with the values of the linear regressions.

4.3.4 Comparison Between Regular structures and Graded structures

One of the objectives of this work is to assess if in-plane gradients in honeycomb structures improve the out-of-plane crushing worthiness relatively to the regular structures. In order to do so, and for matter of understanding the influence of geometrical gradients, the numerical results of PLA structures are used for this purpose since they have well-established patterns that are easily identified.

Since the specimen size and the relative density are parameters that greatly affect the performance of the structures, two structures (regular and graded) were isolated in first instance to assess the effect of gradients: "L6 – 88 x 91.15" and "T6-8-10", with the same core height, and very similar specimen sizes as well as relative densities (0.331 and 0.332, respectively). Although it is possible to verify that the graded structure ("T6-8-10") has more stiffness and better energy absorption capacity, the increases are small – 1.2% on the specific stiffness and 1.9% on the specific energy absorbed – which don't make possible to affirm that in-plane gradients improve the performance of the structures only by its mass distribution. Nevertheless, analysing other regular and graded structures with the equal core height and similar specimen size, but different relative densities, the improvement of energy absorption capacity and stiffness is very notable. Comparing "L10 – 100.46 x 102" and "S0.5+_2O", with relative densities 0.225 and 0.466 respectively, the specific stiffness increases 5.3% and the specific energy absorbed increases 6.1%. It is then possible to affirm that, keeping the specimen size, graded structures that are designed to have greater relative densities than regular structures improve their performance when it comes to stiffness and energy absorption. This also applies to the structure's strength, once the specific stress is only dependent on the relative density, as discussed previously.

Chapter 5: Conclusions

The honeycomb structures are the most used core solution when it comes to sandwich structures. The high strength-to-weight ratio makes this type of structure very attractive for many applications, making it of wide use throughout many areas of industry. Emerging Additive Manufacturing techniques allows the use of new materials and facilitates the production of more complex geometries as the cores of the panels. One of the main assets (besides the strength-to-weight ratio) is the high energy absorption capacity, which can be further enhanced through the design of functionally graded structures. This design can be approached either by material's composition changes or by geometrical changes. This work intended to design FGM structures by the introduction of geometrical gradients, being the cell walls' thickness-to-length ratio, the chosen project parameter.

The studies on this work comprised the analysis of uniform (regular structures) and graded wall thickness cellular cores. In other works that have studied honeycomb structures [30, 34], the specimen size has been pointed as one of the factors that influences the behaviour of the structures when it comes to stiffness, energy absorption and strength. It was possible to conclude that the overall size of the structure and the length-to-thickness ratio are the main factors to influence the out-of-plane mechanical behaviour of the honeycomb structures. However, as there wasn't a correspondence on the results trends between the numerical analysis and the experimental testing, it isn't possible to quantify with certainty what is the effect of the overall specimen size and relative density (the last one expressing the length-to-thickness ratio) over the structures' energy absorption and stiffness. Regarding the structures strength, geometries with higher relative densities have lower stresses, being this variable independent on the overall specimen size. Also, graded structures have their stiffness, energy absorption and strength improved due to the mass distribution: structures that benefit from a larger mass concentration near the centre have their out-of-plane mechanical properties improved.

Relatively to the potential of Additive Manufacturing for the mentioned structures, the development of tailored sandwich panels cores, such as the functionally graded honeycombs, impose significant geometrical requirements of the manufacturing processes used to produced them. Considering so, the design freedom allowed by AM technologies emerges as a natural solution for their production and continuous development. Additionally, future developments should take into consideration process constraints as early as possible in the design process, taking advantage of methodologies such as design for additive manufacturing.

In what concerns to the PLA specimens, there was a good correspondence between numerical and experimental results, validating Fused Filament Fabrication process as an alternative to produce design prototypes of graded cellular materials. Regarding the Selective Laser Melting technique, it was not possible to make any definite statement due to the incongruent results on aluminium specimens.

Finally, the good correlation between Finite Element Analysis results and the experimental testing makes possible to state that the Finite Element Method is an excellent tool when it comes to the analysis of this type of structures.

5.1 Future Work

Given the potential of the honeycomb structures, the following future work is proposed:

- The review the results from aluminium experimental testing;
- The study of the in-plane properties on functionally graded honeycomb structures;
- The study of the out-of-plane properties on honeycomb structures with other types of unit cell (Plateau and Lotus);
- Further studies on the hierarchically-graded honeycomb structures.

References

- [1] T. Bitzer, *Honeycomb Technology: Materials, Design, Manufacturing, Applications and Testing*, 1st ed., Chapman & Hall, 1997.
- [2] Z. Wang, "Recent advances in novel metallic honeycomb structure," *Composites Part B: Engineering*, vol. 166, pp. 731-741, 2019.
- [3] K. K. Chawla, *Composite Materials: Science and Engineering*, 4th ed., Springer, 2019.
- [4] V. Birman and G. A. Kardomateas, "Review of current trends in research and applications of sandwich structures," *Composites Part B: Engineering*, vol. 142, pp. 221-240, 2018.
- [5] H. Araújo, M. Leite, A. M. R. Ribeiro, A. M. Deus, L. Reis and M. F. Vaz, "Investigating the contribution of geometry on the failure of cellular core structures obtained by additive manufacturing," *Frattura ed Integrità Strutturale*, vol. 13, pp. 478-486, 2019.
- [6] A. Miranda, M. Leite, L. Reis, E. Copin, M. F. Vaz and A. M. Deus, "Evaluation of the influence of design in the mechanical properties of honeycomb cores used in composite panels," *Journal of Materials: Design and Applications*, vol. 235, pp. 1325-1340, 2021.
- [7] J. Bru, M. Leite, A. R. Ribeiro, M. F. Vaz and A. M. Deus, "Bioinspired structures for core sandwich composites produced by fused deposition modelling," *SAGE Journals*, vol. 234, pp. 379-393, 2020.
- [8] J. G. Monteiro, M. Sardinha, F. Alves, A. R. Ribeiro, L. Reis, A. M. Deus, M. Leite and M. F. Vaz, "Evaluation of the effect of core lattice topology on the properties of sandwich panels produced by additive manufacturing," *Journal of Materials: Design and Applications*, vol. 235, pp. 1312-1324, 2020.
- [9] I. Carranza, A. Crocombe and I. Mohagheghian et al., "Characterising and modelling the mechanical behaviour of polymeric foams under complex loading," *J Mater Sci*, vol. 54, pp. 11328-11344, 2019.
- [10] L. Gibson and M. Ashby, *Cellular Solids: Structure and Properties*, 2nd ed., Cambridge University Press, 1997.
- [11] R. Kamaliev and R. Charkviani, "Creation of Ultra-light Spacecraft Constructions Made of Composite Materials," *Procedia Engineering*, vol. 185, pp. 190-197, 2017.
- [12] S. H. Goodman and H. Dodiuk, *Handbook of Thermoset Plastics*, 3rd ed., Elsevier, 2014.
- [13] D. Bathe, C. A. Penick, L. A. Ferry and C. Lee, "Classification and Selection of Cellular Materials in Mechanical Design: Engineering and Biomimetic Approaches," *Designs*, vol. 3, 2019.
- [14] A. J. V. Miranda, "Desenvolvimento, caracterização e modelação de novos conceitos no projecto de honeycombs usados em painéis compósitos," MSc dissertation, Instituto Superior Técnico - University of Lisbon, 2019.

- [15] F. Zhu, G. Lu, D. Ruan and Z. Wang, "Plastic Deformation, Failure and Energy Absorption of Sandwich Structures with Metallic Cellular Cores," *Internal Journal of Protective Structures*, vol. 1, pp. 507-541, 2020.
- [16] M. Helou and S. Kara, "Design, analysis and manufacturing of lattice structures: an overview," *International Journal of Computer Integrated Manufacturing*, vol. 31, pp. 243-261, 2018.
- [17] ISO/ASTM 52900 standard, "Additive manufacturing: General principles, Terminology," 2015.
- [18] I. Gibson, D. Rosen, B. Stucker and M. Khorasani, *Additive Manufacturing Technologies*, 3rd ed., Springer, 2021.
- [19] M. Attaran, "The rise of 3-D printing: The advantages of additive manufacturing over traditional manufacturing," *Business Horizons*, vol. 60, pp. 677-688, 2017.
- [20] ASTM F2792-12a standard, *Standard Terminology for Additive Manufacturing Technologies*, 2012.
- [21] I. Bahnini, M. Rivette, A. Rechia, A. Siadat and A. Elmesbahi, "Additive manufacturing technology: the status, applications and prospects," *The International Journal of Advanced Manufacturing Technology*, vol. 97, pp. 147-161, 2018.
- [22] J. Gardan, "Additive manufacturing technologies: state of the art and trends," *International Journal of Production Research*, vol. 54, pp. 3118-3132, 2015.
- [23] B. G. M. Silva, "Cellular structures for use in composite panels with a mass distribution gradient produced by additive manufacturing," MSc dissertation, Instituto Superior Técnico - University of Lisbon, 2021.
- [24] O. A. Mohamed, S. H. Masood and J. L. Bhowmik, "Optimization of fused deposition modeling process parameters: a review of current research and future prospects," *Additive Manufacturing*, vol. 3, pp. 42-53, 2015.
- [25] O. S. Carneiro, A. F. Silva and R. Gomes, "Fused deposition modeling with polypropylene," *Materials & Design*, vol. 83, pp. 768-776, 2015.
- [26] H. Li, Z. Luo, L. Gao and P. Walker, "Topology optimization for functionally graded cellular composites with metamaterials by level sets," *Computer Methods in Applied Mechanics and Engineering*, vol. 328, pp. 340-364, 2018.
- [27] C. M. Taylor, C. W. Smith, W. Miller and K. E. Evans, "The effects of hierarchy on the in-plane elastic properties of honeycombs," *International Journal of Solids and Structures*, vol. 48, pp. 1330-1339, 2011.
- [28] M. Ali, A. Qamhiyah, D. Flugrad and M. Shakoob, "Theoretical and finite element study of a compact energy absorber," *Advances in Engineering Software*, vol. 39, pp. 95-106, 2008.

- [29] J. Fang, G. Sun, N. Qiu, T. Pang, S. Li and Q. Li, "On hierarchical honeycombs under out-of-plane crushing," *International Journal of Solids and Structures*, vol. 135, pp. 1-13, 2018.
- [30] Y. Zhang, M. Lu, C. H. Wang, G. Sun and G. Li, "Out-of-plane crashworthiness of bio-inspired self-similar regular hierarchical honeycombs," *Composite Structures*, vol. 144, pp. 1-13, 2016.
- [31] S. Y. Choy, C. Sun, K. F. Leong and J. Wei, "Compressive properties of functionally graded lattice structures manufactured by selective laser melting," *Materials & Design*, vol. 131, pp. 112-220, 2017.
- [32] I. Maskery, N. T. Aboulkhair, A. O. Aremu, C. J. Tuck, I. A. Ashcroft and R. D. Wildman, "A mechanical property evaluation of graded density Al-Si10-Mg lattice structures manufactured by selective laser melting," *Materials Science & Engineering A*, vol. 670, pp. 264-274, 2016.
- [33] S. Limmahakhun, A. Oloyede, K. Sitthiseripratip, Y. Xiao and C. Yan, "Stiffness and strength tailoring of cobalt chromium graded cellular structures for stress-shielding reduction," *Materials and Design*, vol. 114, pp. 633-641, 2017.
- [34] B. Yu, S. N. Khaderi, V. S. Deshpande and N. A. Fleck, "The effect of matrix shear strength on the out-of-plane compressive strength of CFRP cross-ply laminates," *International Journal of Solids and Structures*, vol. 139, pp. 79-95, 2018.
- [35] B. Yu, B. Han, P. Su, C. Ni, Q. Zhang and T. J. Lu, "Graded square honeycomb as sandwich core for enhanced mechanical performance," *Materials and Design*, vol. 89, pp. 642-652, 2016.
- [36] J. Schwenke and D. Krause, "Optimization of load introduction points in sandwich structures with additively manufactured cores," *Design Science*, vol. 6, 2020.
- [37] H. D. S. S. J. Geramizadeh, "Numerical and experimental investigation for enhancing the energy absorption capacity of the novel three-dimensional printed sandwich structures," *Journal of Materials: Design and Applications*, no. Proceedings of the Institution of Mechanical Engineers, Part L, 2021.
- [38] Y. Tao, S. Duan, W. Wen, Y. Pei and D. Fang, "Enhanced out-of-plane crushing strength and energy absorption of in-plane graded structures," *Composites Part B*, vol. 118, pp. 33-40, 2017.
- [39] S. Kumar, M. S. Rao, I. Balasundar, A. Singh, T. Raghu and G. M. Reddy, "Compressive behaviour of a nickel superalloy Superni 263 honeycomb sandwich pane," *Journal of Sandwich Structures & Materials*, vol. 22, pp. 1426-1449, 2020.
- [40] S. Townsend, R. Adams, M. Robinson, B. Hanna and P. Theobald, "3D printed origami honeycombs with tailored out-of-plane energy absorption behaviour," *Materials and Design*, vol. 195, p. 108930, 2020.
- [41] F. P. Beer, E. R. Johnston, J. T. DeWolf and D. F. Mazurek, *Mechanics of Materials*, 5th ed., New York: McGraw-Hill, 2009.

- [42] ASTM C365-94 standard, *Standard test method for flatwise compressive properties of sandwich cores*.
- [43] S. Brischetto and R. Torre, "Tensile and Compressive Behavior in the Experimental Tests for PLA Specimens Produced via Fused Deposition Modelling Technique," *Journal of Composites Science*, vol. 3, 2020.

Appendix A: Numerical Methodology

This appendix contains supplementary charts, tables and figures that are related to every numerical methodology's subjects.

A.1 Use of Symmetry

In order to spend less computation time and resources, an additional model was set up making use of two symmetry planes along the x - and z - directions, as can be seen in figure A.1. The use of these two symmetry planes results in a reduction of the model geometry to a quarter of its original (figure A.2).

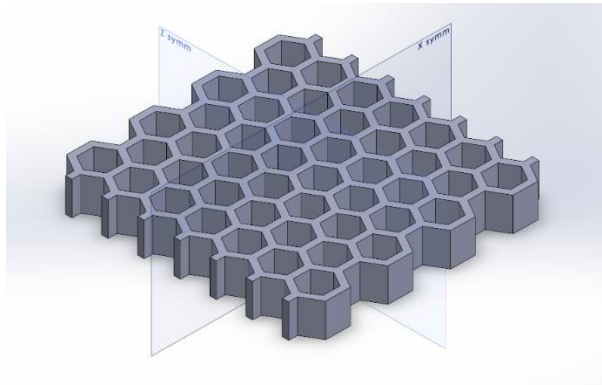


Figure A. 1 - Symmetry plans over the honeycomb structure.

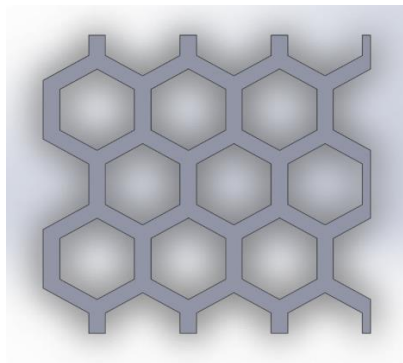


Figure A. 2 - Cut of the honeycomb structure's original model into a quarter.

The original model was cut in the CAD software to create the symmetric model, exporting an .IGS file with the new geometry, ready to be assembled at the FEM model.

The deviation between the full model and the quarter model was calculated in order to check the correspondence between both models after the convergence analysis and mesh refinement at each.

Table A. 1 - Parameters and simulation time for various meshes (quarter model).

	Global seed size [mm]	Number of nodes	Number of elements	Simulation time [s]
Quarter model	1.4	6434	3278	66
	1.2	8074	4194	108
	1.1	8576	4480	123
	1.0	12537	6850	120
	0.95	13104	7186	148

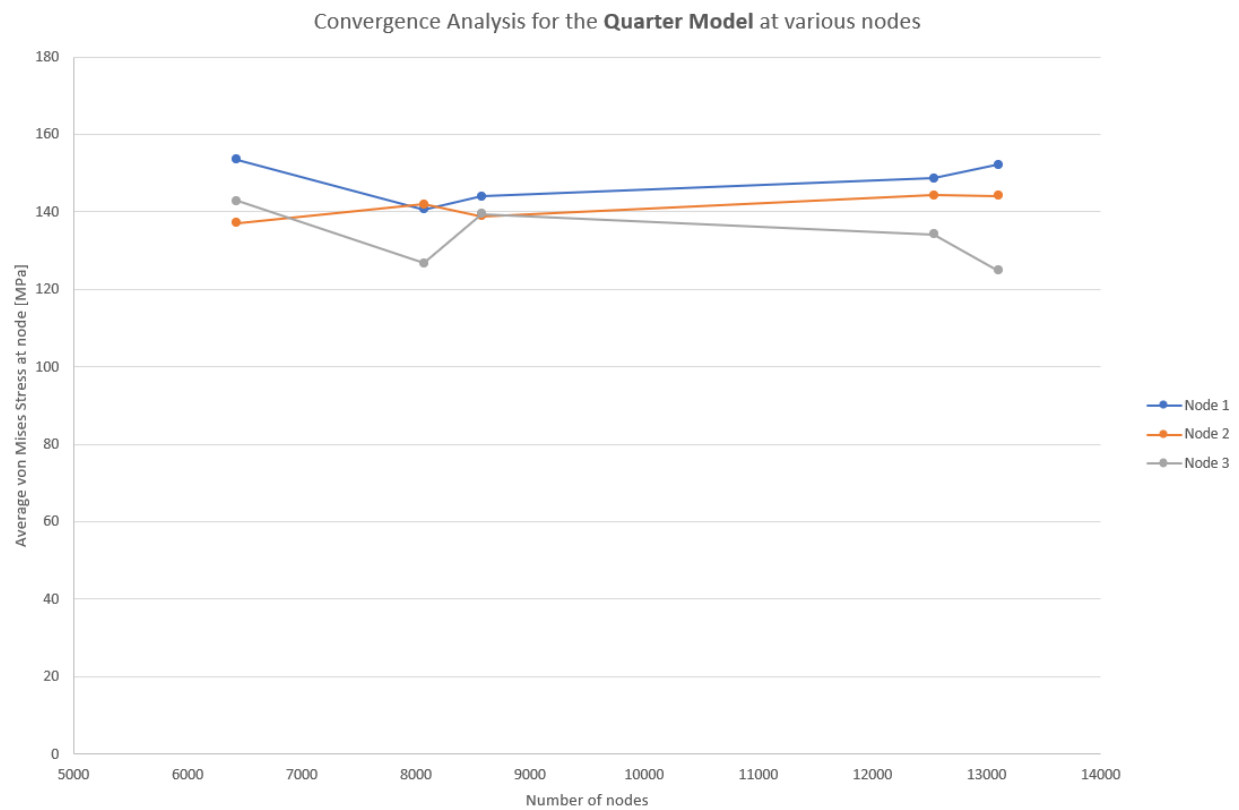


Figure A. 3 - Convergence analysis for the full model at various nodes.

The following table contains the error computed between both models on various node pointed to be critical, considering the full model as the reference for theoretical values. The error was computed in accordance with the expression presented below:

$$Error \text{ at node } i \text{ [\%]} = \frac{|\bar{\sigma}_{VM \text{ quarter model}, i} - \bar{\sigma}_{VM \text{ full model}, i}|}{\bar{\sigma}_{VM \text{ full model}, i}} * 100 \quad A.1$$

Table A. 2 - Computation of error between both models on various nodes.

	Error [%]
Node 1	4.16
Node 2	9.34
Node 3	3.60

Given the convergence analyses and the error calculated between both models on various nodes, if the considered mesh for the quarter model is the one with 1.0 mm set as global seed size, it is possible to verify that there is a good correspondence between the quarter model and the full model, making this one a good alternative in future works to model the structures in order to save computational resources and simulation time.

Appendix B: Materials Properties and Composition

This appendix contains supplementary information about the materials properties and their composition.

B.1 Aluminium's Chemical Composition

Table B.1 contains the chemical composition of the aluminium alloy used to produce the SLM specimens.

Table B. 1 - Chemical composition of aluminium alloy AISi7Mg0,6.

Chemical element	Min. mass fraction [%]	Max. mass fraction [%]
Aluminium (Al)	Balance	Balance
Copper (Cu)	---	0,05
Iron (Fe)	---	0,19
Magnesium (Mg)	0,45	0,70
Manganese (Mn)	---	0,10
Silicon (Si)	6,50	7,50
Titanium (Ti)	---	0,25
Zinc (Zn)	---	0,07
Others ind.	---	0,03
Others all	---	0,10

B.2 PLA specimen's Mechanical Properties

As referred in chapter 3.1, the PLA filament manufacturer hasn't made available the technical data sheet of the material. Hence, it isn't possible to have reference values of the material's mechanical properties. Given the importance of the Young's Modulus to establish a measure of resistance between different materials and to assess, by means of experimental testing, if the produced parts have good properties, this property was measured. By taking out the value of the elastic region's slope in the experimental stress-strain curves, where the stress is calculated by the fraction of the force over the specimen size, it comes the result of the Young's Modulus of the material in the specific direction of the loading (E_3^*), as referred by Gibson and Ashby [10]. Then, the Young's Modulus of the solid (E_s) is calculated using the expression 2.5.. As the specimens were all produced under the same conditions in the same period of time, this property was only evaluated at the regular specimens.

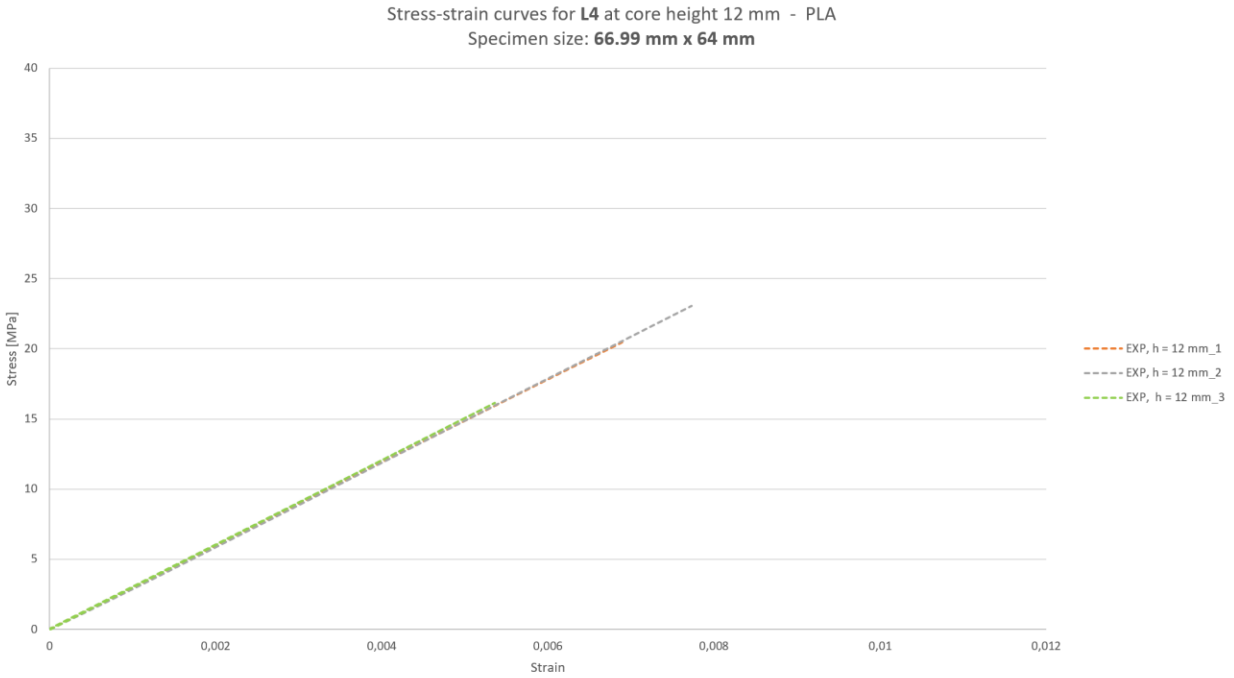


Figure B. 1 - Stress-strain curves for L4 PLA specimens – Experimental testing.

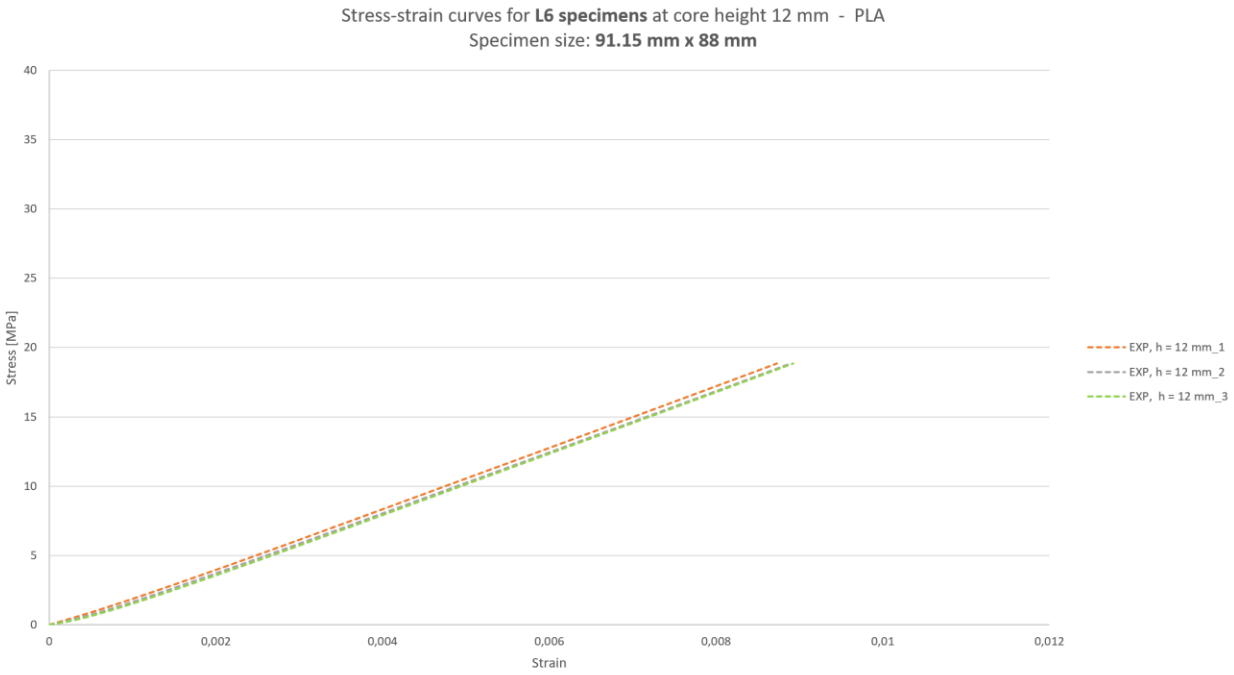


Figure B. 2 - Stress-strain curves for L6 PLA specimens – Experimental testing.

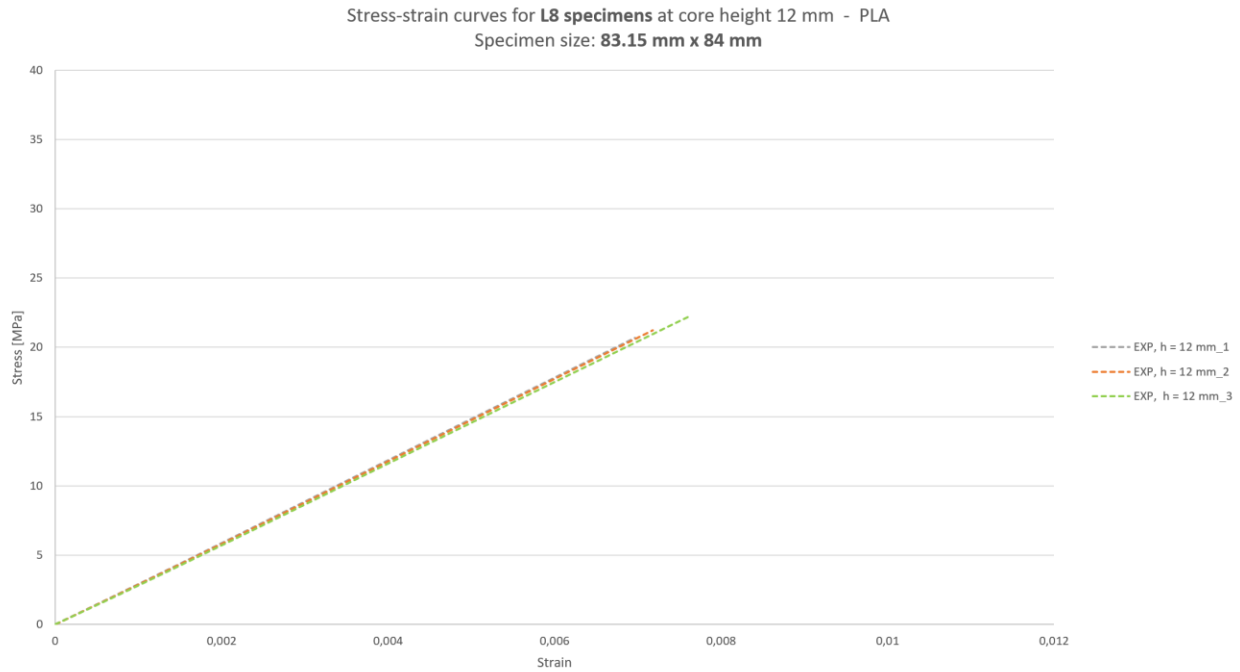


Figure B. 3 - Stress-strain curves for L8 PLA specimens – Experimental testing.

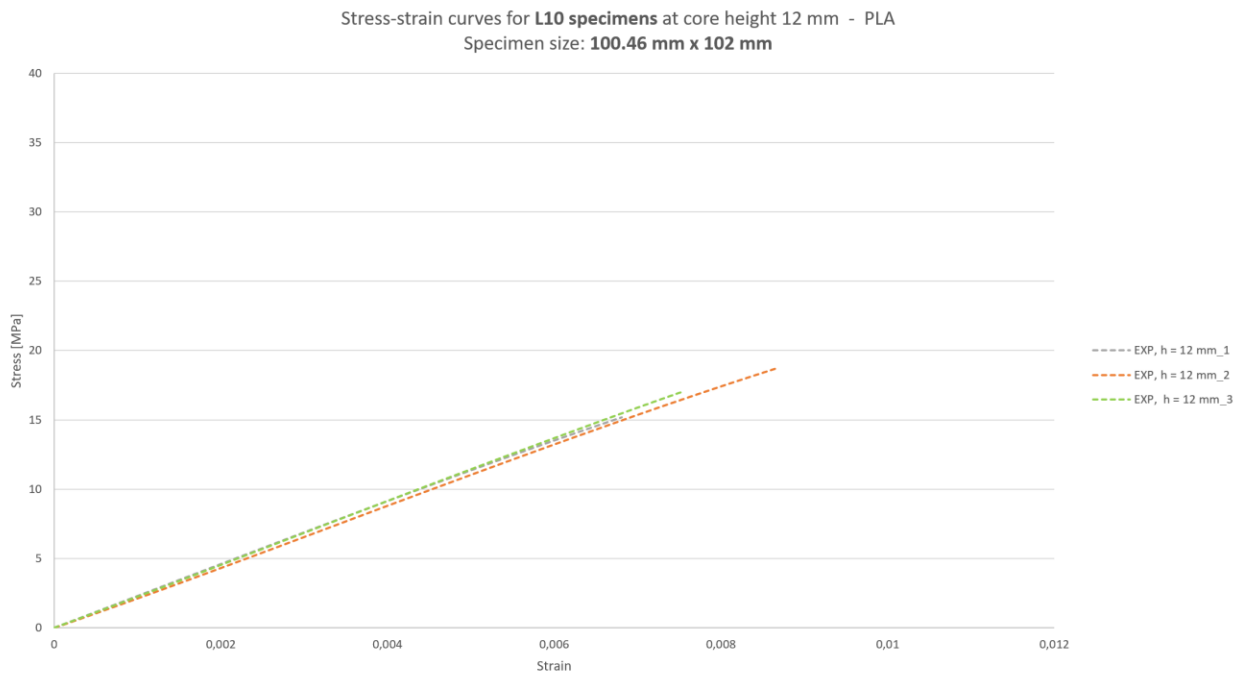


Figure B. 4 - Stress-strain curves for L10 PLA specimens – Experimental testing.

Table B.3. shows the computed Young's Modulus values of the PLA specimens, obtained using the procedure above mentioned.

Table B. 2 - Computed values for the Young's Modulus values of PLA specimens.

	h [mm]	E_3^* [MPa]	E_s [MPa]	Averaged E_s [MPa]
L4 – 66,99 x 64	12 – 1	1147	1987	1985
	12 – 2	1115	1930	
	12 – 3	1178	2039	
L6 – 65,81 x 66	12 – 1	790	2052	1895
	12 – 2	657	1706	
	12 – 3	742	1927	
L8 – 83,15 x 84	12 – 1	650	2250	2352
	12 – 2	703	2436	
	12 – 3	684	2370	
L10 – 100,46 x 102	12 – 1	423	1829	1872
	12 – 2	365	1582	
	12 – 3	509	2204	

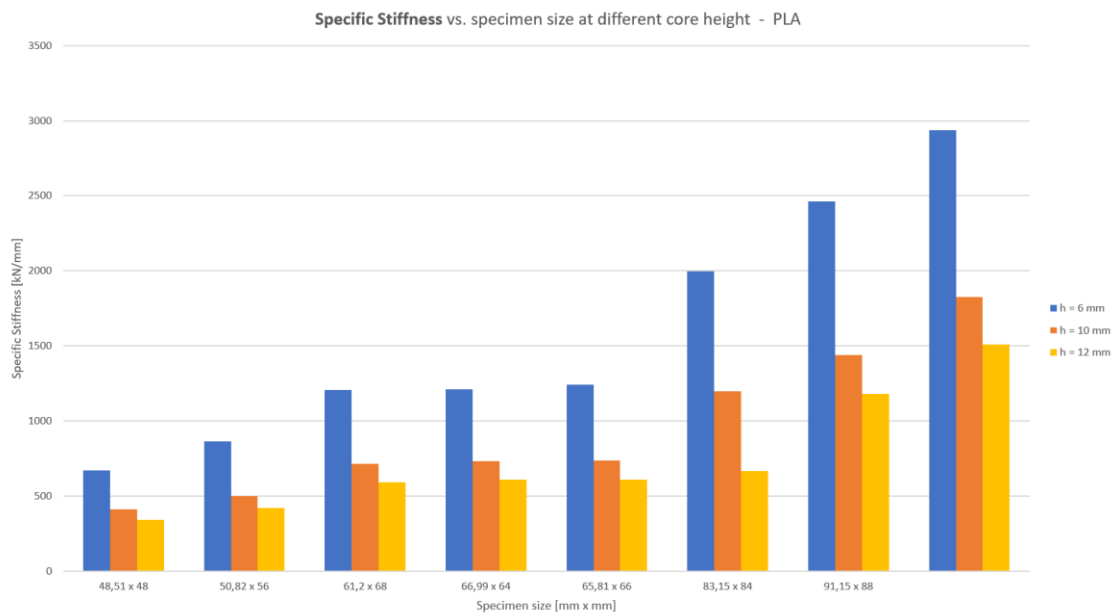
As it is possible to verify, the averaged Young's Modulus of the solid varies between 1872 MPa and 2352 MPa, values that are in accordance with the referenced ones for polymeric materials. This was discussed previously in section 4.3.

Appendix C: Parametric Studies on the Geometrical Parameters Influence and Results Processing

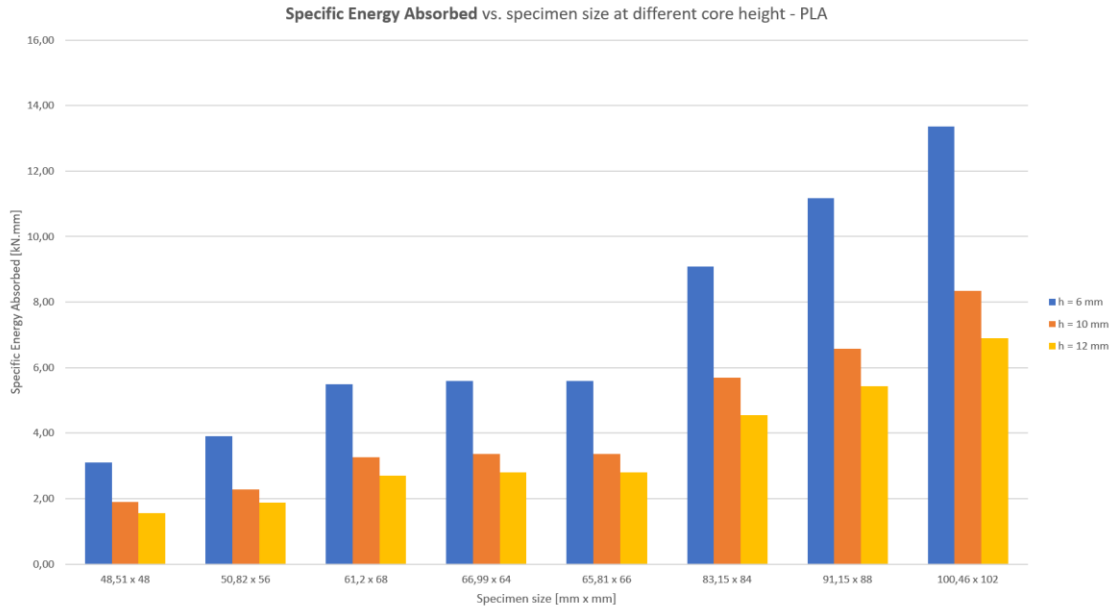
This appendix contains supplementary charts and plots related to the parametric studies on the geometrical parameters influence over the structures, as well as supplementary plots to verify the materials' mechanical properties on the specimens.

C.1 PLA regular structures – Elasto-plastic regime simulation

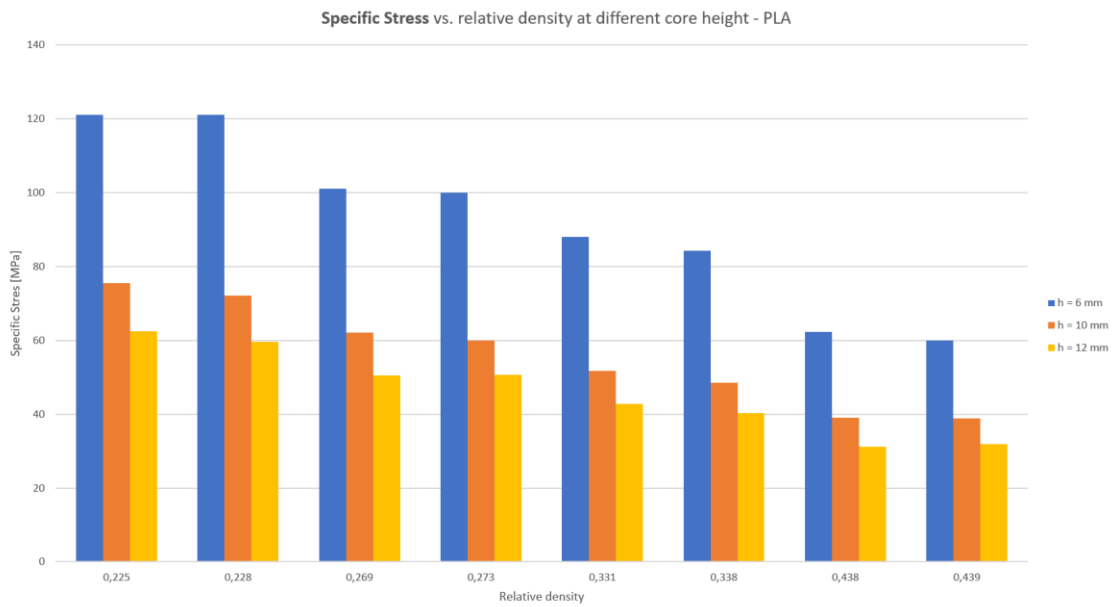
Following the trend of the section 4.3., the charts below represent the results from the three study variables with its dependence on specimen size and relative density at the numerical analysis of PLA regular structures, using the model of the elasto-plastic mechanical regime.



(a)



(b)



(c)

Figure C. 1 - Specific values of (a) stiffness, (b) energy absorbed and (c) stress vs. specimen size and relative density at PLA regular structures – elasto-plastic numerical analysis.

C. 2 PLA Stress-strain curves

Figure C.2 shows the stress-strain curves for a regular structure (“L4 – 66.99 x 64”) on both numerical analysis and experimental test.

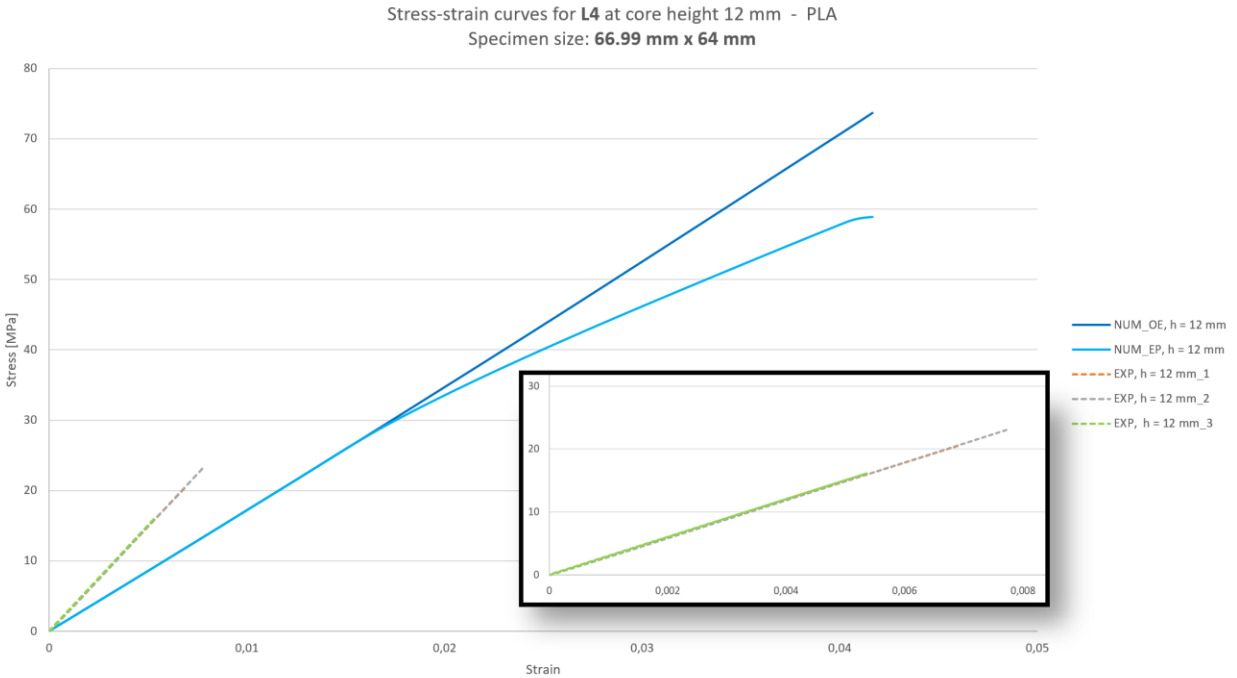


Figure C. 2 - Stress-strain curves for L4 at PLA regular structures – Numerical analysis and experimental test.

Figure C.3 shows the stress-strain curves for a graded structure from the third design method (“ $R_1 = +0.31$ ”) on both numerical analysis and experimental test.

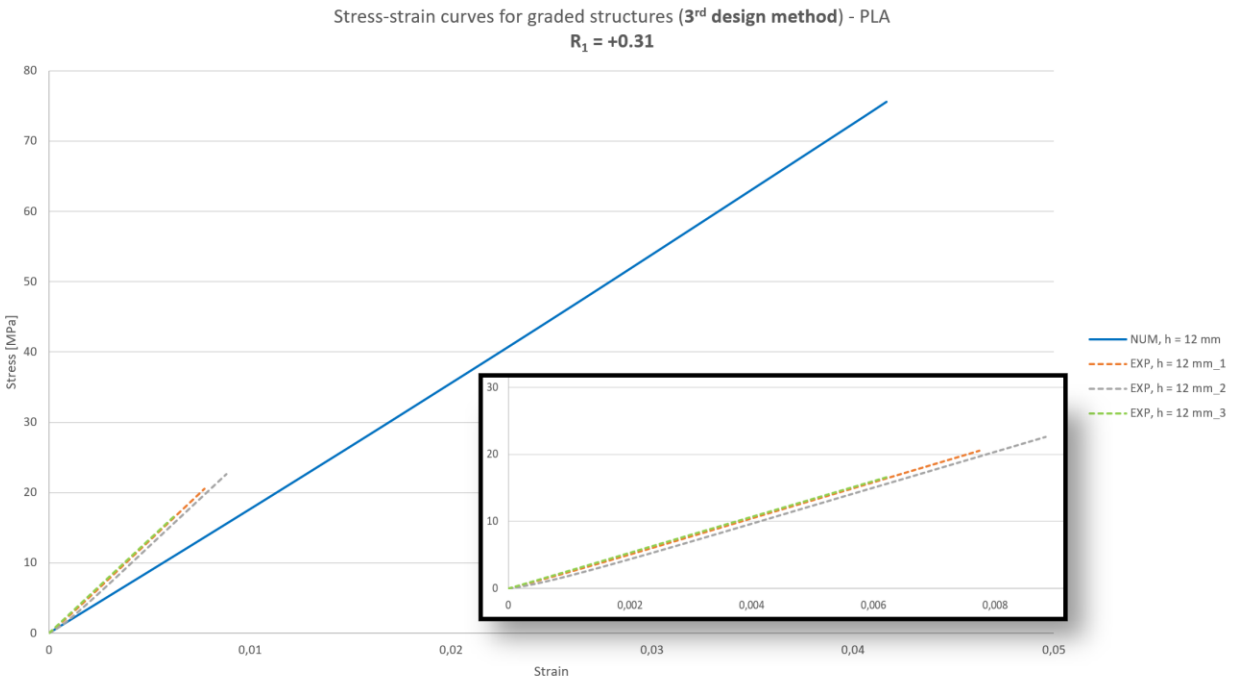
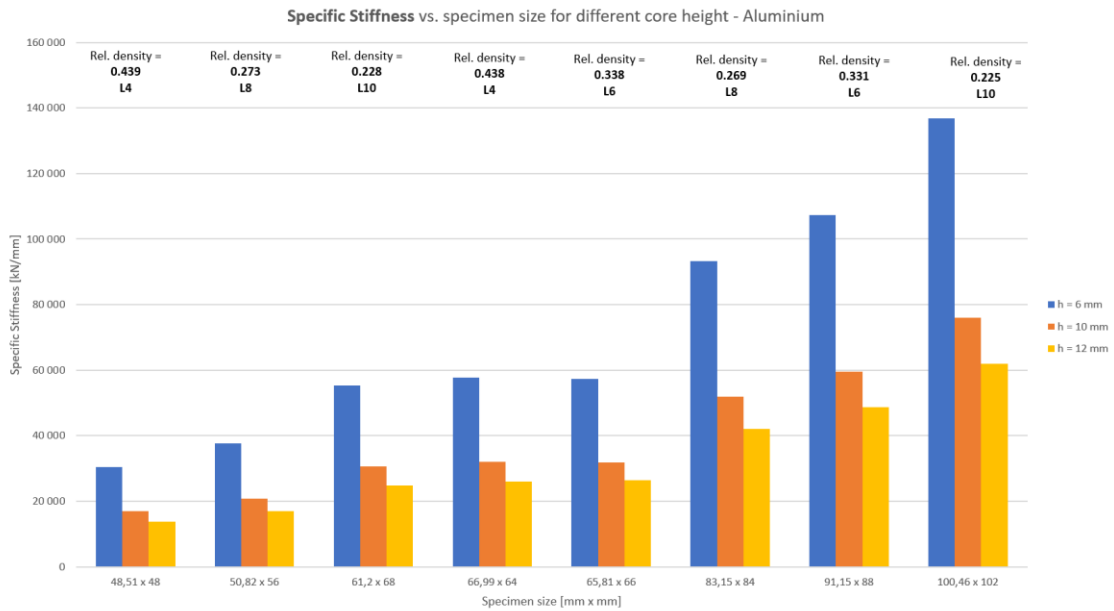


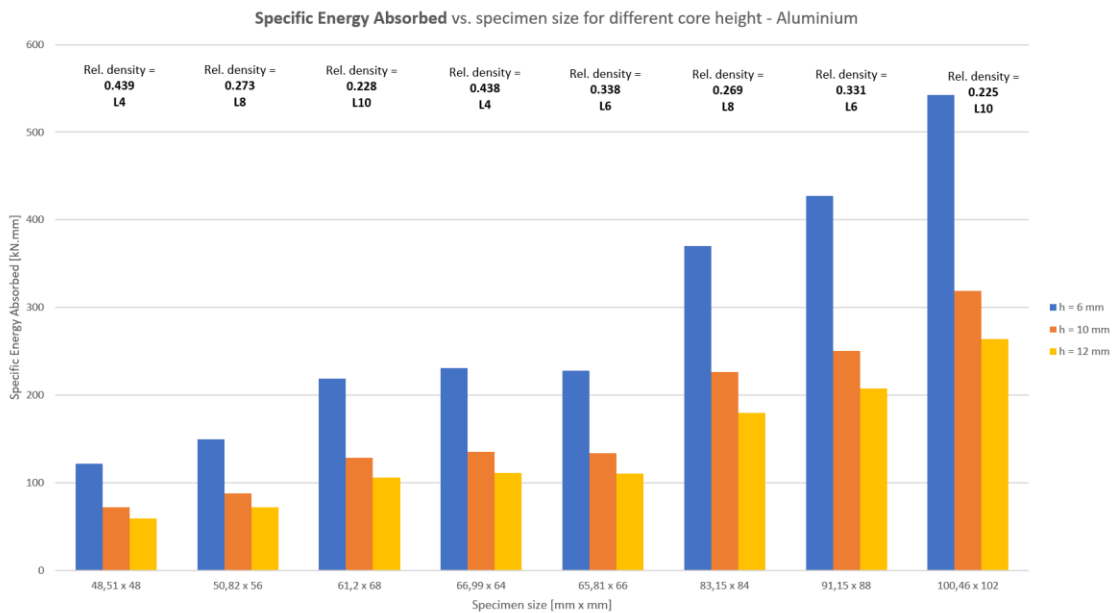
Figure C. 3 - Stress-strain curves for $R_1 = +0.31$ at PLA graded structures – Numerical analysis and experimental test.

C.3 Aluminium regular structures – Numerical analysis

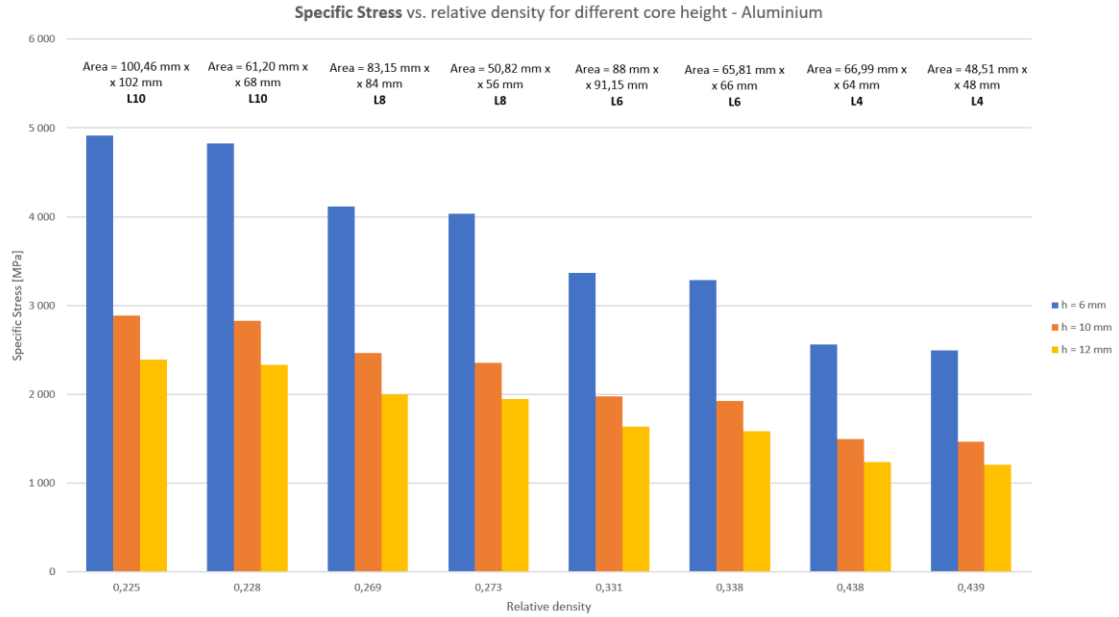
Similarly to the previous charts, figure C.4 represents the results from the three study variables dependent on specimen size and relative density at the numerical analysis of aluminium regular structures.



(a)



(b)

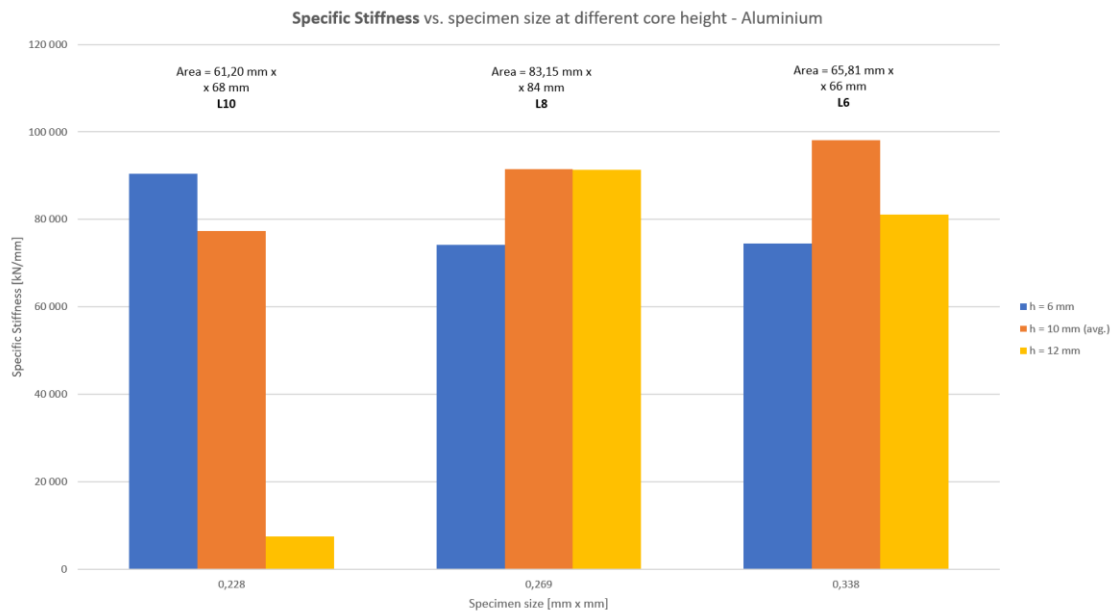


(c)

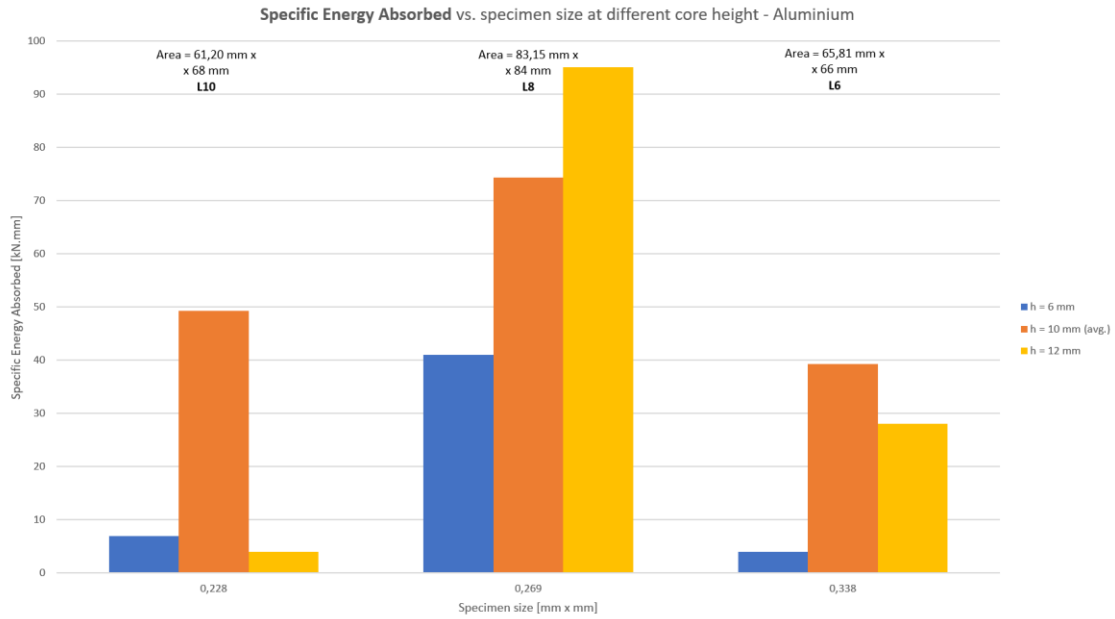
Figure C. 4 - Specific values of (a) stiffness, (b) energy absorbed and (c) stress vs. specimen size and relative density at aluminium regular structures – numerical analysis.

C.4 Aluminium regular structures – Experimental test

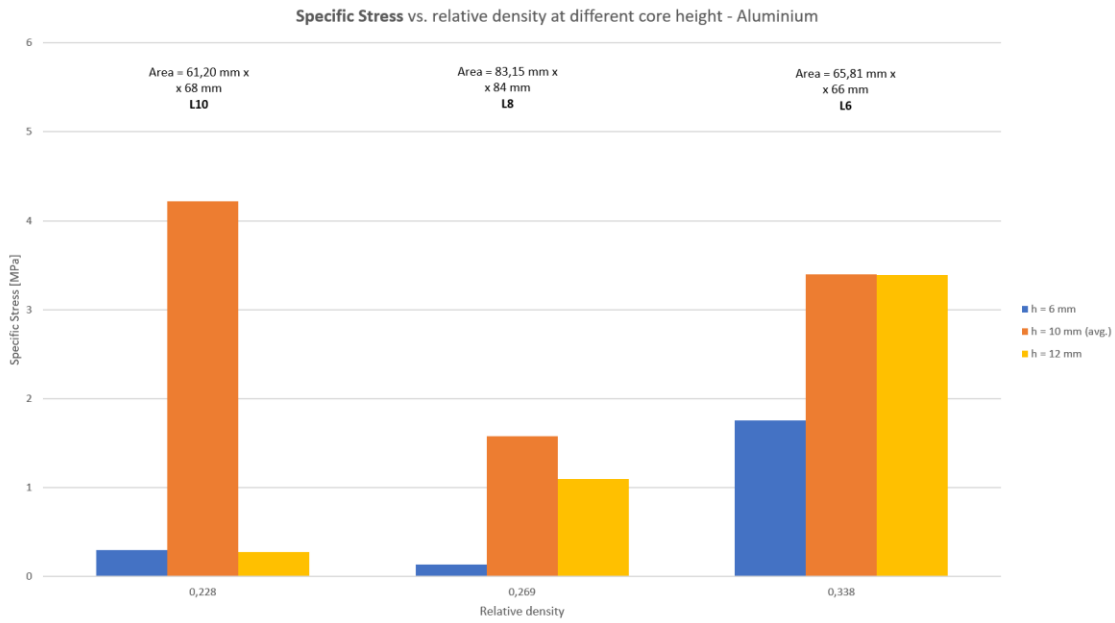
Figure C.5 represents the results from the three study variables vs. the relative density at the experimental test of aluminium regular structures.



(a)



(b)



(c)

Figure C. 5 - Specific values of (a) stiffness, (b) energy absorbed and (c) stress vs. specimen size and relative density at aluminium regular structures – experimental test.

C.5 Error Statistics for Aluminium Experimental Testing Results

The error is defined as being the value of the standard deviation over the mean value of each study variable.

Table C. 1 - Error statistics for "h10" aluminium samples.

	Error for $\frac{E_a}{\rho}$ [%]	Error for $\frac{K}{\rho}$ [%]	Error for $\frac{\sigma}{\rho}$ [%]
L6, h10	32.4	19.5	26.7
L8, h10	128.2	15.8	108.0
L10, h10	36.7	11.0	16.9

C.6 Aluminium Stress-strain curves

Figure C.6 shows the stress-strain curves for a regular structure ("L6 – 65.81 x 66") on both numerical analysis and experimental test.

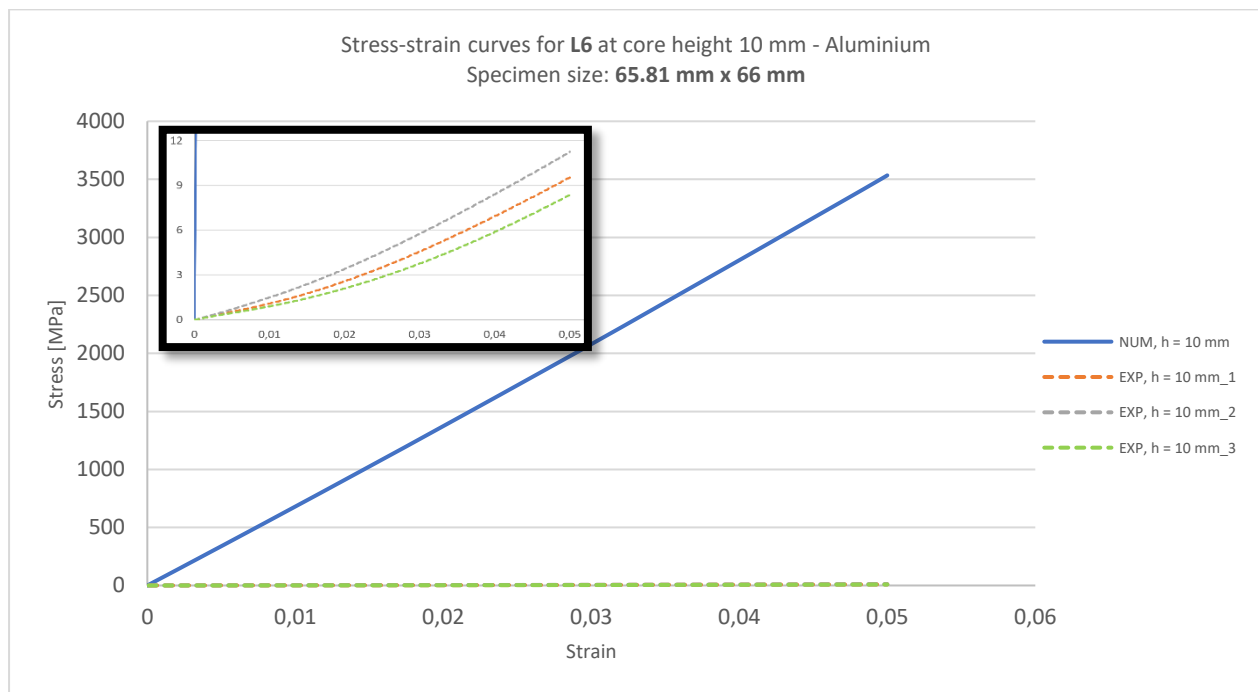


Figure C. 6 - Stress-strain curves for L6 at aluminium regular structures – Numerical analysis and experimental test.

C.7 Determination of Euler's Critical Load and Comparison with Maximum Load

Figures C.7 to C.10 show the plots of the maximum load (P_{max}) for the numerically analysed displacement and the theoretical critical load (P_{cr}), for the larger structures of L4, L6, L8 and L10 PLA regular geometries, respectively.

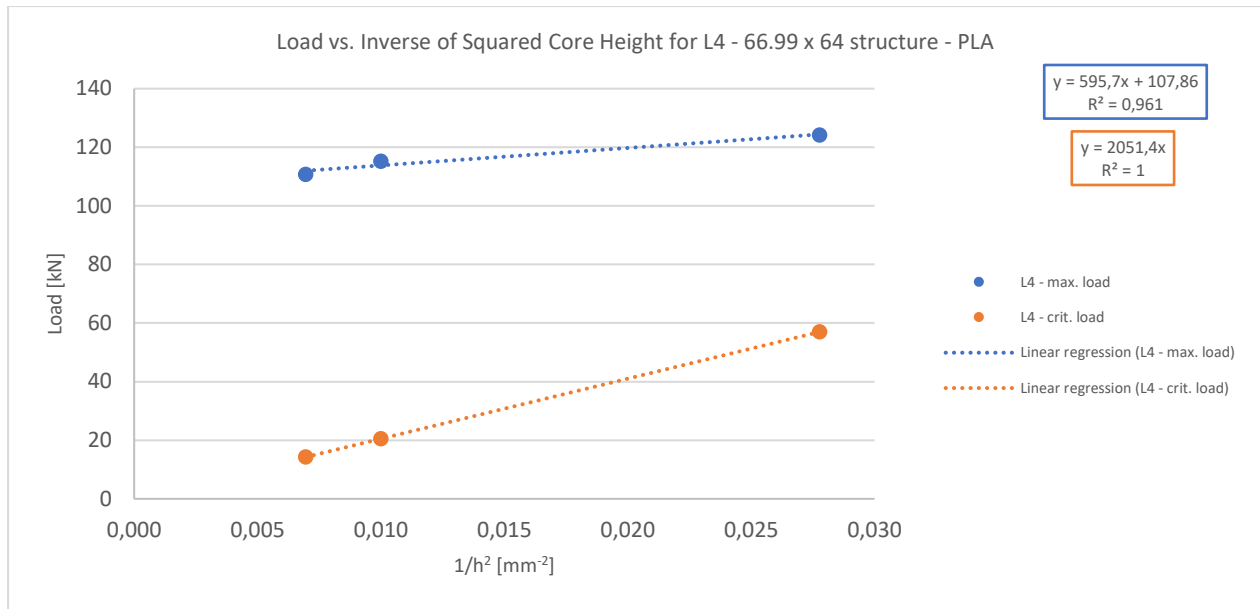


Figure C. 7 - Load vs. Inverse of Squared Core Height for L4 – 66.99 x 64 structure – PLA numerical analysis.

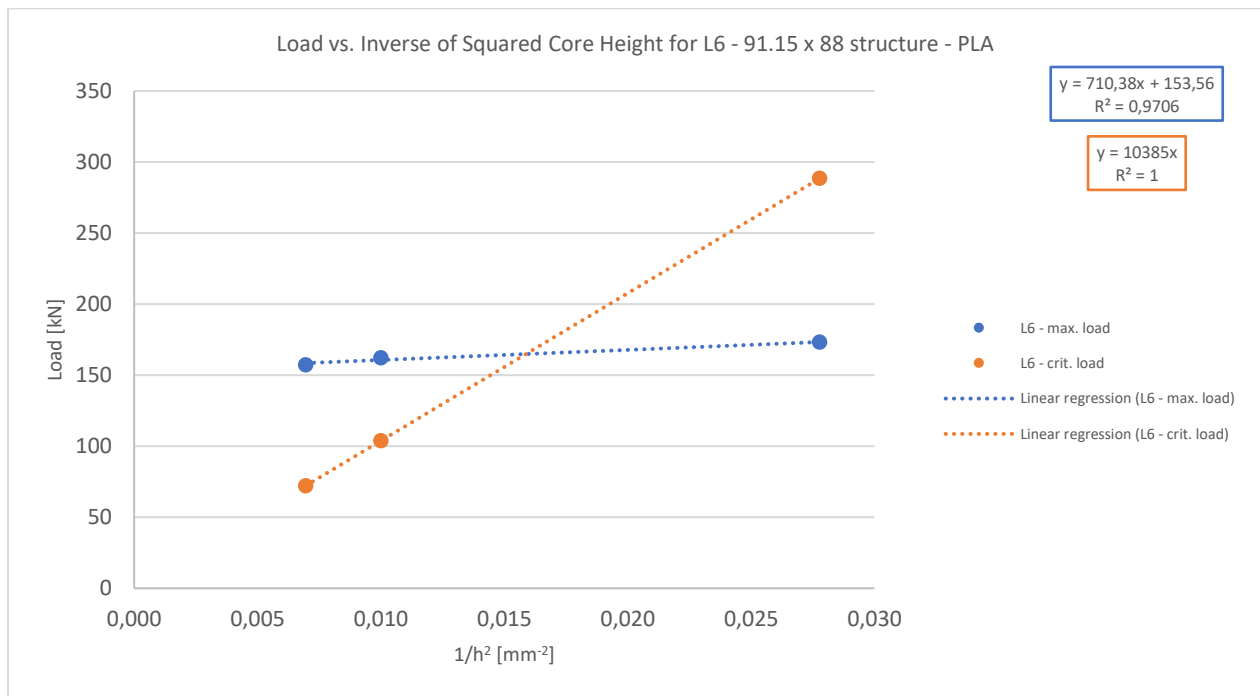


Figure C. 8 - Load vs. Inverse of Squared Core Height for L6 – 91.15 x 88 structure – PLA numerical analysis.

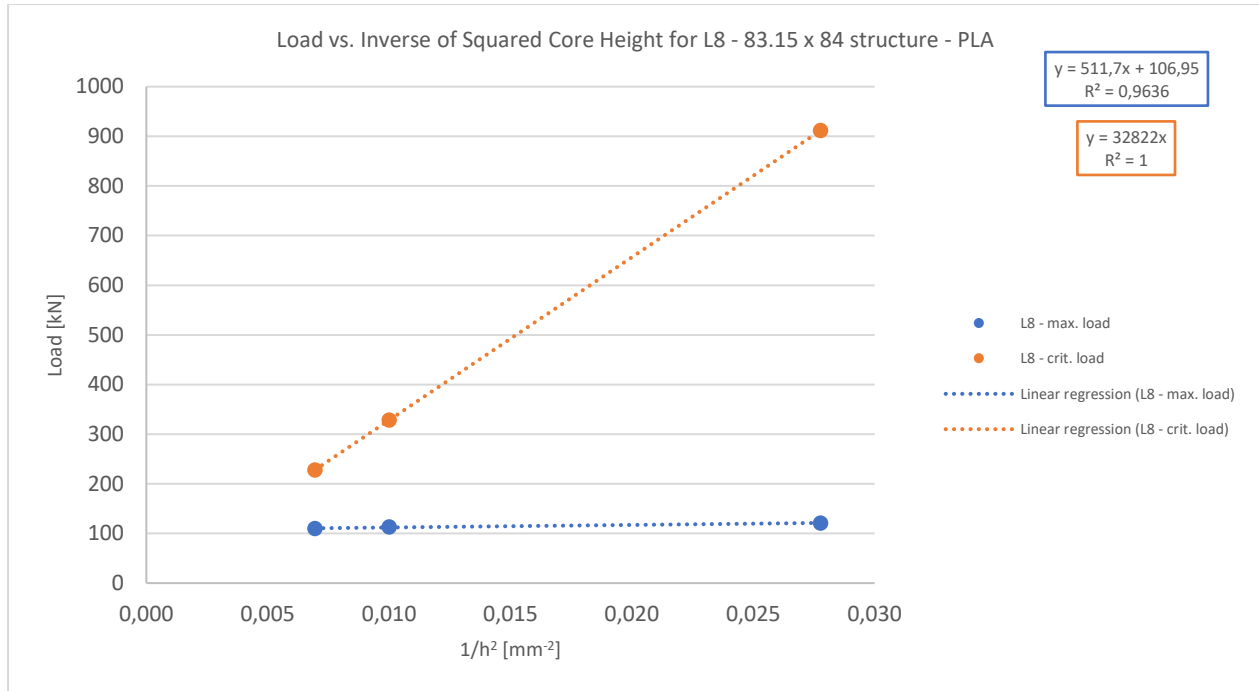


Figure C. 9 - Load vs. Inverse of Squared Core Height for L8 – 83.15 x 84 structure – PLA numerical analysis.

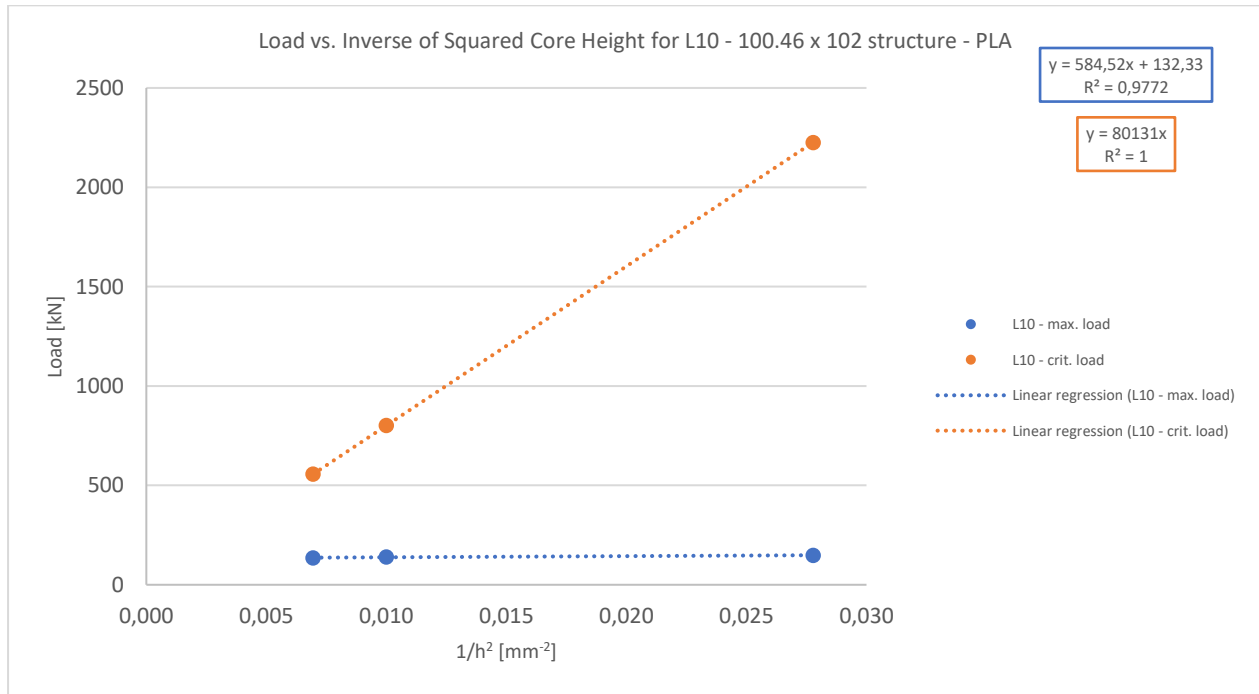


Figure C. 10 - Load vs. Inverse of Squared Core Height for L10 – 100.46 x 102 structure – PLA numerical analysis.

Table C.2 compares the slope values of the maximum load regressions with the ones of the critical load regressions.

Table C. 2 – Slope values of maximum load and critical load linear regressions vs. inverse of squared core height.

	$\pi^2 * E_s I$ (Maximum Load)	$\pi^2 * E_s I$ (Critical Load)
L4 – 66.99 x 64	595,70	2051,4
L6 – 91.15 x 88	710,38	10385
L8 – 83.15 x 84	511,70	32822
L10 – 100.46 x 102	584,52	80131

Appendix D: Produced Specimens

D.1 PLA Specimens

Figure D.1 shows the produced PLA regular specimens. There are only exhibited the larger specimen sizes for each structure.

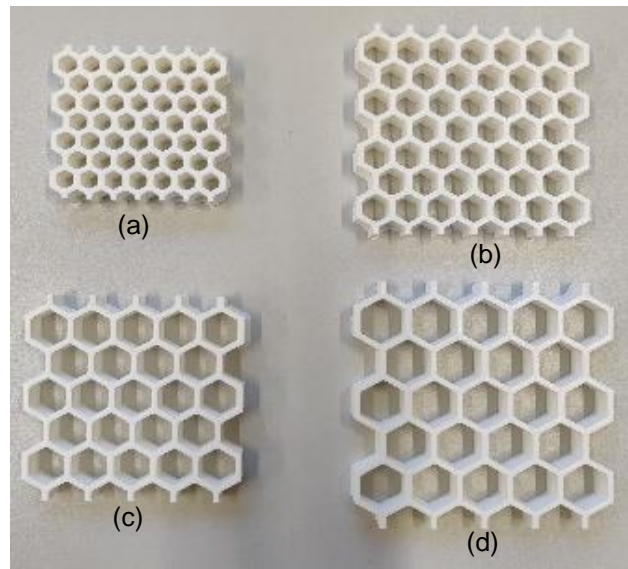


Figure D. 1 - PLA Specimens of geometries (a) L4, (b) L6, (c) L8, (d) L10.

Figure D.2 shows the produced PLA graded specimens.

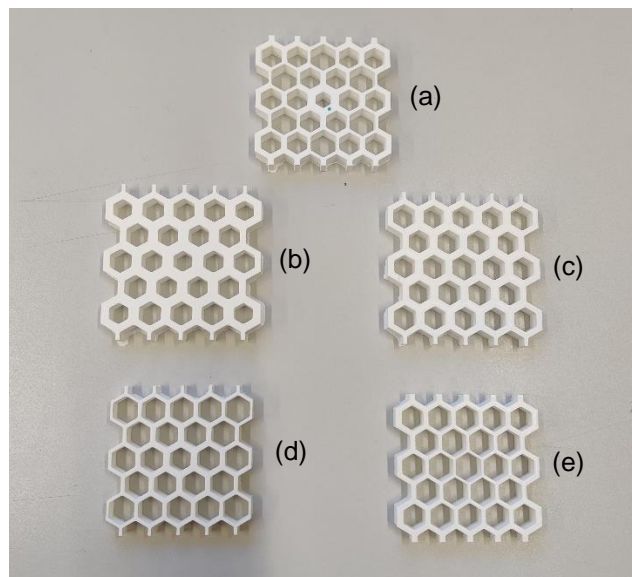


Figure D. 2 - PLA specimens of graded structures: (a) "T6-8-10"; (b) "S0.5+_20"; (c) "S0.5-_20"; (d) "R1 = +0.31"; (e) "R1 = -0.31".

D.2 Aluminium Specimens

Figure D.3 shows the produced aluminium regular specimens.

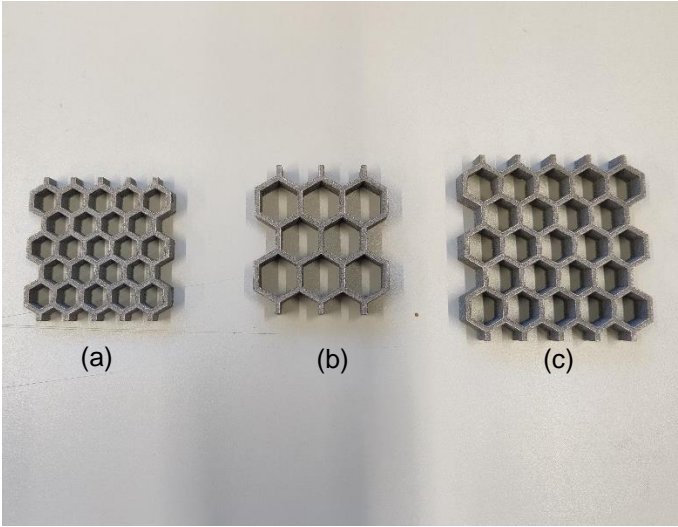


Figure D. 3 - Aluminium Specimens of geometries (a) L6, (b) L8, (c) L10.